Transient Wall Temperature and Film Thickness of Vertical Annular Two-Phase Pulsatile Flow

by

Brian Fehring

thesis submitted in partial fulfillment of

the requirements for the degree of

Master of Science

(Mechanical Engineering)

at the

University of Wisconsin-Madison

2018

Transient Wall Temperature and Film Thickness of Annular Two-Phase Pulsatile Flow

Brian Fehring, Master of Science
Department of Mechanical Engineering
University of Wisconsin-Madison, 2018
Professor Gregory F. Nellis, Advisor
Arganthaël Berson, Co-advisor
Kristofer Dressler, Co-advisor

Annular flow is a specific type of two-phase flow common in a variety of boiling and condensing applications. The thin liquid film in annular flow provides a higher heat transfer coefficient compared to other flow types but is susceptible to critical heat flux or drying out, which causes a significant decrease in the heat transfer coefficient. Studying the heat transfer coefficient and film thickness of annular flow can provide insight into the coupling between the two and how to prevent issues like liquid film dryout and critical heat flux.

The facility described in this thesis is capable of developing vertical two-phase annular flow. During the current study, many of the facility components were repaired or upgraded, allowing better function of the system and control of the flow. A controllable boiler system was constructed and installed which can introduce consistent pulses of vapor into the flow for studying oscillatory conditions.

The techniques used to measure the liquid film thickness and wall temperature of the flow were improved. The instantaneous wall temperature can now be accurately and reliably measured and synchronized with instantaneous measurements of the liquid film thickness.

The current facility and instantaneous measurements of the film thickness and wall temperature can be used to estimate the wall shear and heat transfer coefficient of vertical annular two-phase pulsed flow.

Acknowledgments

I would like to thank Professor Greg Nellis, my primary advisor and committee chair, for this opportunity. His well-timed guidance, cryo-cool patience, and abundant trust in me over the past two years has helped make graduate school a great experience. I hadn't considered graduate school before talking with Professor Nellis, but now I can't imagine my life without it. I would like to thank my co-advisors Kris Dressler (Dress) and Arganthaël Berson. Dress is a great leader and truly unites the lab. He is somehow able to keep everyone motivated without sacrificing a fun and positive environment. Arganthaël is like a fountain of modeling and troubleshooting ideas. Whenever I became stuck, especially when working on the temperature optics, Arganthaël always seemed to have a solution. I have truly enjoyed working with all three of you.

I would like to thank Professor Sanford Klein and Professor Franklin Miller for their time and serving on my committee.

I would like to acknowledge Bettis Laboratory for their financial support. Thank you to Evan Hurlburt, Tom Conroy, and Louise McCarrol for their guidance with the project and understanding when deadlines could not be met.

I would like to thank my friends in the Solar Energy Lab. Being a part of the SEL community was a pleasure and added an extra dimension to my graduate school life.

I would like to thank the undergraduates that worked on our project over the past two years: James, Simon, Cruz, Mari, Fatima, Ian, Tyler, Dan, and Sydney. Thank you, Jason, for constantly challenging me to be better. Jason was perhaps my greatest critic and pushed me to always check my designs and consider new techniques rather than become complacent with those I already knew. Thank you, Roman, for the countless hours of assistance and fun. I will miss your chill attitude (which seemed to be unwavering, even while scrambling to catch our flight out of Denver), our easygoing banter, and the long data collection sessions in the lab, complete with excellent 'jams'. All of you added a valuable part to the lab and together, made my work possible.

Table of Contents

Abstract i

Acknowledgments ii

Table of Contents iii

List of Tables vi

List of Figures vii

Nomenclature xi

1 Two-Phase Flow 1

1.1 Annular Flow 1

1.1.1 Heat Transfer Coefficient 2

1.1.2 Pulsatile Flow 3

2 MFVAL Annular Flow Facility 4

2.1 Water and Glycol Heat Pump Loop 4

2.2 R245fa Refrigerant Loop 8

2.3 Mixing Tee 12

2.4 Developing Flow Section 13

2.4.1 Main Development Section 13

2.4.2 Development to Test Section Transition 16

2.5 Pipe Transition Sections 18

2.6 Test Section 21

2.6.1 Design and History 21

2.6.2 2017 Changes 23

3 Pulse Generator **27**

3.0.1 History 27

3.0.2 Thermodynamic Model 30

3.0.3 Heating Element Thermal Analysis 37

3.0.4 Mechanical Design and Construction 40

3.0.5 Wiring, Controls, and Instrumentation 49

3.0.6 Safety Features 53

4 Measurement Methods and Results **54**

4.1 Annular Flow Liquid Film Thickness Measurements 54

4.1.1 Optical Theory 56

4.1.2 Experimental Setup 58

4.1.3 Calibration 60

4.1.4 Data Processing 61

4.1.5 Results and Analysis 63

4.2 Wall Temperature Measurements 67

4.2.1 Background 68

4.2.2 Optical Theory 69

4.2.3 Experimental Setup 73

4.2.4 Calibration 78

4.2.5 Results and Analysis 82

5 Vertical Annular Two-Phase Pulsatile Flow **86**

5.1 Results 86

6 Conclusions **94**

References **95**

7 Appendix **100**

7.1 Part Drawings 100

7.1.1 Test Section 101

7.1.2 Pulse Generator 110

7.1.3 Development Section 116

7.1.4 Test Section / Development Section Flow Converter 117

7.1.5 Development to Test Section Converter 119

7.1.6 3D-Printed Prism Holder 121

7.1.7 3D-Printed Double Laser Holder 122

7.2 Pulse Generator 123

7.2.1 Thermodynamic Model EES Code 123

7.2.2 Critical Heat Flux EES Code 126

7.2.3 Cartridge Heater Geometry MATLAB Code 127

7.2.4 Cartridge Heater Finite Element Analysis MATLAB Code 133

7.3 Wall Temperature 140

7.3.1 Intensity Ratio Model 140

List of Tables

1 Labels for refrigerant heat exchangers shown in both Figures 3 and 4 . . 6

2 Input conditions used for calculating the pulse generator required input power 32

3 Cartridge heater rated power and size information 34

4 Cartridge heater rated power at 240 V and actual power using 205 V available in the lab, corresponding total powers are roughly 3900 W rated and 2800 W actual 36

5 Cartridge heater sleeve finite element thermal analysis boundary conditions and settings 38

6 Surface area comparison of bare cartridge heater and sleeve geometry . . 44

7 Cartridge heater phase connections 50

8 Test section optical materials in the order encountered by the input laser beam, refractive indices for 632.8 nm light wavelength and a 15-35 °C temperature range 77

9 Test section material interfaces for reference in Equation 11 78

10 Curve fitting parameters used in Figure 53 81

11 Subplot labeling nomenclature 86

List of Figures

1 A few patterns for vertical two-phase flow regimes, given by Hewitt and Hall-Taylor [8] and consolidated into a single graphic 2

2 Rendering of Annular Flow facility pulse generator and test section assembly 5

3 Schematic of the MFVAL water and glycol heat pump loop 6

4 Schematic of the MFVAL R245fa refrigerant loop 8

5 Vapor and liquid mass flow rates during a temperature calibration 10

6 Vapor and liquid mixing tee 12

7 Main development section 13

8 Single section, previous main development section 15

9 Development section to test section internal duct converter 17

10 Left: Test section to round pipe transition; Right: round pipe to development section transition 18

11 Round pipe to development section transition 20

12 Annular Flow test section in 2016 21

13 Section view of the test section; 1 - Main plate, 2 - Window flange, 3 - Float glass window, 4 - Pressure tape / wire lead, 5 - ULTEM spacer . . 23

14 Annular Flow test section 2017-2018 24

15 Cutaway rendering of the redesigned pulse generator installed in the MFVAL 28

16 Mark Rodarte's pulse generator 29

17 Schematic of the old pulse generator 30

18 Total required heating power and critical power (per cartridge heater) as a function of target output vapor mass flow rate, geometries considered are 9-inch long cylinders with 0.5, 0.75, and 1.25-inch diameters 33

19 Pulse generator vapor mass flow rate at 3 Hz, data from 2018-6-20 35

20 Pulse generator vapor mass flow rate model (Equation 2) and data collected on 2018-7-24 36

21 PDE Toolbox geometry for single cartridge heater and sleeve 38

22 FEA results for a single cartridge heater and sleeve 39
23 Cutaway views of the pulse generator with components labeled 40
24 Schematic of the redesigned pulse generator 42
25 Pulse generator pipe flanges and top and bottom plates 43
26 Left: Pulse generator tank components; Right: Flanges welded to 10-inch pipe 44
27 Left: Single cartridge heater sleeve with fins; Right: Cartridge heater sleeves installed on the base plate 45
28 Left: Top view of stainless steel bulkhead fitting; Right: Bottom view . . 46
29 Top plate of pulse generator with bulkhead fittings attached 47
30 Pulse generator pressurized to 55 PSI gage for leak test 48
31 Left: Three-phase power box with fuses, indicator LED's, and six Solid-State Relays; Right: DAQs for interfacing with LabVIEW 49
32 Pulse generator heater power circuit with 3-phase 240 V source shown in the upper left and the heaters middle-right 50
33 All six cartridge heaters and respective blue LEDs activated 51
34 Pulse generator heater control circuit (top) and float switch liquid level sensor circuit (bottom) 52
35 Pressure relief, set to 60 PSI 54
36 Rendering of the liquid film thickness measurement optical setup with test section 55
37 Ray trace of light ring formation 58
38 Film thickness optical setup 59
39 Pixel calibration using grid paper 60
40 Left: Raw image of dry light ring; Right: MATLAB radius measurement 61
41 Left: Raw image of film thickness light ring; Right: MATLAB radius measurement 62
42 Film thickness for six steady state vapor flow rates 63
43 Film thickness with 1Hz pulses, 15W heated data 64

44 Film thickness data, 0 Hz (steady), 6000 fps 65

45 Film thickness dry calibration measurements 66

46 CAD rendering of the wall temperature measurement optical setup . . . 67

47 Refractive index of liquid water and liquid R245fa as a function of temperature, with curve fit for R245fa data, [13], [2] 70

48 Trace of rays reflected off of a glass and liquid R245fa interface over a 1.5 degree range of angles just before the critical angle, shown as lines getting darker for increasing angle, material thickness not to scale 72

49 Calculated intensity of light reflected and transmitted at an interface of glass and liquid R245fa (Figure 48) at varying angles of incidence near and at the critical angle, shown with lines getting darker with increasing angle 74

50 Simplified wall temperature optics setup, shown from above with components labeled 75

51 Test section optics with laser beam path, dimensions not to scale and light ray angles exaggerated 76

52 Effects of a few of the curve fitting parameters (input angle of incidence, background light, and frustrated total internal reflection), final curve shown by the dark, solid line 80

53 Calibration data with reflectance model curve fit, applied using parameters from Table 10 81

54 Normalized wall temperature variation with liquid film thickness 82

55 Calibrated wall temperature vs time, measured intensity ratio converted to wall temperature using the calibration reflectance model curve (Figure 53) 83

56 0.5 Hz pulsed, 20W heated data 87

57 3 Hz pulsed, 20W heated data 88

58 Film thickness for 0.5 Hz pulsed, 20 W heated data 88

59 Film thickness for 4 Hz pulsed, 20 W heated data 89

60 Average film thickness and the standard deviation for different pulsing frequencies 90

61 Wall temperature for 0.5 Hz pulsed, 20 W heated data 90

62 Average wall temperature with fluctuations of +/- 2 standard deviations for different pulsing frequencies 91

63 Normalized temperature for 0.5 Hz pulsed, 20 W heated data 91

64 Normalized temperature for 3 Hz pulsed, 20 W heated data 92

65 Normalized temperature for 7.5 Hz pulsed, 20 W heated data 92

66 Normalized temperature for 10 Hz pulsed, 20 W heated data 93

Nomenclature

Symbol	Description
α	input angle of incidence at prism
κ	extinction coefficient
$\theta_{\text{crit-gv}}$	critical angle at the glass-vapor interface
$\theta_{\text{crit-lv}}$	critical angle at the liquid-vapor interface
θ_i	input angle of incidence
θ_t	angle of transmittance
h_l	liquid film thickness
$i\kappa$	imaginary component of index of refraction
I_{in}	light intensity from test section optics
I_{out}	light intensity into test section optics
n	real component of index of refraction
N_{R245fa}	index of refraction of R245fa
n_i	refractive index of first material
n_t	refractive index of second material
q''_{in}	heat flux at the wall
r	radius of wet light ring
r_o	radius of dry light ring
R_p	p-polarized Fresnel coefficient
R_s	s-polarized Fresnel coefficient
T_{sat}	saturation temperature
T_{wall}	wall temperature

T_p	p-polarized light transmitted
BK7	borosilicate-crown glass designation
CHF	critical heat flux
EES	Engineering Equation Solver
FFT	Fast Fourier transform
FNPT	female national pipe threads
FT	film thickness, abbreviated figure label
FTIR	frustrated total internal reflection
FTO	Fluorine-doped Tin Oxide
HeNe	helium-neon laser
HTC	heat transfer coefficient
ID	inside diameter
MFVAL	Multiphase Flow Visualization and Analysis Lab
MNPT	male national pipe threads
NPT	National Pipe Threads
OD	outside diameter
PDE	partial differential equation
PG MF	pulse generator vapor mass flow rate, abbreviated figure label
PLIF	planar laser induced fluorescence
POE	polyolester compressor oil
PSD	Fast Fourier transform power spectrum density
PTFE	polytetrafluoroethylene (Teflon)
R	light reflected
T	light transmitted
TIFF	tagged image file format
WT	wall temperature, abbreviated figure label

1 Two-Phase Flow

Two-phase flow is conventionally defined in fluid mechanics by a flow consisting of a liquid and a vapor phase. The type of flow can be further categorized into flow regimes, based on the flow direction, orientation, and the void fraction. In addition to multiple phases, the flow can also contain multiple species and different levels of stratification. Single-species, two-phase flows can be found commonly in boiling, evaporating, and condensing applications.

1.1 Annular Flow

Annular flow (depicted in Figure 1) is a specific, separated two-phase flow regime, characterized by a liquid film on the channel wall and a continuous vapor core at the center of the channel. Vapor bubbles may exist within the liquid film and liquid droplets can be entrained within the otherwise vapor core. Annular flow is associated with high mass fluxes [35]. A few common applications which contain annular flow include steam generators, evaporator coils, and chemical reactors.

The liquid film in an annular two-phase flow is driven by the momentum transfer between the fast-moving vapor and the liquid [9]. The interfacial shear between the two phases creates a wavy interface and the vapor, if it reaches a sufficiently high velocity, can shear the tops of the waves and entrain more liquid. The increase of liquid in the core results in an increase in the core density and consequently the friction factor of the flow [34].

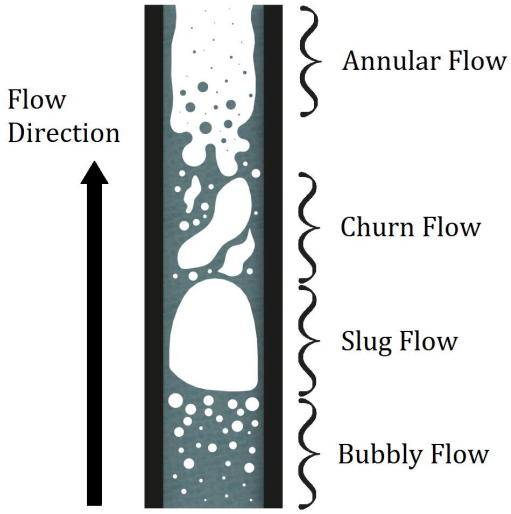

Figure 1: A few patterns for vertical two-phase flow regimes, given by Hewitt and Hall-Taylor [8] and consolidated into a single graphic

1.1.1 Heat Transfer Coefficient

In an annular two-phase flow, the liquid film is sheared between the fast-moving vapor core and the fixed channel walls. This develops a high shear stress within the liquid film [33] and provides a higher heat transfer coefficient between the wall and the flow compared to other boiling flow regimes. Thinning of the liquid film further increases the heat transfer coefficient [24]. Hurlburt and Newell [9] developed a model for calculating the heat transfer coefficient of annular two-phase flows. Kim et al. [24] developed a model for the local heat transfer coefficient of annular two-phase flow in micro-channels.

In order to experimentally measure the heat transfer coefficient (Equation 1) measurements of the wall temperature (T_{wall}) and saturation temperature of the flow (T_{sat}) as well as knowledge of the heat flux to the flow (q''_{in}) are required.

$$\text{HTC} = \frac{q''_{\text{in}}}{T_{\text{wall}} - T_{\text{sat}}} \tag{1}$$

1.1.2 Pulsatile Flow

Pulsating annular two-phase flow can occur in applications with parallel boiling channels. Oscillations complicate the study of annular two-phase flow and the resulting heat transfer coefficient. The film thickness and mass flow rates are no longer steady, which leads to an unsteady wall shear stress and heat transfer. The thermal mass of the flow duct can no longer be neglected. Measurements must also be taken at a higher sampling frequency in order to study the effects of the pulsations.

Furthermore, the critical heat flux (CHF) of the flow decreases as the flow becomes oscillatory [32]. Once CHF is reached, the heat transfer coefficient drops considerably [24], [28]. CHF effectively poses a limit on the maximum heat transfer possible by the flow and can cause thermal runaway and a catastrophic failure if it occurs. The CHF and liquid film dryout in boiling channels and of annular two-phase flow have been studied [27], [32], [25] in applications using water and steam. Work has been done to predict the onset of critical heat flux in annular two-phase flow [26]. Post-dryout conditions and rewetting have also been studied for boiling flows [31].

Instantaneous, time-synchronized measurements of the wall temperature and film thickness can be used to analyze the relationship between the wall temperature, film thickness, and pulsing frequency. These results can further be used to calculate the instantaneous heat transfer coefficient of annular two-phase flow.

2 MFVAL Annular Flow Facility

The Multiphase Flow Visualization and Analysis Laboratory (MFVAL) was established by Dr. Tim Shedd in 2001 at UW-Madison and has housed several multiphase experiments since its creation. Current experiments include studying the pressure drop along a horizontal bubbly flow, steam injection into liquid pipe flow, and studying vertical two-phase annular flow. Only the Annular Flow facility will be discussed here. For additional details concerning the Annular Flow facility, see [3] and [4]. The pulse generator, test section assembly, and the temperature and film thickness measurements are shown in the rendering, Figure 2.

The Annular Flow facility consists of a heat pump loop, a refrigerant loop, a developing flow and test section, and a refrigerant boiler (pulse generator). These components allow the facility to generate vertical annular two-phase pulsatile flow using R245fa refrigerant as the working fluid.

2.1 Water and Glycol Heat Pump Loop

The water and glycol heat pump loop (shown in Figure 3) is the driving system of the MFVAL Annular Flow facility. The heat pump loop provides heating and cooling for vaporizing and condensing refrigerant and generates the pressure differences necessary for developing flow.

A mixture of water and glycol is circulated through the cold and hot sides of each heat pump and stored in each side's respective tanks (Figure 3). The mixture is pumped through heat exchangers which condense and evaporate refrigerant in the separate R245fa

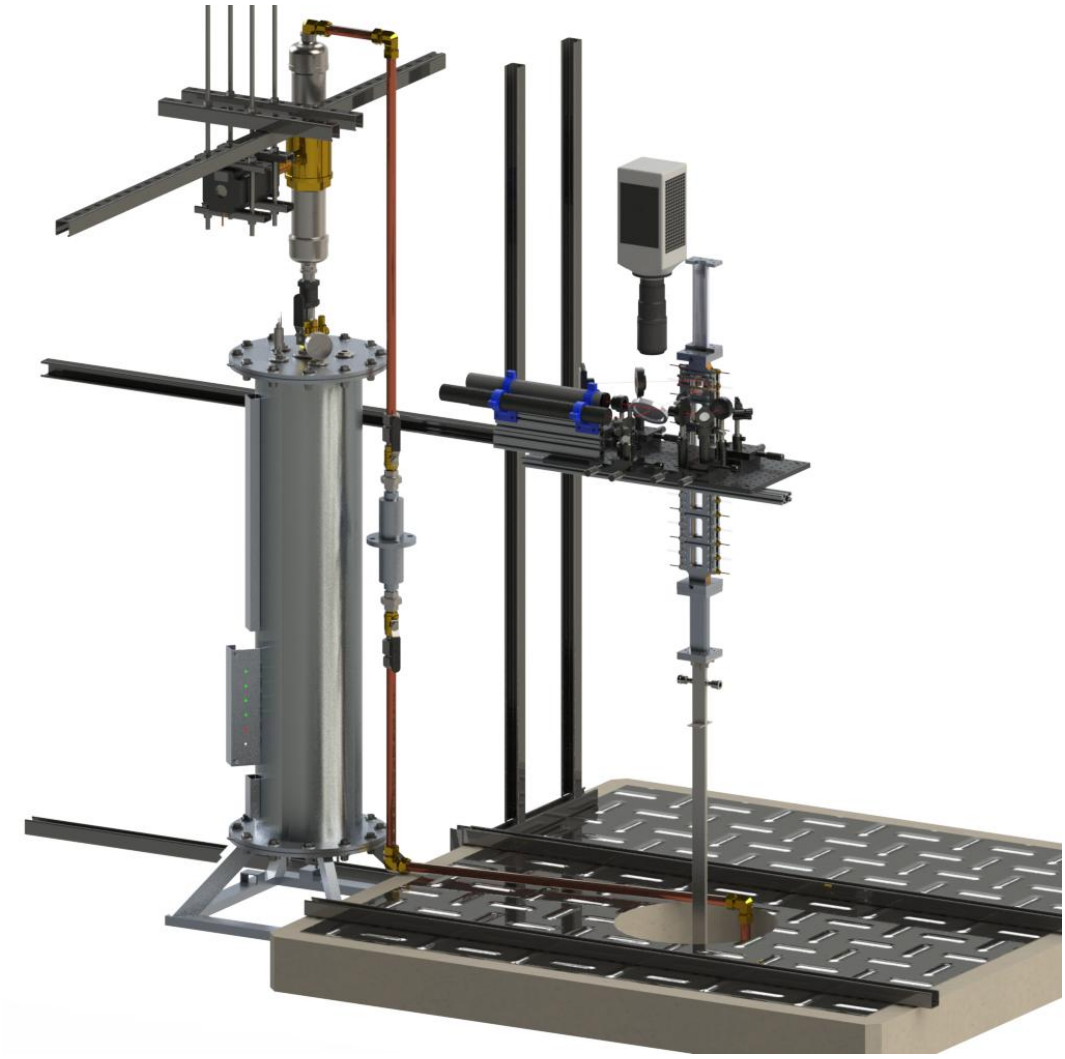

Figure 2: Rendering of Annular Flow facility pulse generator and test section assembly

refrigerant loop (shown in next section, Figure 4). The refrigerant heat exchangers are labeled in Table 1 and numbered in both facility schematics. Water and glycol in the hot loop are pumped through two water-cooled heat exchangers (top of Figure 3) which are actively cooled when the hot loop reaches a set maximum temperature.

The operating temperatures of the hot and cold sides of the heat pumps are currently set to 42 °C and 11 °C, respectively. The flow has been reasonably steady using these

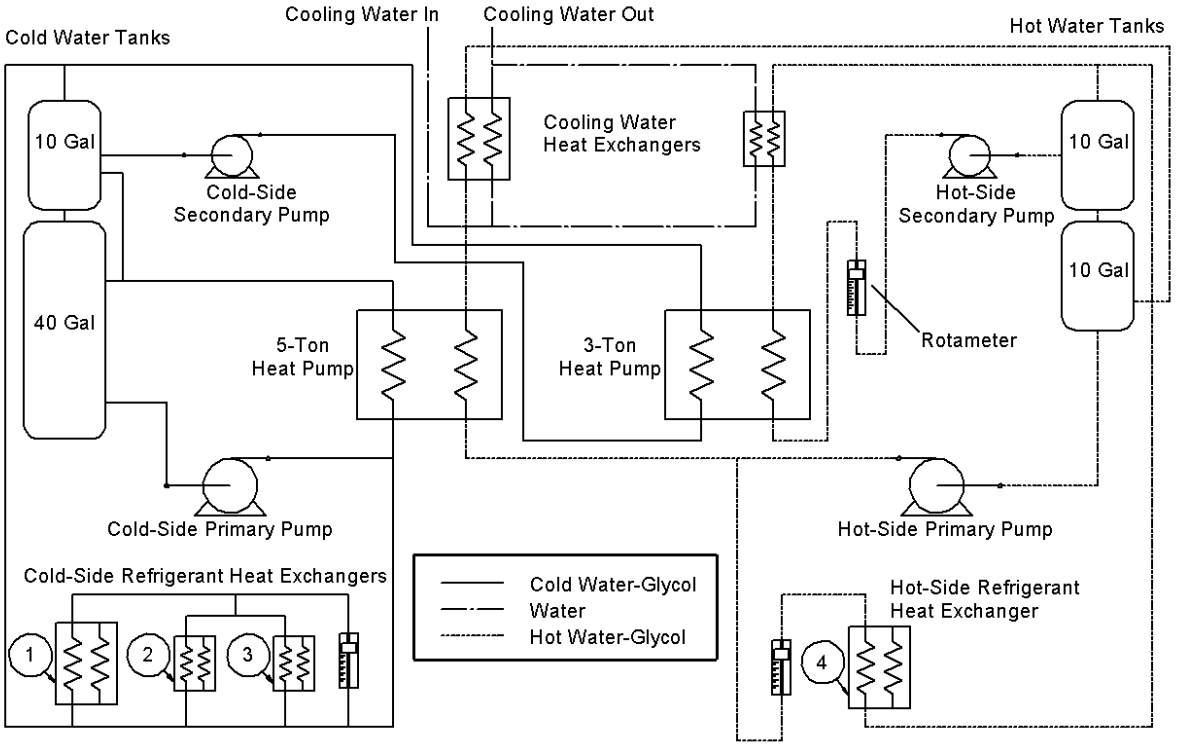

Figure 3: Schematic of the MFVAL water and glycol heat pump loop

Table 1: Labels for refrigerant heat exchangers shown in both Figures 3 and 4

Label Number	Heat Exchanger Function
1	Refrigerant Condenser
2	Vapor-Side Subcooler
3	Liquid-Side Subcooler
4	Refrigerant Vaporizer

temperature settings. At one point, the hot and cold side temperatures were set to around 45-50 °C and 5 °C, respectively, which caused uncontrollable oscillations in the test section. Steady flow rates were impossible to maintain, and the liquid film consistently reached dryout with these set temperatures. Bringing the set temperatures closer to each other, but still maintaining subcooled liquid and superheated vapor, prevented the oscillations and again allowed steady flow rates.

The heat pump loop contains roughly 50 gallons of an 85/15 water/propylene glycol mixture in the cold loop and around 25 gallons of 90/10 mixture in the hot loop. Previously, the heat pump loop used a mixture of ethylene glycol and tap water. In the interest of safety, ethylene glycol was replaced with propylene glycol. In an effort to reduce corrosion, especially in the hot side liquid tanks, distilled water was used to fill the loop instead of tap water. To best prevent corrosion, the 10-gallon compressed air tanks (Manchester Tank catalog # 304937) used for storing the liquid should be replaced with internally-coated water tanks, intended for use with liquids.

The heat pump loop was upgraded in early 2018 for increased cooling capacity. Two 3-ton, water-to-water Trane heat pumps (model # WPWD07230D22000T) powered the water and glycol loop until one of the heat pumps started to fail in late 2017. With only one fully working 3-ton heat pump, the refrigerant flow loop temperatures and pressures would slowly increase uncontrollably while generating two-phase flow. The broken heat pump was replaced with a 5-ton water-to-water Trane heat pump (model # EXWE06031B00A000D0). A 40-gallon tank was installed to replace one of the two, 10-gallon cold liquid storage tanks. The massive increase in cooling capacity and storage has since provided excellent temperature control of the refrigerant flow loop.

2.2 R245fa Refrigerant Loop

The R245fa refrigerant loop (shown by the schematic in Figure 4) is the testing and data collection loop of the MFVAL Annular Flow facility. Refrigerant liquid and vapor are mixed and developed into an annular two-phase flow for analysis in the test section.

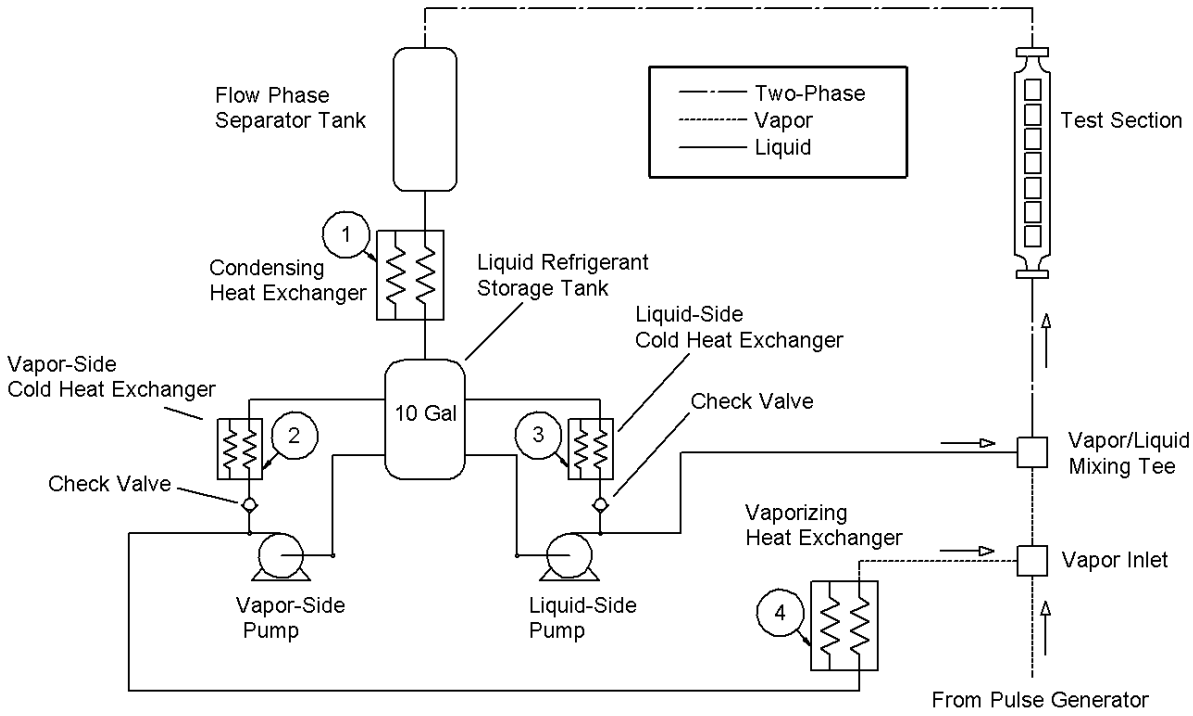

Figure 4: Schematic of the MFVAL R245fa refrigerant loop

R245fa refrigerant is the working fluid used in the refrigerant loop. With a boiling point of 15.3 °C at atmospheric pressure, R245fa can be both boiled and condensed using a standard industrial heat pump. The refrigerant is condensed using a cold heat exchanger and stored in a 10-gallon compressed air tank (Manchester Tank catalog # 304937). The subcooled liquid refrigerant is divided into a liquid-side and vapor-side loop from the storage tank. Refrigerant in the vapor-side loop is pumped through a vaporizing heat exchanger (label 4, Figure 4) and injected into a pipe tee as a superheated

vapor. Refrigerant in the liquid-side loop is pumped into the vapor/liquid mixing tee just before the developing flow section (both discussed in later sections). After mixing, the multiphase refrigerant flow develops into vertical annular two-phase in the development section. The flow is studied in the test section before entering the separator plenum tank. Refrigerant in the separator tank is condensed back to a subcooled liquid in the condensing heat exchanger (label 1, Figure 4) and is again stored in the refrigerant liquid tank to repeat the cycle.

The liquid mass flow rates of the vapor and liquid sides are controlled and measured individually. Two Cole-Parmer (model # 07002-21) centrifugal pumps, powered by two Cole-Parmer (model # 75211-62) variable speed drives, are used to pressurize the vapor-side and liquid-side loops. Under normal operation, each pump is driven at a constant speed and the flow rates are changed through a LabVIEW program which controls two Omega (model # ECV-2506-4X) control valves. The liquid mass flow rate in each line is measured by an Emerson Micro Motion (model # F025S121CQBMEZZZZ) and monitored and recorded by the same LabVIEW program. When the control valves are closed, liquid is forced through the check valves and circulated through the cold heat exchangers (labels 2 and 3, Figure 4). This system was intended for use with proportional-integral-derivative (PID) control in LabVIEW, but this was never successfully implemented.

Control of the liquid and vapor mass flow rates has been imprecise with the variable displacement pumps and control valves. The minimum control step size for the mass flow rates is about 4 g/s and both the liquid and vapor flows oscillate about +/- 3 g/s, shown in Figure 5. The minimum mass flow rate step size is limited by the step size of the Omega control valve stepper motors. Finer control could be achieved by installing a gearbox between the motor and valve, but this would decrease the maximum flow rate. Oscillations in the flow rates could possibly be remedied by replacing the centrifugal

pumps and control valves with positive displacement pumps in the future.

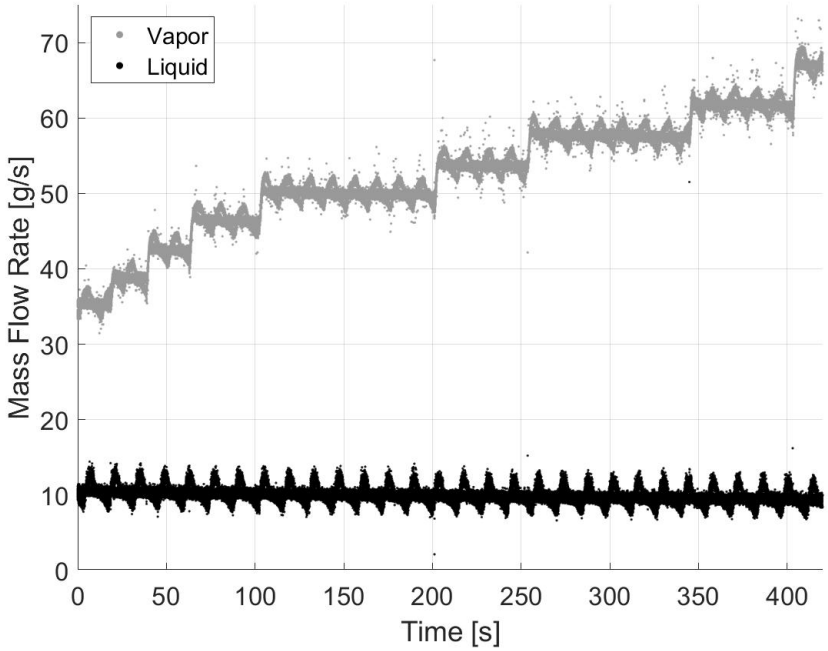

Figure 5: Vapor and liquid mass flow rates during a temperature calibration

The refrigerant storage system was consolidated in 2017 to eliminate pressure and liquid level imbalances between the liquid and vapor sides. Previously, the separator plenum tank was used to separate the vapor and liquid phases into individual 5-gallon liquid storage tanks. This configuration was likely implemented for future experiments using particle image velocimetry (PIV), but caused issues with liquid level, pressure, and flow imbalances. Theoretically, each side would have maintained the same mass of refrigerant with the vapor and liquid separating in the separator tank and flowing into the respective loops. However, the liquid-side tank emptied more quickly than the vapor-side tank. The vapor-side tank also cooled more effectively, which caused a pressure imbalance between tanks and forced liquid from the liquid-side tank to the vapor-side. Both tanks were replaced with a single 10-gallon storage tank (Manchester Tank catalog # 304937). Consolidating the liquid storage resolved the imbalances but did not fix the

unsteady mass flow rates.

2.3 Mixing Tee

Annular two-phase flow is artificially developed in the mixing tee by injecting small streams of liquid into a flow of vapor. Subcooled liquid is pumped into the mixing tee by the liquid-side pump and enters the vapor flow through holes in the pipe, shown in Figure 6. This method is able to produce annular flow in a much shorter pipe length than either boiling or condensing a flow until it naturally progresses through the other flow regimes (Figure 1). The two-phase mixture continues through the developing flow section before reaching the test section.

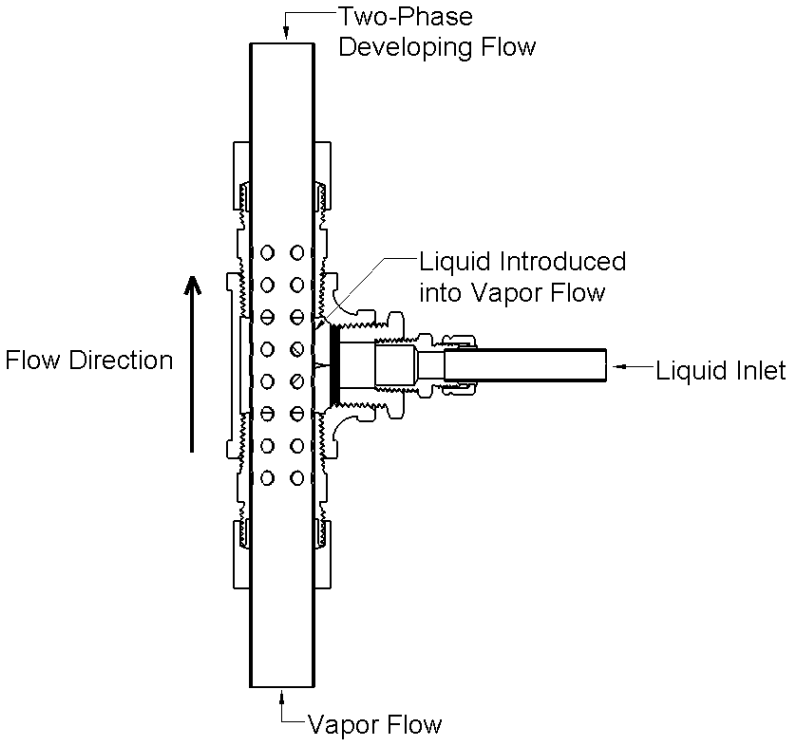

Figure 6: Vapor and liquid mixing tee

2.4 Developing Flow Section

The current developing flow section consists of three main parts which provide both a smooth transition between round and rectangular geometry and a sufficient length for the annular flow to become fully developed. The entire developing flow section was replaced in 2017 in order to fix leaks, increase rigidity, improve alignment, and add sensors.

2.4.1 Main Development Section

The main developing flow section, as its name suggests, is the primary development length for the vertical annular flow. The current main development section, shown in Figure 7, replaced two sections made of plastic with a leak-tight, rigid, stainless steel section with additional sensor capabilities.

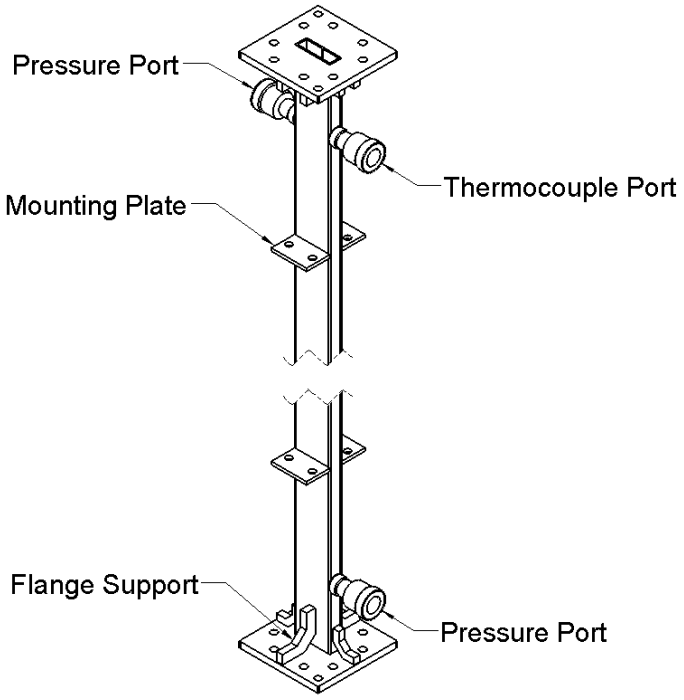

Figure 7: Main development section

History

The previous main development section was constructed from two sections in order to obtain a sufficient development length from available materials. Each section was built from 4 separate sheets of PVC, milled to size and bolted together along the length of the shorter edge, shown in Figure 8. The sheets were glued at the seams and plastic flanges were attached at the top and bottom of the duct using epoxy. The first section was reinforced along the wider side with aluminum plates, held on using the same bolts. Two threaded rods were extended between and through flanges on opposite corners and tightened with two nuts against each flange. The threaded rods were intended to add rigidity to the weak plastic assembly and structurally link the two development sections. An additional aluminum flange was used between the two development section plastic flanges, possibly to provide a better O-ring seal.

Redesign

Replacement of the old development section was warranted due to significant refrigerant leaks and questions of duct alignment between flanges. The previous development sections leaked along the glued corners. Epoxy was added along the seams (Figure 8) as a temporary fix but leaks continued to form. In order to prevent leaks from the new main development section, a single 5-ft stainless steel tube was chosen, and the pipe flanges were welded to the tube. To facilitate alignment of the internal flow ducts, two holes with tighter tolerances were added at opposite corners of the pipe flanges for locating pins. However, the holes were cut too large by the water jet to be used for locating pins. The flanges for both the development section and development-test section converter were cut using the water jet and held the same dimensions between features. This allowed

Figure 8: Single section, previous main development section

the alignment of the inside duct through alignment of the outer edges of the flanges. The flange faces were also welded to the tube and sanded flat to provide a smooth and uniform sealing surface.

Several additional pieces were welded to the base structure of the development section for adding strength and sensing capabilities. Flange supports were originally designed for aligning the face of the flange plate at a 90°angle to the rectangular tube. A fixture table was used to align the pieces but the supports were still welded to the development section (Figure 7) to provide extra support to the flanges against bending and prevent excessive distortion of the flange faces during welding. Four small plates

with 0.25-inch holes were welded to the long side of the rectangular tube for rigidly mounting the development section to the testing structure. For adding sensors to the development section, three 0.030-inch holes were drilled into the development section tube and 3/8-inch FNPT to 1/8-inch FNPT pipe reducer fittings were welded at each hole location. Two fittings were added near the top of the tube for a pressure transducer and a thermocouple while a fitting was added near the bottom for a second pressure transducer.

Prior to installation, the development section was pressurized with air to 30 psig and tested for leaks. Since installation and through all subsequent operation, no leaks have been found on the development section.

2.4.2 Development to Test Section Transition

Although the internal dimensions of the development section stock steel tube were close to the internal test section dimensions, each side was short by about 0.04 inches (1.02 mm). Because the annular flow film thickness is only 150 µm (0.006 inches) or less, this step would have been significantly disruptive to the thin liquid film. A transition section (Figure 9) was therefore constructed to smooth out the sharp internal step along 6 inches of duct length and merge the internal walls of the development section to the test section.

Aluminum 6061 was the material chosen for the converter section due to the ease with which it can be machined and welded. The conversion section was machined from two 0.5x2x6-inch blocks and welded together along the edge of the short side. Two 0.5-inch flange plates were cut using a water jet to match the internal dimensions of the appropriate side and test section bolt hole pattern. An O-Ring groove was later machined in each flange for sealing against the main development section and the test section. Two

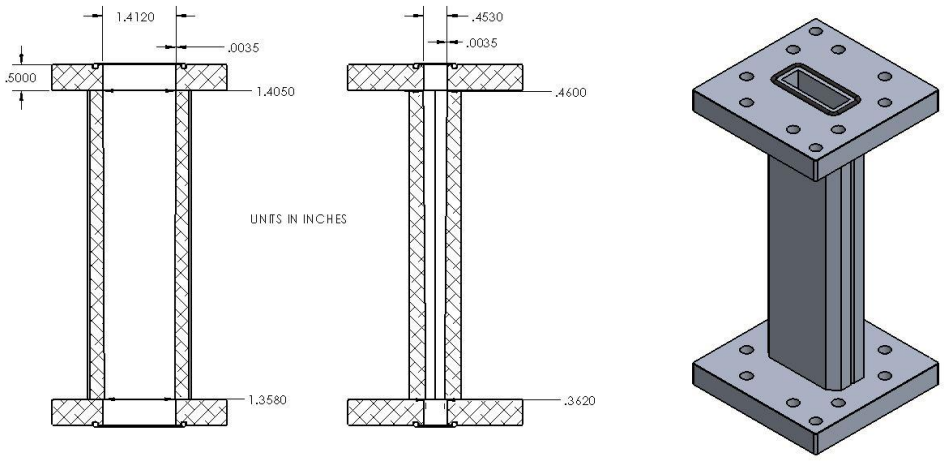

Figure 9: Development section to test section internal duct converter

locating pin holes were cut with a water jet on opposite corners for alignment with the development and test sections, but were again not used in the final installation. The flange plates were butted up against the converter section and welded around the outside edge.

If a new test section is constructed, the development to test section converter may not be necessary. The internal dimensions of the new test section could be designed to fit the current development section without requiring a transition piece. A new development section could also be easily made in tandem with the new test section, to ensure proper alignment of the internal flow duct.

2.5 Pipe Transition Sections

With the exception of the developing flow section and the test section, round pipes and hoses of standard dimensions were used for all facility plumbing. Two flow converters, machined from plastic, were used previously to transition between a round and rectangular flow duct. The flow converter connected to the test section could no longer hold pressure and the converter connected to the development section did not match the internal dimensions of the replacement developing flow section. Two new flow converters (Figure 10) were made to fix these issues.

Figure 10: Left: Test section to round pipe transition; Right: round pipe to development section transition

The test section to round pipe transition was machined from two 1.5x3x8-inch pieces of aluminum. The inside profile was machined to match the test section dimensions on

one side and a 1-inch round pipe on the other side and smoothly transition the two sides together. The outside of the blocks was machined to produce a flange on one side for attaching to the test section flange. The two pieces were then welded together on the outside seam. The top and bottom seams of the converter were also welded and then machined to produce smooth and leak-proof faces. A 1-inch FNPT thread was cut into the round pipe side for attaching a fitting. Finally, an O-ring groove was machined into the surface of the flange to provide a tight seal with the test section flange.

The round pipe to development section transition (Figure 11) was machined out of two 0.75x1.75x8-inch pieces of aluminum. The internal profile was made nearly the same as the test section pipe transition, except the rectangular profile was made to match the new development section rather than the test section. The two pieces were welded together on the outside seam. Two separate aluminum flanges were cut using the water jet then welded to the top and bottom of the converter to provide smooth mating surfaces. A 1-inch FNPT thread was cut into the round pipe side for attaching a fitting. An O-ring groove was machined on the top surface to provide a tight seal with the development section flange.

Both converters were tested to 30 psig and leak tested before installing. Since installation, no refrigerant has been found leaking from either transition section.

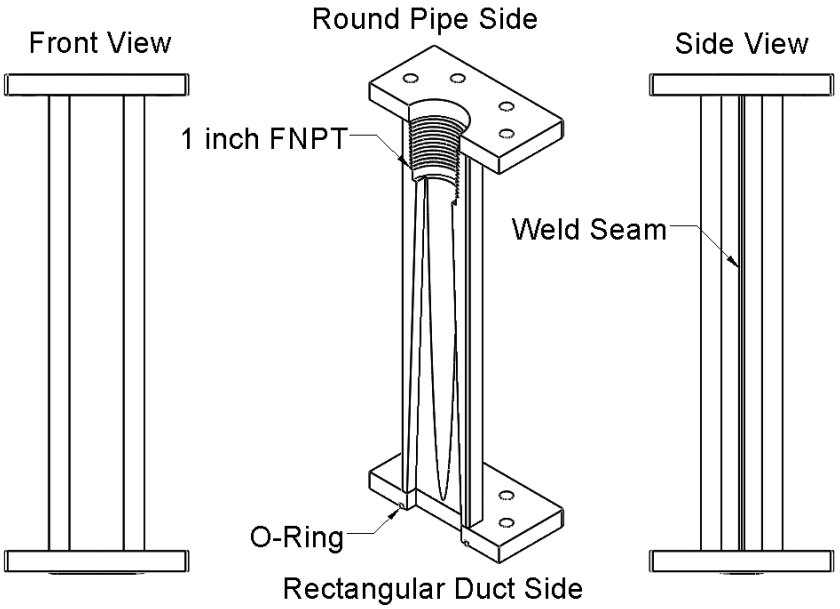

Figure 11: Round pipe to development section transition

2.6 Test Section

The test section is the focus of the Annular Flow test loop and the location where most of the measurements are taken. The test section is capable of heating the flow through electrically-conductive windows while maintaining optical access to the flow for light-based measurement techniques. Taps along either side of the test section (Figure 12) can be connected to pressure sensors or thermocouples.

2.6.1 Design and History

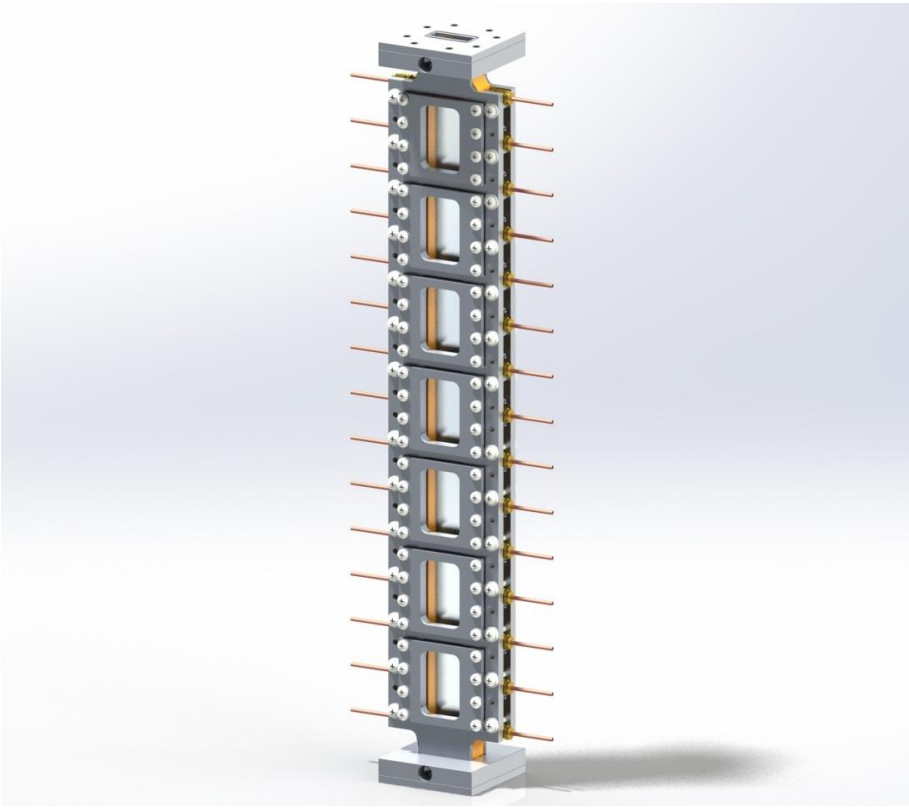

Figure 12: Annular Flow test section in 2016

Mechanical Construction

The testing section used for annular flow experiments through 2017, shown in Figure 12, was the same device designed and used by Mark Rodarte for his doctoral research. The test section consisted of 14, 75x50x3 mm float glass windows (3 - Figure 13) placed end to end to form a 525x50x3 mm duct. Two ULTEM (a formulation of polyetherimide, made by SABIC) spacers (5 - Figure 13) fit between the front and back windows and maintained a flow channel depth of around 12 mm (0.48 inches). An aluminum front and back main plate fixed the ULTEM spacers side to side and established a flow channel width of around 35 mm (1.39 inches). The internal flow dimensions were designed for a depth of 11.6 mm (0.457 inches) and a width of 36 mm (1.417 inches) [3]. An aluminum window flange (2 - Figure 13) was sealed against each window and a main plate (1 - Figure 13) to complete the flow containment. O-ring grooves were cut into the ULTEM spacers, main plates, and window flanges and silicone O-rings were used to seal the components together (shown by the red ovals in the section view, Figure 13). For more information on the design, construction, and function, see Mark Rodarte's PhD thesis [3].

The front and back main plates of the test section were held together by 28, 10-24 x 1 1/2-inch screws and the window flanges were mounted to the main plates by 8, 10-24 x 7/16-inch screws per flange. The main plates were designed for attachment by 56 screws, but only every other screw hole was used. The top and bottom of the test section were contained with aluminum blocks with an internal profile cut to fit the test section and 8 threaded holes for mounting the test section to the facility. Each block was attached to the test section with a set screw. A flange plate was attached to each block with red silicone sealant. The total height of the test section was roughly 24 inches.

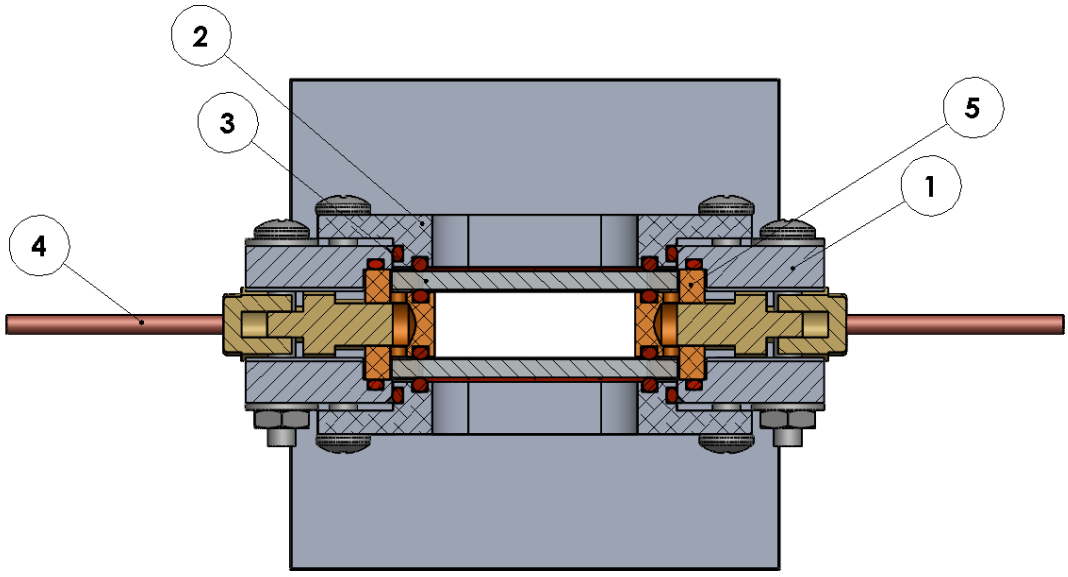

Figure 13: Section view of the test section; 1 - Main plate, 2 - Window flange, 3 - Float glass window, 4 - Pressure tape / wire lead, 5 - ULTEM spacer

Function

The float glass windows, purchased from Delta Technologies (model # CG-11FTO-S232), have a thin coating of fluorine-doped tin oxide (FTO) on one side. The coating resistance is rated at 9-11 ohms and is used to heat the inside wall of the test section. By adding a known heat flux at the wall and measuring the temperatures at the wall and the test section saturation temperature the heat transfer to the flow can be estimated.

2.6.2 2017 Changes

Minor changes and repairs were made to the original test section during 2017 to improve or restore function. The test section is shown in Figure 14, installed in the Annular Flow loop after the 2017 modifications and repairs.

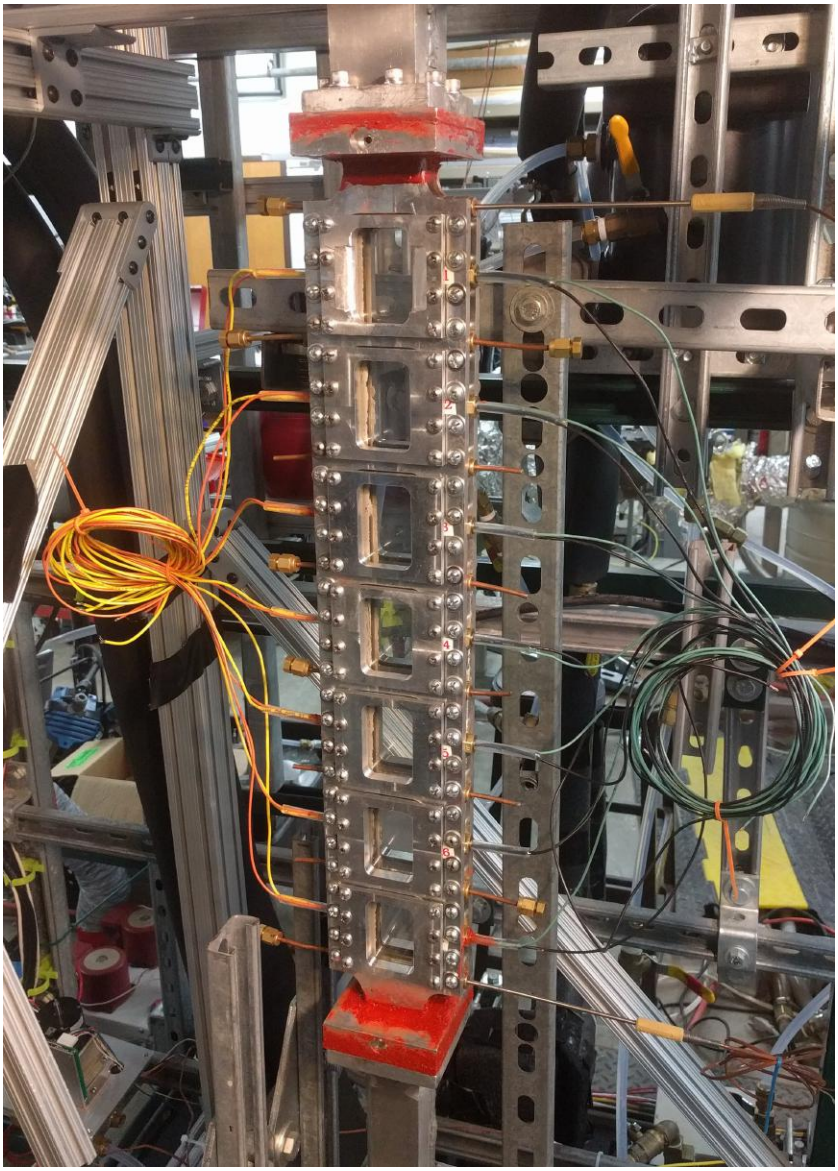

Figure 14: Annular Flow test section 2017-2018

A few of the test section components were repaired in 2017. The most significant repair to the test section was the manufacturing of new ULTEM spacers. One of the spacers broke while disassembling one of the wire and pressure tap fittings. New CAD drawings were made using Mark's thesis and by measuring the unbroken spacer. Two new spacers were machined out of spare ULTEM and installed into the test section without any noticeable issues.

The test section O-rings, fittings, and electrical wires were all replaced to improve the function and safety of the test section. Previously, red silicone was used for the O-ring material, but it is not compatible with R245fa [37]. EPDM O-rings were purchased from Grainger and used to replace the red silicone O-Rings. The window power wires were also replaced, along with the compression fittings which seal against the wire conduit. The 22 GA multi-conductor wires were replaced with 18 GA single-conductor hook-up wire to allow more current for heating the windows and to better seal against refrigerant leaking between the conductor and wire sheath. Larger compression fittings were installed to fit the larger tubes and wires. Epoxy was used to seal the space between the wires and the inside of the tubes. This prevented further refrigerant leaks from the tubes, but a small amount of refrigerant was still able to escape between the wire conductor and sheath.

Additional sensors were added to the test section in 2017. A thermocouple was installed at both window 1 (top) and window 7 (bottom) of the test section (shown in Figure 14) and a fast, absolute pressure sensor (Omega model # PX309) was installed on window 1 of the test section (not yet installed in Figure 14). The thermocouples have been used for calibrating the pressure sensors before collecting data. Previously, absolute pressure measurements closest to the test section were actually collected in the development section and at a very low sampling frequency. As a result, the test section saturation pressure was only reliably measured at steady flow rates. The fast response pressure sensor at window 1 allows the absolute pressure of the test section to be measured at 2000 Hz. The fast sample frequency has been particularly useful for measuring the test section saturation temperature during a wall temperature calibration (see Wall Temperature Measurements section).

The window flange for window 1 was modified slightly to accommodate the wall temperature measurement laser. The laser beam is directed at window 1 at a shallow

angle, which previously intersected the sharp angles on the inside of the window flange. The edge was filed round (Figure 14) to allow the laser beam to pass and reach window 1.

3 Pulse Generator

Applications of vertical, annular two-phase flow are not limited to steady flow conditions. Boiling, especially in a parallel configuration of pipes, can generate oscillations in the flow direction and change the behavior and properties of the flow, such as the liquid film thickness and resulting heat transfer coefficient. To study the effect of oscillations in an annular two-phase flow, a pulse generator was constructed and attached to the existing MFVAL refrigerant loop.

The MFVAL pulse generator is simply a pressure vessel capable of boiling, storing, and releasing pressurized refrigerant vapor in a controlled manner in order to simulate unsteady flow conditions. At steady state, boiling liquid refrigerant resupplies the tank with the vapor mass that it loses with each pulse, recharging it to the correct pressure. Pulses of refrigerant vapor are released from the vessel by using a stepper motor to rotate a ball valve attached to the top of the pulse generator. The pulsing frequency and amplitude of the pulses can be adjusted by changing the motor and heater settings, respectively.

3.0.1 History

The first MFVAL pulse generator, designed and created by Mark Rodarte, used an external heating source and a 3.2-gallon aluminum tank for storing the pressurized refrigerant. Prior to use, the tank was filled to about 1/4 capacity with liquid R245fa using the solenoid-controlled valve shown on the left side of Figure 17. The liquid refrigerant was then pulled from the bottom of the storage tank by a variable speed vane pump and cycled through 12, 3D-printed Ebullient modules. The Ebullient modules were attached

Figure 15: Cutaway rendering of the redesigned pulse generator installed in the MFVAL

to copper plates, which were heated using chip resistors. The boiling refrigerant flowed back into the storage tank and increased the pressure inside the tank. After a sufficient pressure had been obtained inside the storage tank, a valve connected to the tank outlet was rotated using a stepper motor. Pulses of vapor would flow out of the pulse generator storage tank with each half-turn of the valve.

The past pulse generator functioned correctly, but there were several mechanical limitations. Ebullient modules mounted on copper plates (which can be seen in Figure

Figure 16: Mark Rodarte's pulse generator

16) were used to effectively increase the surface area of the heat source and prevent critical heat flux when boiling the refrigerant. However, the use of Ebullient modules and external piping led to frequent refrigerant leaks. The 3D-printed plastic threads of the Ebullient modules were weak and broke easily when attaching fittings. The fittings needed to be checked daily before collecting data and leaks due to loose fittings were a common occurrence. On one occasion, an Ebullient module burst open while pressurizing the system to 220 kPa (absolute pressure). The heating system and tank size also limited the usefulness of the pulse generator. After a 10-pulse train, the pressure in the storage tank became too low to continue without stopping to boil more refrigerant and build up pressure again. Furthermore, even if the tank was large enough to sustain more pulses, the pulse generator still lacked any ability to control the heating power. The pressure

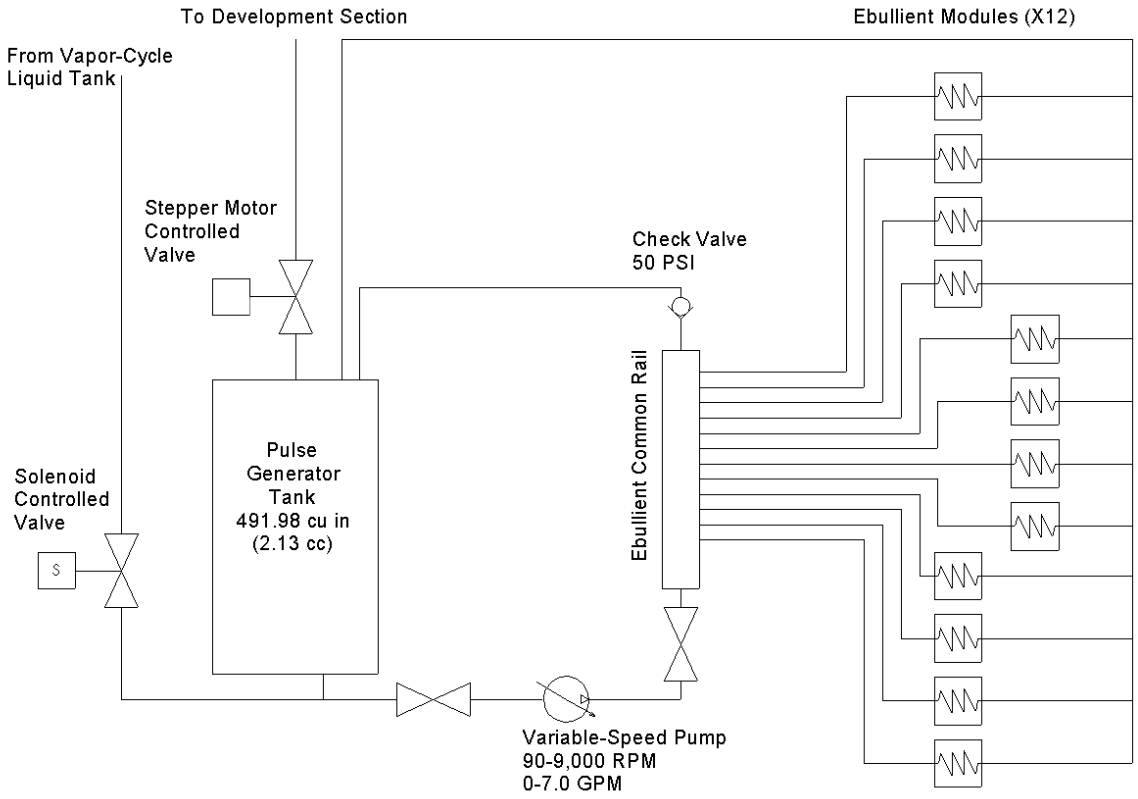

Figure 17: Schematic of the old pulse generator

and resulting mass flow rate of the pulses depended on the fixed heating power.

3.0.2 Thermodynamic Model

The previous pulse generator lacked sufficient heating power and tank volume to sustain long or repeatable pulse trains. Control over pulsing frequency was also difficult with the old system. The new pulse generator was designed to deliver pulses at controlled frequencies and amplitudes for long periods of time. The thermodynamic model for the pulse generator was developed using Engineering Equation Solver (EES) [17].

Maximum Heating Power

The first design criteria for the new pulse generator was maximum heating power. The heating element needed to boil refrigerant at a rate fast enough to sustain a steady flow of vapor at the maximum pulsing flow rate. In order to specify the maximum required pulsing vapor mass flow rate, mass flow rates from previous data sets were averaged and found to range between 12-20 g/s. Pulse amplitudes, even at a mass flow rate of 12 g/s, were quite disruptive of the liquid film in the test section, even to the point of forcing dryout. Smaller pulse amplitudes were desired for future tests to better observe the effects of film dryout caused by heat flux rather than the pulsed flow momentum. It was proposed that a vapor mass flow rate as low as 6-8 g/s would be sufficient for this study. However, an average pulsing vapor mass flow rate of 18 g/s was used as the maximum design condition to provide room for error and energy losses above the proposed mass flow range.

The maximum required heating power was calculated from the maximum pulsing vapor mass flow rate using the energy balance shown in Equation 2. The input energy ($\dot{Q}_{\text{in}}$) is equal to the enthalpy required to bring the subcooled inlet liquid to saturation ($h_{\text{liquid\_sat}} - h_{\text{liquid\_in}}$) and the enthalpy of vaporization of R245fa (h_{vap}) multiplied by the vapor mass flow rate out of the pulse generator ($\dot{m}_{\text{out}}$), after subtracting the energy lost in the system ($\dot{Q}_{\text{loss}}$).

$$\dot{Q}_{\text{in}} = \dot{m}_{\text{out}}(h_{\text{liquid\_sat}} - h_{\text{liquid\_in}} + h_{\text{vap}}) - \dot{Q}_{\text{loss}} \tag{2}$$

The enthalpies used in Equation 2 are shown in Table 2. These values were calculated using the Helmholtz energy equation of state [1] adapted for R245fa [36], programmed

in EES [17]. The liquid inlet temperature and pressure and the saturation pressure in the pulse generator were estimated based on measurements taken while operating the previous pulse generator. Thermal losses were not calculated at this stage but are discussed later in the 'Error Analysis' section. Ignoring system losses, the maximum required heating power was calculated to be around 3900 W for a vapor mass flow rate of 18 g/s.

Table 2: Input conditions used for calculating the pulse generator required input power

Condition	Label	Temperature [K]	Pressure [kPa]	Enthalpy [kJ/kg-K]
Liquid Inlet	liquid_in	285	250	215
Saturated Liquid	liquid_sat	-	220	247
Vaporization	_vap	-	-	184

Critical Heat Flux

Before the type of heating element could be chosen, concerns of reaching critical heat flux (CHF) needed to be addressed. Ebullient modules were used in the past to prevent CHF by means of liquid jet impingement boiling, but frequently caused issues with refrigerant containment and were inconvenient to maintain. In an effort to prove that a simpler, solid-state heater such as an immersion cartridge heater could be used instead of Ebullient modules, the CHF was calculated for several proposed geometries. CHF correlations in EES determined that the maximum allowable power density would be 177 W/in^2, far higher than even the most power dense cartridge heater chosen (64 W/in^2, Table 3). However, the use of aluminum sleeves (discussed in more detail in the 'Mechanical Design and Construction' section) was suggested to increase the surface area and provide a larger factor of safety. The critical power for a single cartridge heater with a 9-inch long sleeve and a diameter of 1.25 inches was calculated to be 6700 W, shown in Figure

18. Using a 1000 W cartridge heater (shown for reference on Figure 18) with a 1.25-inch diameter sleeve would provide a safety factor of 6.7:1. To further increase the factor of safety from CHF by increasing the boiling surface area, fins were welded to each of the sleeves.

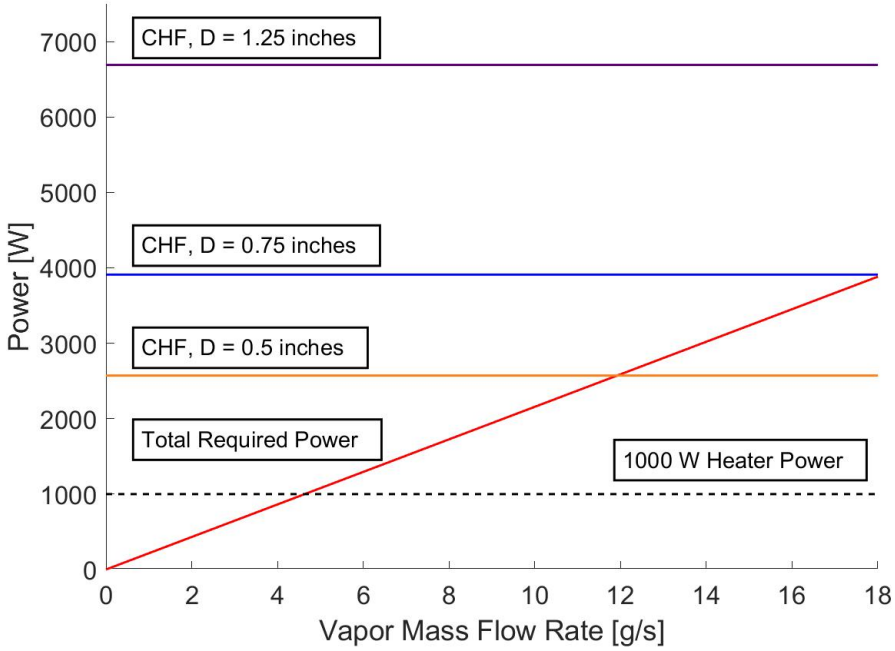

Figure 18: Total required heating power and critical power (per cartridge heater) as a function of target output vapor mass flow rate, geometries considered are 9-inch long cylinders with 0.5, 0.75, and 1.25-inch diameters

Variable Heating Power

After CHF calculations determined a maximum individual heater power, the remaining heaters were chosen to provide reasonable power steps up to the maximum total power. Three heaters rated for 1000 W at 240 VAC were chosen as the main heat source. Three more heaters rated for 500 W, 250 W, and 150 W at 240 VAC were chosen for precise adjustment of the total heating power. Controlling all six cartridge heaters allows oper-

ation at any heating power between 150 W and 3900 W, in increments of 150 W. This heating power step correlates to a vapor mass flow rate step of about 0.7 g/s.

Table 3: Cartridge heater rated power and size information

Rated Power [W]	Power Density [W/inch^2]	Diameter [inch]	Length [inch]
1000	57	0.75	8
500	28	0.75	8
250	64	0.5	3
150	41	0.625	2.375

Tank Volume

In addition to total heating power, the total tank volume of the old pulse generator (about 3.2 gallons) was estimated to be insufficient for pulsing stability, long pulse trains, and safety. The previous pulse generator was typically only used for 10 pulses at a time due to limitations in data collection. The first two pulses (out of ten) were quite large, with peaks up to 90 g/s, while the remaining eight were consistently much smaller, at peaks around 30-40 g/s. The old pulse generator was not tested for pulse trains longer than 10 seconds, but the ability to do so successfully was doubted. Even if a reasonable and steady vapor mass flow rate could be reached, the small amount of stored liquid would boil off too quickly to continue and there was no automatic system for refilling. If the previous tank was filled 1/4 with liquid, it would have only taken about 3.5 minutes to boil off the liquid at a vapor mass flow rate of 18 g/s. The new pulse generator was designed with a much larger tank, about 16.4 gallons, for storing a minimum vapor volume of 10.4 gallons and a maximum liquid volume of 6 gallons. The large volume was designed to reduce the pressure lost per pulse of vapor and increase the repeatability of the pulses. The mass flow rate of the new pulse generator (PG MF) is shown for a pulsing

frequency of 3 Hz over a 20 second duration in Figure 19. The pulse generator is capable of producing long and consistent pulse trains. The larger tank is also inherently safer because it pressurizes slower, allowing more time for the user to react before a dangerous situation can occur.

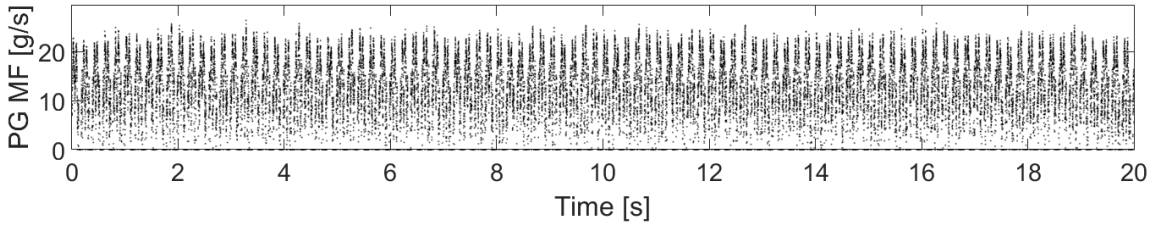

Figure 19: Pulse generator vapor mass flow rate at 3 Hz, data from 2018-6-20

Uncertainty Analysis

Several losses prevented the new pulse generator from operating at the design conditions described previously. All of the immersion cartridge heaters were rated for 240 V operation but only 205 V was available in the lab. The actual power provided by each cartridge heater is shown in Table 4 and the difference between rated and actual power resulted in a total heating power loss of about 1100 W.

In addition to the electrical power loss, some heat is also lost through conduction from the cartridge heater sleeves into the pulse generator base plate and frame. The sleeve walls were made thinner close to the baseplate to minimize this loss. However, the entire tank and frame are made from aluminum and act as a good conductor as well as a large heat sink. The thermal losses were not included in the model calculations but the effect can be seen by the loss in the vapor mass flow rate between the model and the collected data in Figure 20. The pulse generator vapor mass flow rate was calculated using the pressure differential measured by a Dwyer Pitot tube, located just before the stepper

motor-controlled valve. There may also be flow rate losses associated with overcoming the pressure in the test section, which is typically between 150-200 kPa absolute. Total losses effectively lowered the maximum vapor mass flow rate to around 8 g/s.

Table 4: Cartridge heater rated power at 240 V and actual power using 205 V available in the lab, corresponding total powers are roughly 3900 W rated and 2800 W actual

Rated Power [W]	Actual Power [W]
1000	706
500	372
250	186
150	109

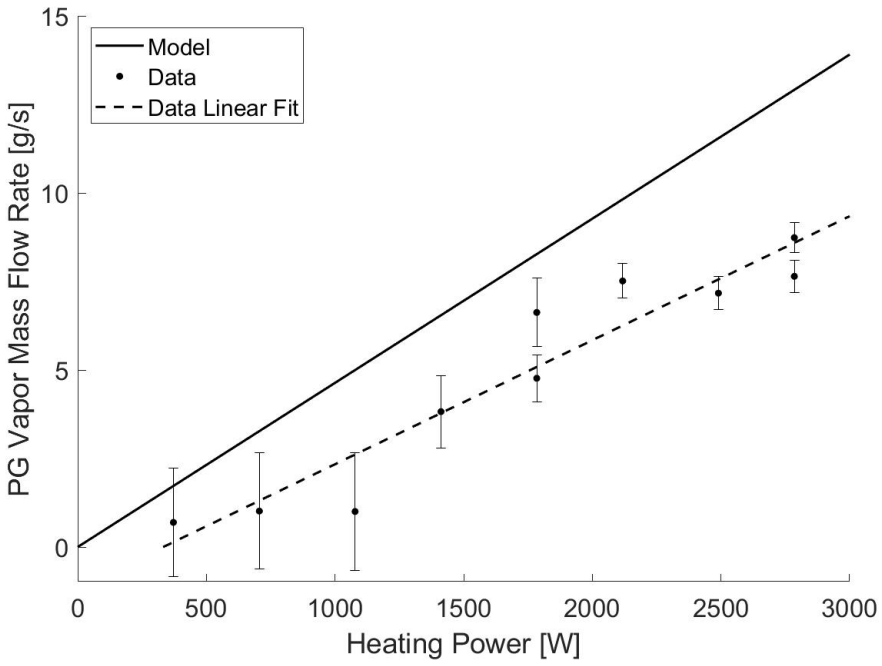

Figure 20: Pulse generator vapor mass flow rate model (Equation 2) and data collected on 2018-7-24

3.0.3 Heating Element Thermal Analysis

With the cartridge heaters chosen, a cartridge sleeve length needed to be chosen and verified. Criteria for the sleeve included reducing heat transfer to the base plate to prevent burning the flange-sealing materials while also keeping the heaters as low as possible in the tank to minimize the required liquid fill volume. A finite element analysis (FEA) was carried out in MATLAB using the Partial Differential Equation (PDE) Toolbox to estimate the steady state temperature gradient in the heater, sleeve, liquid refrigerant, and baseplate. An axial-symmetric geometry centered on one cartridge heater was chosen for the analysis and is shown with component labels in Figure 21, prior to meshing. The welded connections between the cap on the cartridge sleeve and between the sleeve and the base plate were modeled as one part. Following several simulations, a final cartridge sleeve length of 10 inches (9 inches above the baseplate) was chosen and used in the FEA model shown in Figures 21 and 22. The mechanical setup is shown in more detail in the 'Mechanical Design and Construction' section.

The outside liquid temperatures were set to 315 K for saturation at an operating pressure of 220 kPa. Contact resistance, boiling, and free convection values were estimated using EES. The FEA set conditions and assumptions are shown in Table 5 and the results are shown in Figure 22. The analysis estimated that the steady state temperature of the O-ring would remain well under the 420 K maximum operating temperature of EPDM. Further, the maximum temperature of the cartridge heater (1030 K) and of the thermal paste (473 K) would also be easily avoided. These results were reassuring, especially because the actual maximum temperature is likely lower than the FEA predicted. The FEA did not account for the additional surface area from the five fins added to each cartridge sleeve and the resulting decrease in thermal resistance between the sleeve and

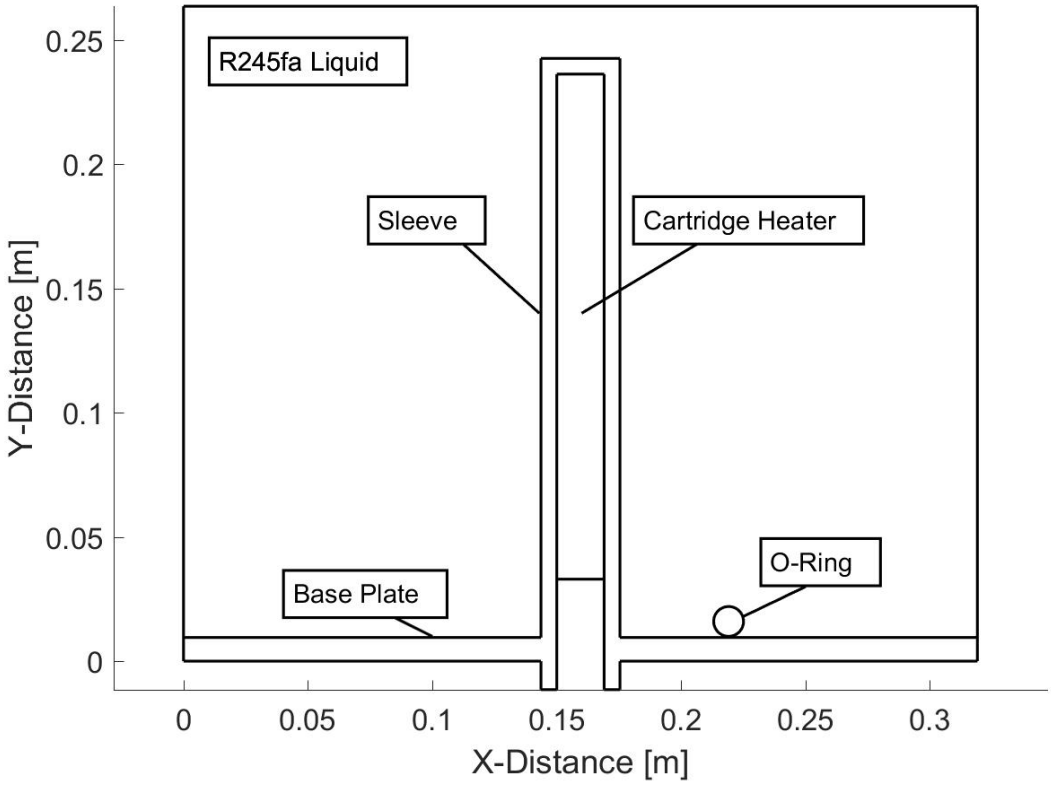

Figure 21: PDE Toolbox geometry for single cartridge heater and sleeve

the liquid. The top of the O-Ring is also in contact with the pulse generator tank flange which acts as a heat sink for the O-Ring.

Table 5: Cartridge heater sleeve finite element thermal analysis boundary conditions and settings

Boundary	Heat Transfer	Resistance [K/W]	Heat Flux or Temperature Setting
Inside Sleeve	Contact	0.01	226.5 [W/m-K]
Outside Sleeve	Boiling	0.0044	-
Bottom Baseplate	Convection	0.67	295 [K]
Top Baseplate	Convection	0.67	1.5 [W/m-K]
Outside Liquid	-	0.00001	315 [K]

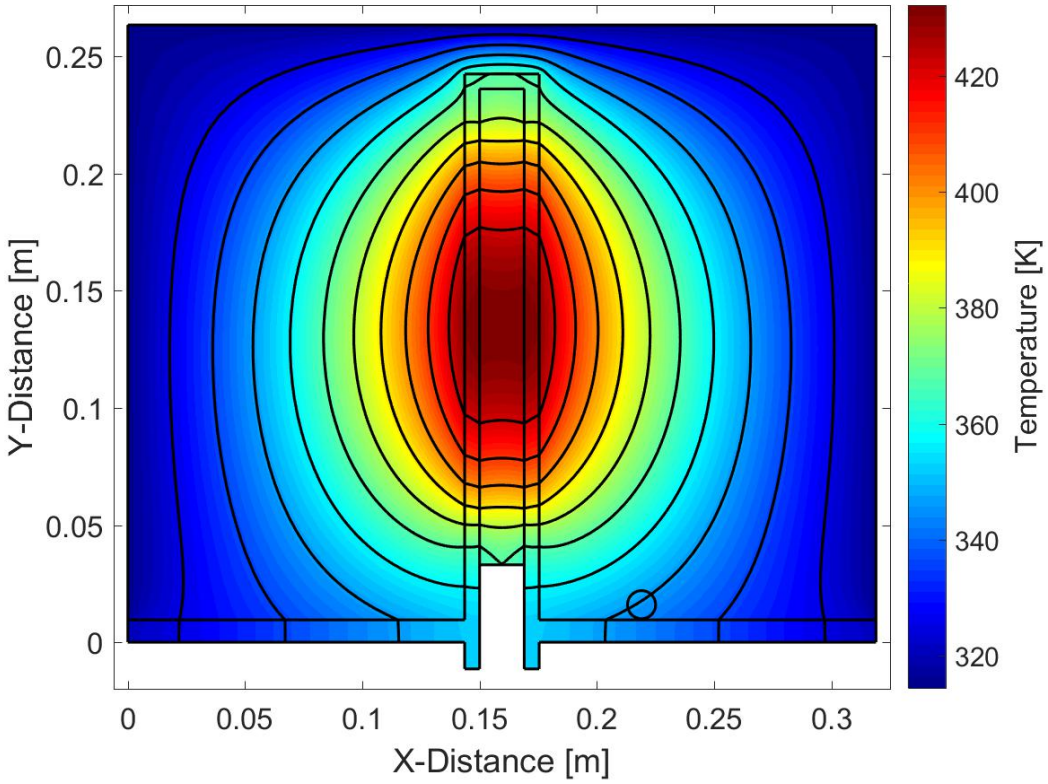

Figure 22: FEA results for a single cartridge heater and sleeve

3.0.4 Mechanical Design and Construction

The mechanical design of the pulse generator relied on the results of the thermodynamic model and thermal analysis to start. The next criteria were form and function, designing the pulse generator with sufficient ports for sensing, data collection, and refrigerant flow and allowing ease of assembly and maintenance. The remaining design criteria depended on practical manufacturing methods as well as commercial availability of the components. The finished pulse generator is shown in Figure 23 with all the major components labeled.

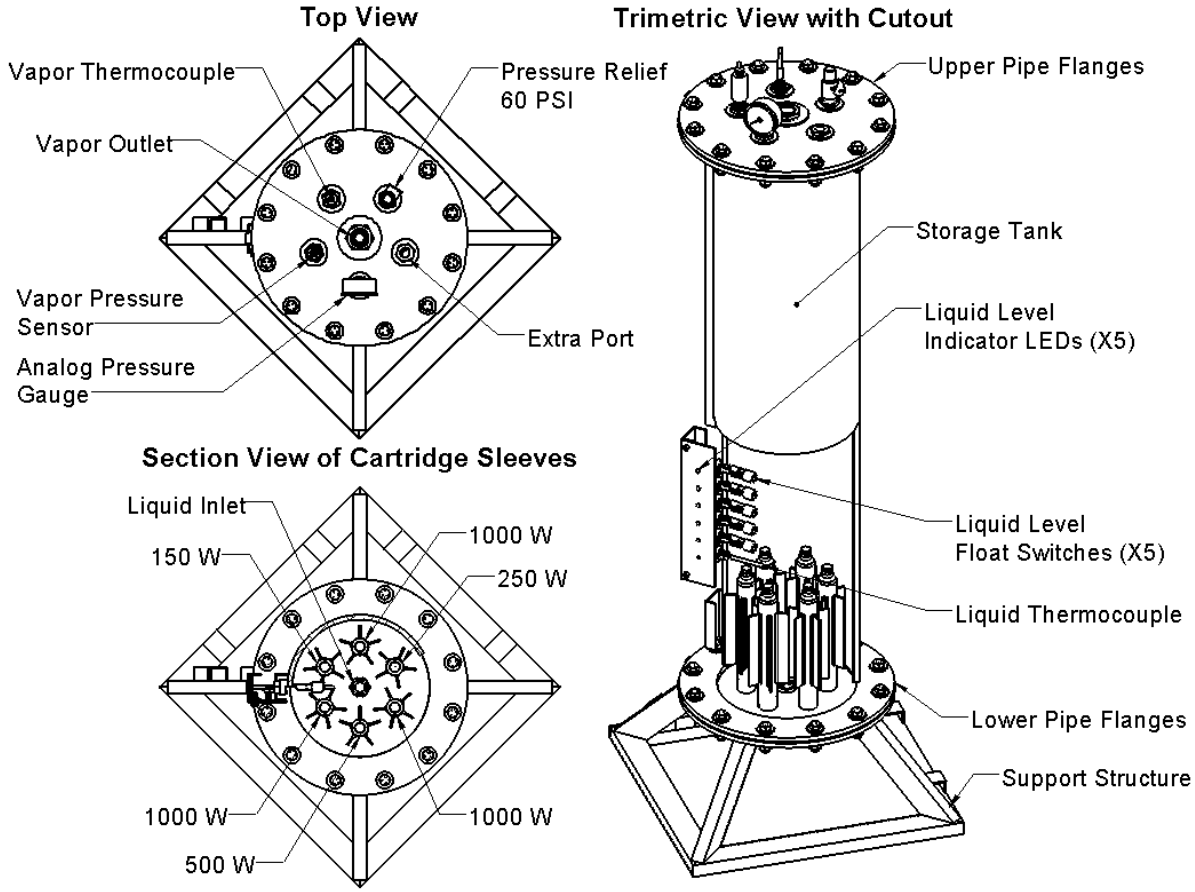

Figure 23: Cutaway views of the pulse generator with components labeled

Design of Operation

The new pulse generator was designed to operate functionally the same way as the old pulse generator. Both were designed to boil liquid R245fa refrigerant, store the pressurized vapor in a tank, and release the vapor in controlled pulses using a stepper motor controlled valve. The new pulse generator was designed to fulfill these functions with increased control, stability, and sensing capabilities.

Similar to the old pulse generator schematic (Figure 17), the new pulse generator was built with a storage tank, a vapor outlet with a stepper motor controlled valve above the tank, and a liquid inlet in the bottom of the tank (Figure 24). However, quite different from the old pulse generator, the heating elements were incorporated into the storage tank of the new pulse generator for simplicity and better reliability. Sensors were added to measure the level of the liquid refrigerant, the pressure and temperature of the vapor, and the temperature of the liquid (shown in Figure 24). An adjustable pressure relief (set to 60 PSI) was installed to vent vapor back to the separator in the event of excessive pressurization. The original design of the new pulse generator also included a solenoid-controlled valve on the liquid inlet line for automatic filling of the liquid volume when the liquid level float switches detected a low volume of liquid. However, this design was not implemented for favor of manually filling the tank.

Storage Tank and Flanges

Construction of the new pulse generator began with the storage tank. A 4-ft-long, standard 10-inch aluminum pipe provides the pulse generator with 16.4 gallons of internal volume. This was an increase of around 13.2 gallons from the old pulse generator. The

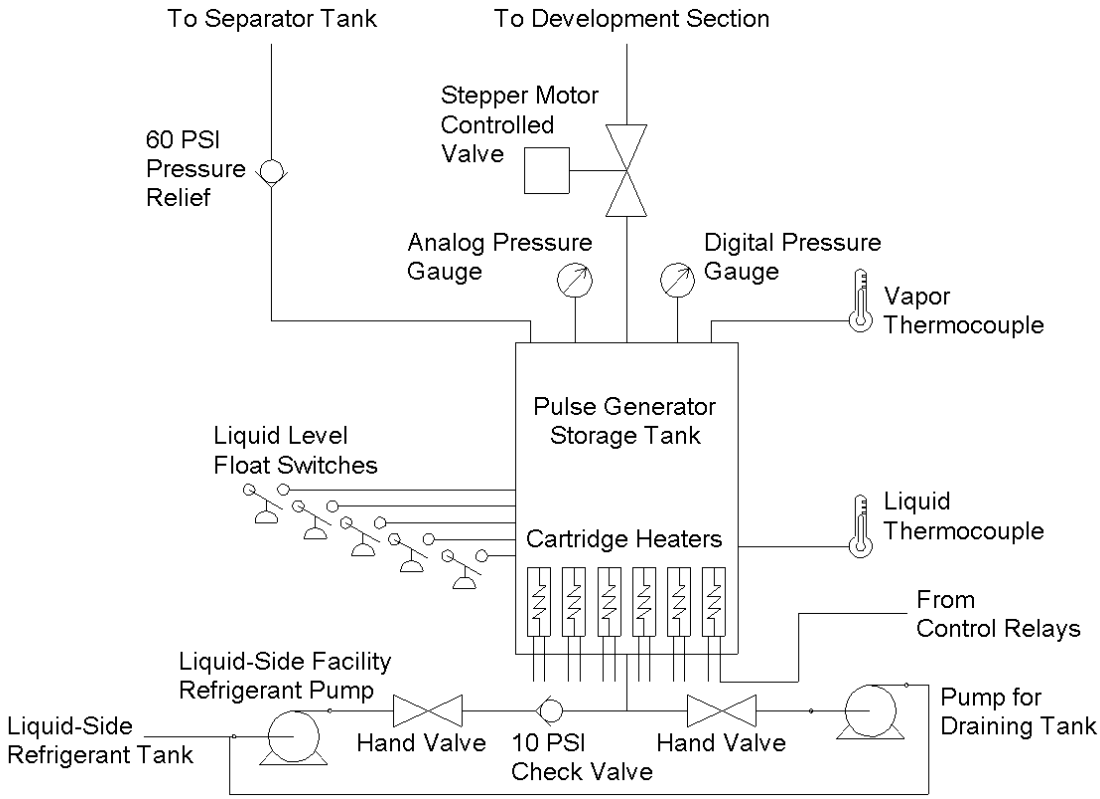

Figure 24: Schematic of the redesigned pulse generator

larger volume was designed to minimize pressure loss and transient effects within the tank during long pulse trains.

Pipe flanges with a 12-hole bolt pattern and a 16-inch outside diameter were cut from 3/8-inch-thick aluminum using a water jet. The flanges were designed with a standard ASME class 150 bolt pattern for a 10-inch Nominal Pipe Size (NPS), except that 0.55-inch bolt holes were used instead of 1-inch due to the low pressure requirements of the vessel. Two additional plates were cut from the same aluminum with the same bolt pattern and outside diameter for use as the top and bottom of the pulse generator. The top plate had one hole cut in the center for the pulse generator outlet and a 5-hole pattern around the center for sensors. The bottom plate had one hole cut in the center for the pulse generator liquid inlet and a 6-hole pattern around the center for the cartridge heater

sleeves. All four flange plates are shown together in Figure 25 and in the exploded view on the right side of Figure 26. The pipe flanges were welded to both sides of the 10-inch pipe, as shown on the right side of Figure 26.

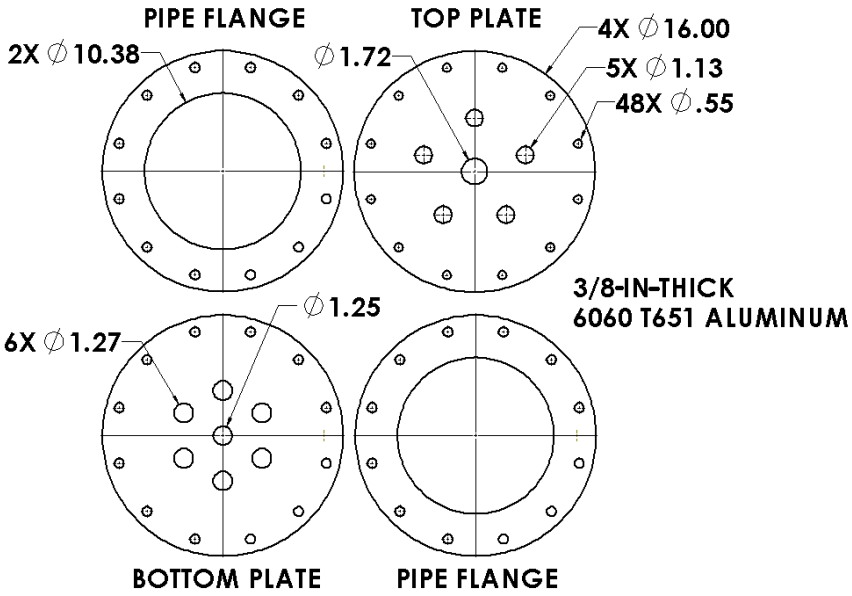

Figure 25: Pulse generator pipe flanges and top and bottom plates

The top and bottom plates were attached to the tank using an R245fa-compatible EPDM O-ring from Zatkoff near the inside edge of the flange and an EPDM gasket around the outer edge. The gasket provided a more even seal, but the exact material composition could not be found, so compatibility with R245fa was not guaranteed. The O-ring provided a compatible seal and the gasket was installed as a backup.

Cartridge Heater Sleeves

Cartridge immersion heaters were chosen for the heating element due to their mechanical simplicity and reliability. Since critical heat flux was a primary design criterion for the old pulse generator, the cartridge heaters were inserted into finned tubes to increase the

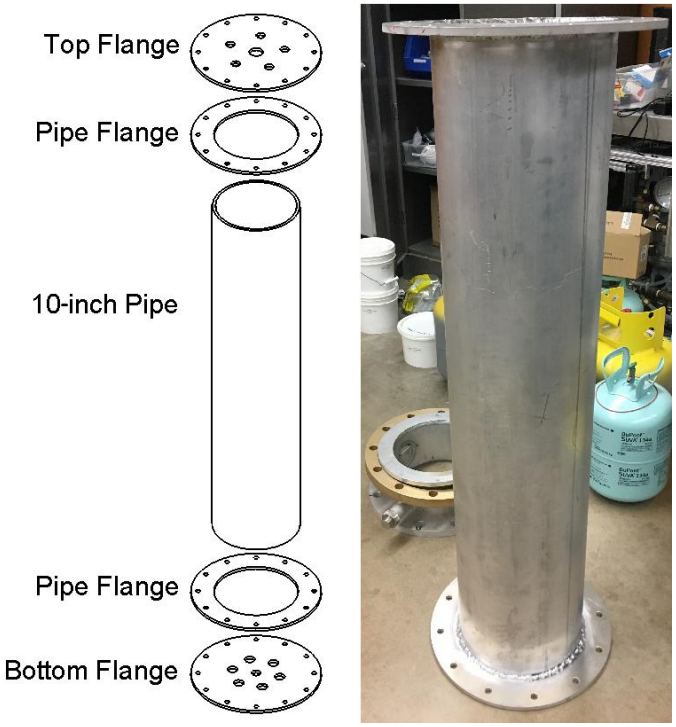

Figure 26: Left: Pulse generator tank components; Right: Flanges welded to 10-inch pipe

boiling surface area. The largest cartridge heater diameter was limited to 0.75 inches. To increase the surface area in contact with the liquid refrigerant, the cartridge heaters were installed in 10-inch-long aluminum tubes with an outside diameter of 1.25 inches. Five fins, 6x0.75x0.125 inches each, were evenly distributed about the center axis and welded to the outside of the sleeves, shown in Figure 27. The surface areas for the bare heater, sleeve tube, and the sleeve with fins are shown in Table 6.

Table 6: Surface area comparison of bare cartridge heater and sleeve geometry

Geometry	Surface Area [in^2]
1000 W Heater	19.4
Cartridge Sleeve	39.5
Sleeve + Fins	89.2

3/8-inch NPT (National Pipe Thread) fittings were welded to the top of each sleeve to allow pressure release during installation of the cartridge heaters as well as sealing after installation. The cartridge heater sleeves were then inserted through the six holes in the bottom plate of the pulse generator and welded to the plate from the bottom side. A standing structure was made with 1x2-inch rectangular aluminum tubes for elevating the bottom plate from the ground (shown in Figure 27). To finalize preparation of the finned sleeves before cartridge heater installation, the inside surface of each sleeve was sanded and cleaned to ensure a tight and smooth fit with each cartridge heater. Each sleeve was then isolated, pressurized to 25 psig, and checked for leaks. After repairing the leaks, Omegatherm "201" thermal paste was added to the surface of the cartridge heaters and the heaters were inserted into the finned sleeves.

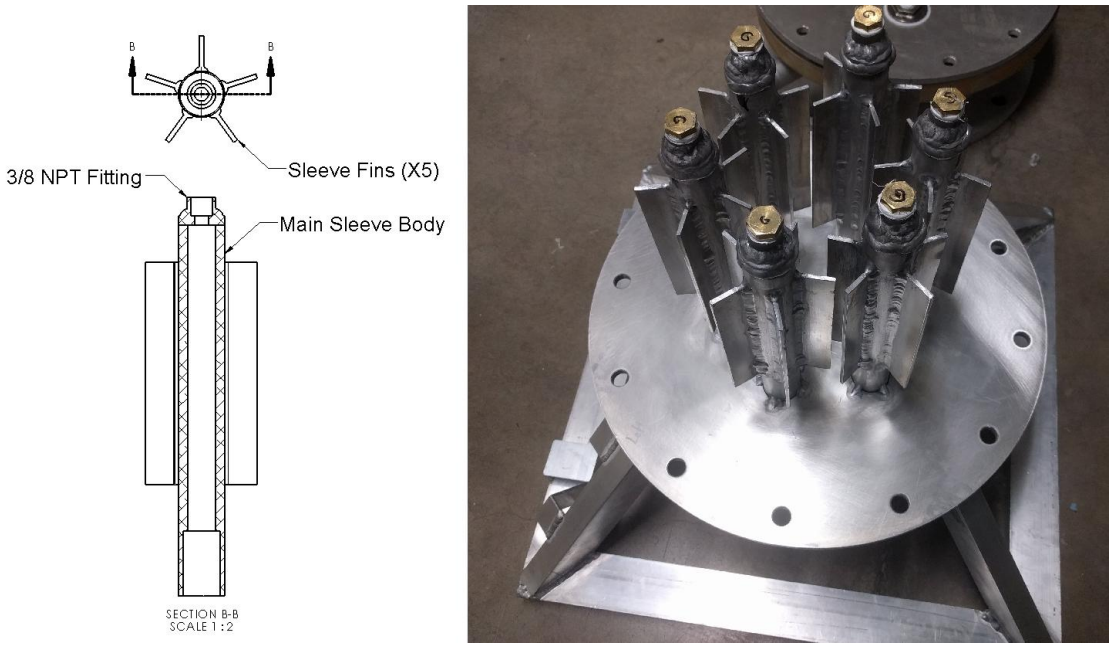

Figure 27: Left: Single cartridge heater sleeve with fins; Right: Cartridge heater sleeves installed on the base plate

Accessory Ports

The six holes in the top plate of the pulse generator and center hole of the bottom plate were designed for bulkhead fittings for attaching sensors and pipe fittings. Five of the stainless steel bulkhead fittings were made by welding a 0.75-inch FNPT (Female National Pipe Thread) x 1-inch MNPT (Male National Pipe Thread) hex bushing to a 2-inch OD x 0.13-inch thick washer. Both sides of the fitting are shown in Figure 28. A sixth fitting of this size was made for the center hole of the bottom plate. The center hole of the top plate required a larger bulkhead fitting, which was made from a 1-inch FNPT x 1.25-inch MNPT hex bushing and a 3.25-inch OD x 0.15-inch thick washer. The bulkhead fittings were originally installed on the pulse generator with hard, white Teflon (PTFE) gaskets for ensured compatibility with R245fa. However, sealing required more force than was anticipated so the gaskets were replaced with compatible EPDM O-rings from Zatkoff.

Figure 28: Left: Top view of stainless steel bulkhead fitting; Right: Bottom view

For the installation of liquid-level float switches and a liquid-temperature thermocouple, six, 0.75-inch holes were drilled in the side of the 10-inch pipe, near the bottom of the tank. Six, 1/2-inch FNPT fittings were aligned with the holes and welded on the

Figure 29: Top plate of pulse generator with bulkhead fittings attached

outside of the tank. Liquid-level float switches were installed in the top five fittings and a thermocouple was later installed in the bottom fitting, shown upside down on the right side of Figure 26. Also shown are conduit channels welded to the tank for clean routing of sensor wires and a guard bolted over the switches to protect bystanders in the case of a switch or fitting failure under pressure.

Pressure Testing

Once all of the components were welded, the pulse generator was fully assembled, and pressure tested with compressed air. The pulse generator was pressurized to 55 psig, disconnected from the air supply, and left for 19 days. In this time, the tank dropped to around 52 psig, losing about 0.158 psig/day. The leakage rate would be far slower during operation at a maximum working pressure of only15 psig. The pulse generator was also pressurized up to 65 psig to test the function of the pressure relief valve (set to 60 psig). The pulse generator, therefore, has a proven operation safety factor of at least 4:1 but

could likely reach pressures greater than 150 psig before failure.

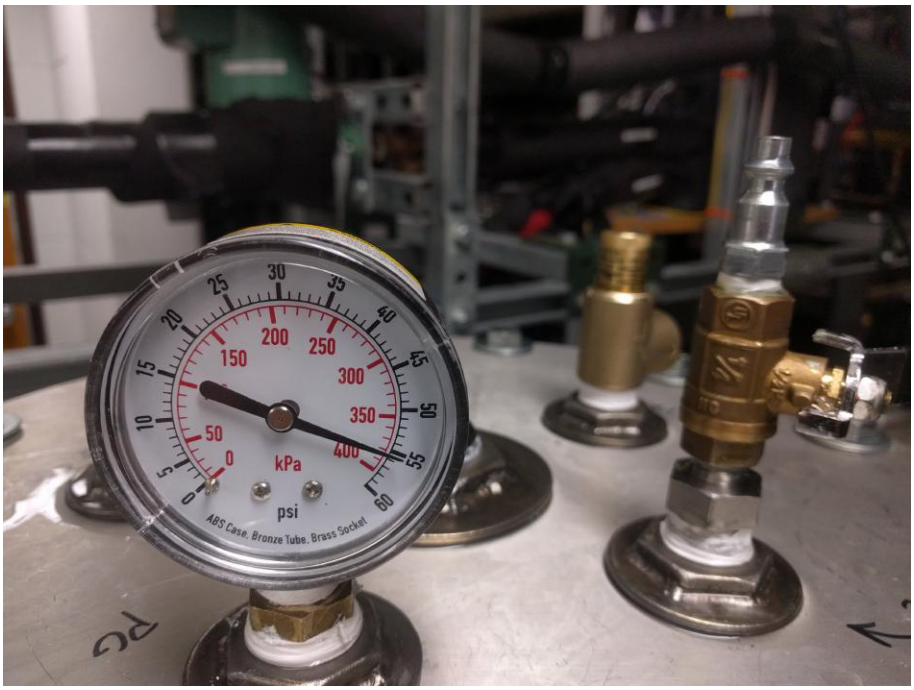

Figure 30: Pulse generator pressurized to 55 PSI gage for leak test

3.0.5 Wiring, Controls, and Instrumentation

The pulse generator was designed for integration with LabVIEW for sensor reading and heater control. Each of the six cartridge immersion heaters was powered by two 120 VAC legs from a three-phase circuit. Each phase was wired in line with a 7A, 250 VAC fuse and connected to a solid-state relay (SSR), shown in the left circuit box in Figure 31. In order to distribute the load current between the three phases, each 120 VAC leg was connected to a single 1000 W cartridge heater and one of the lower power cartridge heaters. The three phase leg to cartridge heater combinations are detailed in Table 7 and the connections are shown in Figure 32. As discussed in the 'Thermodynamic Model' section, the actual voltage available in the lab was 205 V rather than 240 V. For simplicity, this section uses the rated cartridge heater powers and the intended voltage of 240 V.

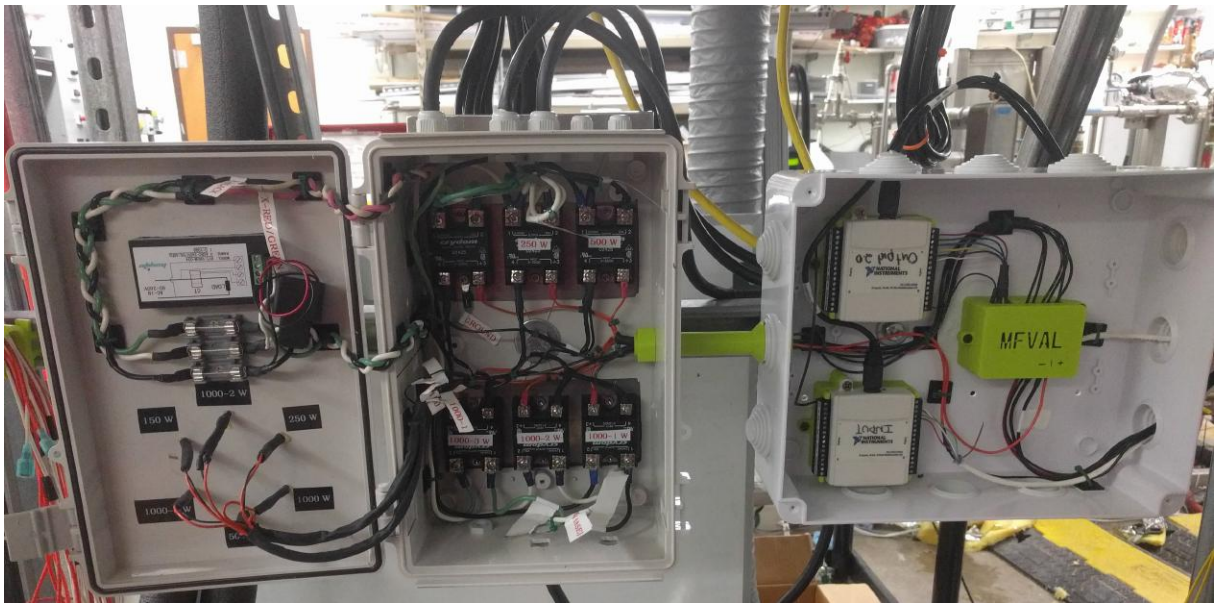

Figure 31: Left: Three-phase power box with fuses, indicator LED's, and six Solid-State Relays; Right: DAQs for interfacing with LabVIEW

Table 7: Cartridge heater phase connections

Phase Label	Primary Connection	Secondary Connection
X	1000 W	150 W
Y	1000 W	250 W
Z	1000 W	500 W

To control the cartridge heaters from LabVIEW, the coil side of each SSR was connected to the output terminals of a DAQ. However, the DAQ unit alone could not output the minimum amperage required (7 mA) to activate the SSRs. A ULN 2803A Darlington array was installed between the DAQ and the SSRs to amplify the signals from the output DAQ, shown by the top circuit diagram in Figure 34. The control signal to each SSR was also connected to a blue LED on the front of the three-phase power box to visually notify the operator which heaters were active. A schematic of the output DAQ heater control circuit is shown at the top of Figure 34. All six heaters and corresponding LEDs are shown activated with the control circuit and pulse generator in Figure 33.

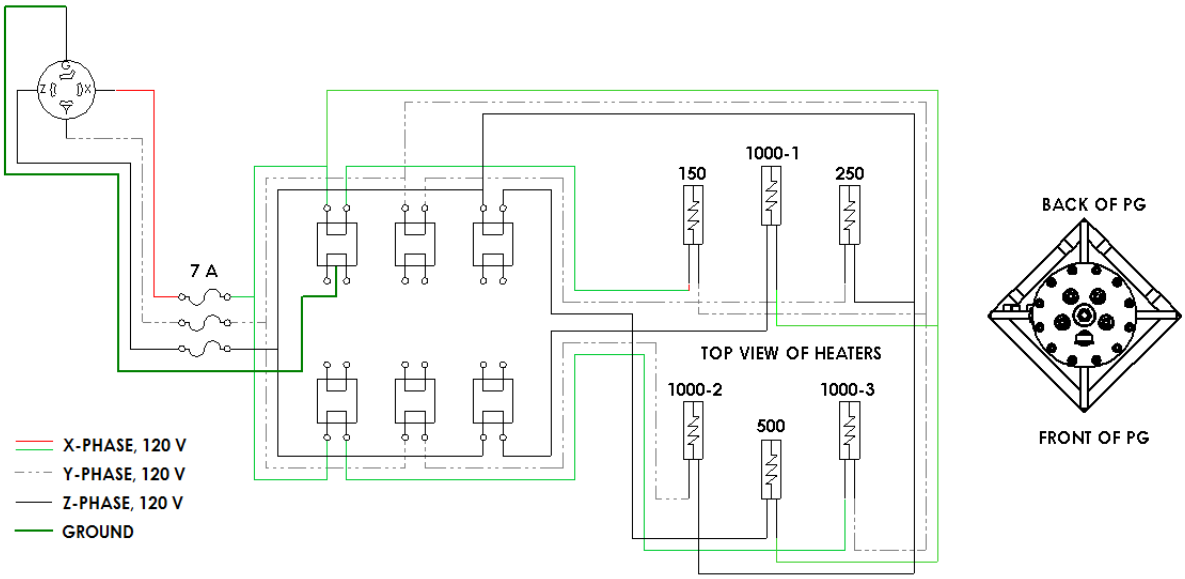

Figure 32: Pulse generator heater power circuit with 3-phase 240 V source shown in the upper left and the heaters middle-right

Figure 33: All six cartridge heaters and respective blue LEDs activated

Several sensors were added to the pulse generator for general operation and data collection. An absolute pressure sensor (Omegadyne model # PX209-0605A) and thermocouple were installed in the top of the pulse generator for recording the pressure and temperature of the refrigerant vapor. Five polypropylene liquid-level float switches (Grainger model # 5DYC2) and a thermocouple were installed in the side of the tank, near the bottom, for monitoring the liquid refrigerant level and temperature. Each float switch was connected to an LED mounted on the pulse generator and to a digital input of a DAQ unit. This circuit is shown in the bottom of Figure 34.

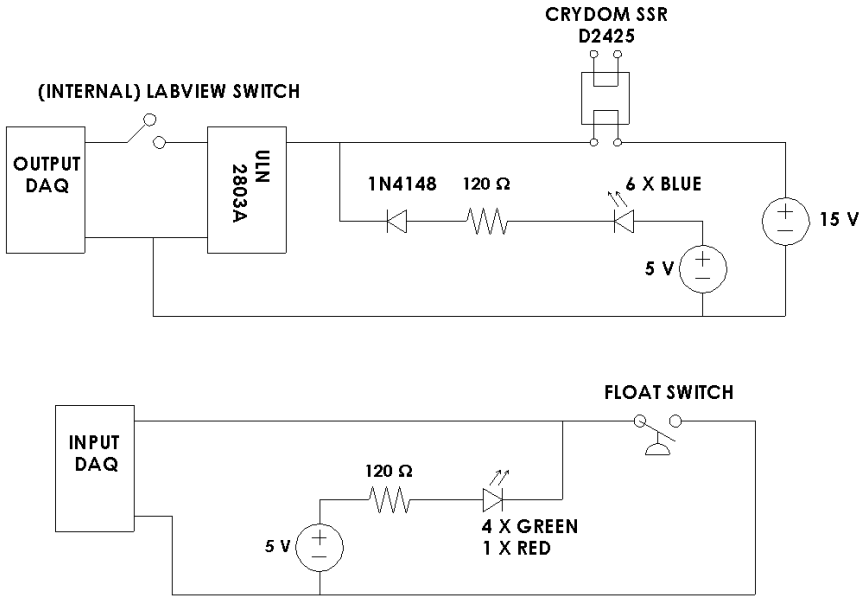

Figure 34: Pulse generator heater control circuit (top) and float switch liquid level sensor circuit (bottom)

Stepper Motor Controlled Valve

Although the old pulse generator lacked frequency control above 1 Hz, the new pulse generator used the same stepper motor and valve. The stepper motor was previously supplied with a voltage too low for higher frequency operation. To allow the new pulse generator to reach pulsing frequencies up to 10 Hz, a high voltage power supply was connected to the stepper motor and a ramping function was programmed into LabVIEW.

3.0.6 Safety Features

The new pulse generator was designed with inherent, computer-automated, and manual safety features. The 16.4-gallon storage tank used for the new pulse generator takes much longer to pressurize than the old 3.2-gallon tank. This allows more time for the operator to react and prevents excessive pressure build up in the tank. The size of the tank also provides room for more liquid storage. The large capacity of liquid takes longer to boil before exposing the heaters in the bottom of the tank. This again provides more time for the user to react before an emergency situation can occur.

Despite these inherent features, several automatic safety features were also added to protect the user and equipment. The greatest threat to safety and equipment involve the cartridge heaters operating too long and building up excessive pressure in the tank or operating without liquid to cool them. LabVIEW was programmed to shut down the heaters if either the pressure sensor reads a value above a set point (typically 15 psig) or the lowest liquid-level switch is activated. To prevent catastrophic failure in the event that all other safety features fail, a pressure relief valve was added to the top of the pulse generator, shown in Figure 35. The valve was set to relieve pressure above 60 psig, which is significantly lower than the pressure rating of the weakest components (the float switches are rated for 150 psig). The pulse generator was leak tested for two weeks at 55 psig and also pressurized to 65 psig to test the pressure relief valve.

In addition to the automatic safety features, manual on/off switches were added for the power box, the control box, and for the heaters in the LabVIEW program. Each of the float switches and cartridge heater SSRs was connected to an LED to keep the operator informed about the level of the liquid refrigerant and heater power. An analog pressure gauge was added to the top of the pulse generator for offline observation of the

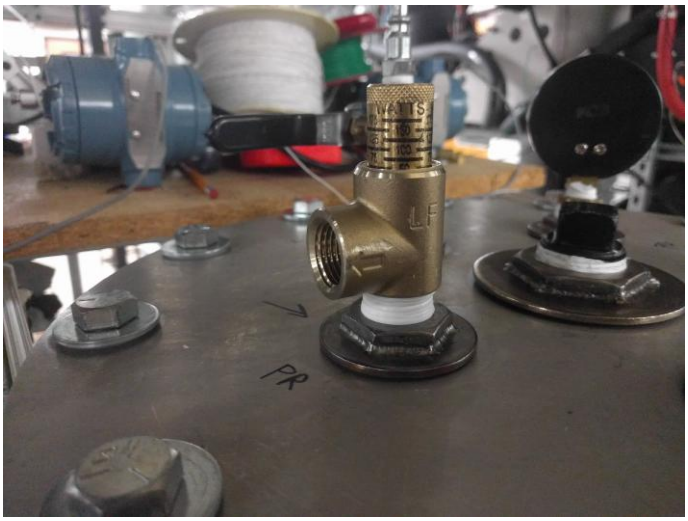

Figure 35: Pressure relief, set to 60 PSI

internal pressure.

4 Measurement Methods and Results

4.1 Annular Flow Liquid Film Thickness Measurements

Measuring the liquid film thickness of two-phase annular flow is useful for calculating wall shear as well as monitoring for film thinning or dryout conditions. Wall shear calculations can be compared to two-phase flow correlations and estimates of the heat transfer coefficient of the flow. Real-time film thickness measurements can provide qualitative insight on the effect of flow parameters such as liquid flow rate, pulsing frequency and amplitude, and input heat flux at the wall. The film thickness measurement setup is shown in Figure 36.

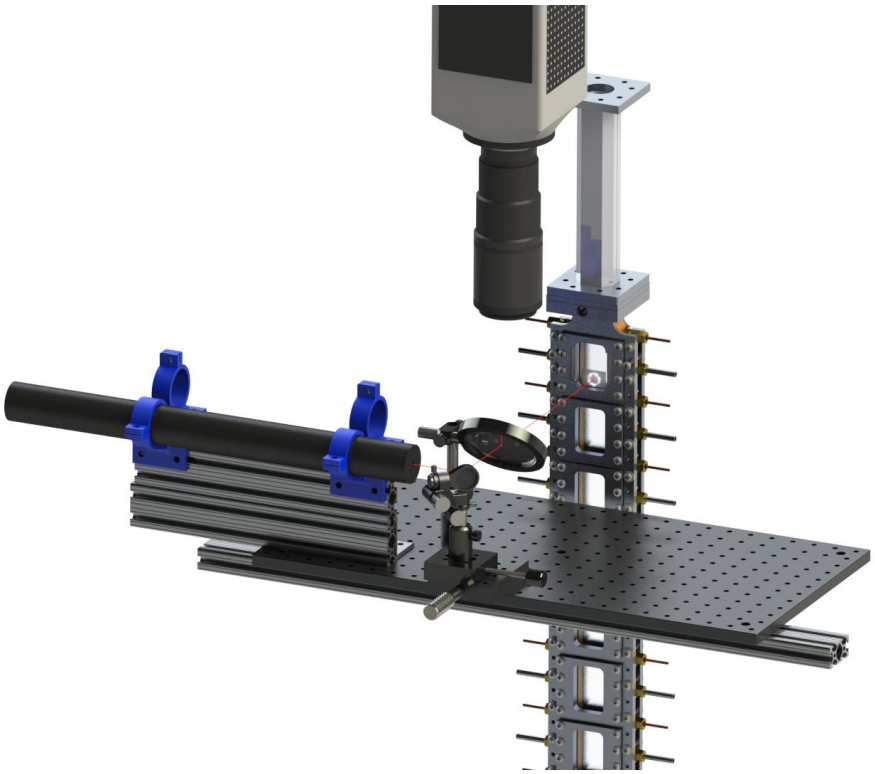

Figure 36: Rendering of the liquid film thickness measurement optical setup with test section

Background

Several non-invasive techniques have been used to measure the liquid film thickness in two-phase flows. For a conductive working fluid, conductance or capacitance probes have been used to estimate the liquid film thickness [30], [33]. Rodriguez [5] and Schubring et al. [29] used planar laser-induced fluorescence (PLIF) to optically analyze the film thickness in air-water annular flows. Both techniques were able to capture the film thickness with good time and spatial resolution.

Working with a non-conductive and chemically volatile liquid such as R245fa requires a method that is independent of electrical conductivity and preferably does not require additives. The method also needed to be noninvasive due to the scale of the thin liquid

film that is formed, typically less than 150 µm thick. A noninvasive, optical technique presented by Hurlburt and Newell [7] fulfills these requirements and was implemented at the MFVAL and used by both Vanden Hogen [4] and Rodarte [3]. The technique is used in the current experiment to successfully measure the liquid film thickness of a vertical annular two-phase flow of R245fa.

4.1.1 Optical Theory

The film thickness optical technique presented by Hurlburt and Newell [7] uses light reflected off of the liquid-vapor interface at the critical angle to form a measurable ring of light on the outer surface of the transparent wall. The critical angle, and therefore the size of the light ring, changes with the thickness of the liquid film. By capturing images of the light ring and measuring the ring size compared to the size of a dry ring, the film thickness can be measured with a time resolution limited mostly by the frame rate of the camera and a spatial resolution limited by the quality of the optics.

Total Internal Reflection

The optical technique relies on the total internal reflection of light at the liquid-vapor interface. Light rays which contact the interface at and above the critical angle (Equation 3) are reflected. The technique works because the index of refraction of the vapor core (n_2) is lower than the index of refraction of the liquid film (n_1).

$$\theta_{\text{critical}} = \arcsin(\frac{n_1}{n_2}) \tag{3}$$

Light Reflectance Model

To ensure light rays reach the liquid-vapor interface at the critical angle, a light point source is diffused on the outer surface of a glass window. The diffused light rays are projected in the glass at angles between -90°and 90°from incidence. The light rays then pass into the liquid film and vapor core at angles of incidence dictated by Snell's Law (Equation 4) and the refractive indices of the materials.

$$n_i \sin(\theta_i) = n_t \sin(\theta_t) \tag{4}$$

Light rays which reach the liquid-vapor interface at angles of incidence less than the critical angle (Equation 3) are refracted and lost into the vapor core. Light rays which hit the interface at and slightly above the critical angle are reflected back to the outer surface of the glass. These rays form the inner radius of the light ring observed on the outside of the glass window, as shown in Figure 37. The remaining diffused light is reflected at the glass-liquid interface back to the outer glass surface at a more dispersed concentration.

Rearranged from Hurlburt and Newell [7], Equation 5 can be used to calculate the liquid film thickness (h_l) by calculating the critical angle at the liquid-vapor interface ($\theta_{\text{crit-lv}}$) and measuring the radius of the light ring with a liquid film (r). The last parameter required is the radius of the light ring in the absence of a liquid flow (r_o), which can be found by measuring the light ring formed with only the glass window and

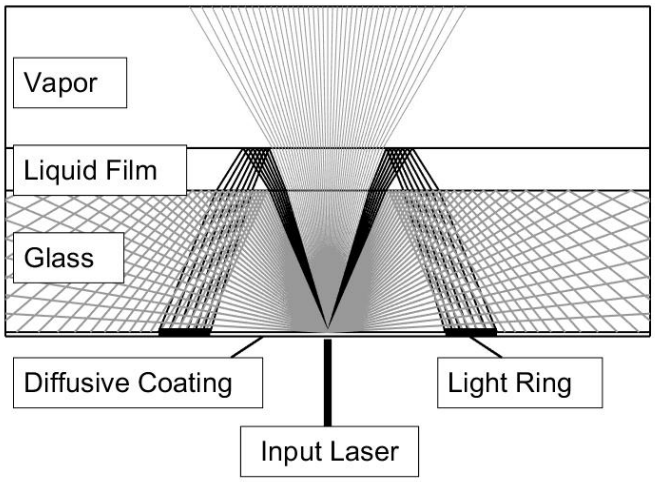

Figure 37: Ray trace of light ring formation

vapor (Equation 6).

$$h_l = \frac{\frac{1}{2}(r - r_o)}{\tan(\theta_{\text{crit-lv}})} \tag{5}$$

$$r_o = 2h_{\text{wall}}\tan(\theta_{\text{crit-gv}}) \tag{6}$$

4.1.2 Experimental Setup

The film thickness optical setup consists of a light source and a means of capturing images of the film thickness light ring. The most complicated feature of the setup is the method used to capture images along the same axis as the input light source. A hole, about 1/8 inches in diameter, was drilled through a mirror at a 45° angle to allow a 0.8 mm (0.031-inch) diameter laser beam through while also reflecting the image of the light ring

to a camera.

A Uniphase 1135P 15 mW HeNe laser provides the point light source for the film thickness measurements. The laser is reflected 90° by a high-precision rotating mirror on two fine-adjustment stages, shown in Figure 38. The laser beam passes through the 45° hole in the camera mirror and continues to the test section window. White freezer tape is used to diffuse the laser beam on the outer surface of the glass test section window. A Phantom V311 high-speed camera is mounted vertically and directed at the camera mirror. The mirror, camera, and camera lenses are adjusted until the light ring is in focus for image capture.

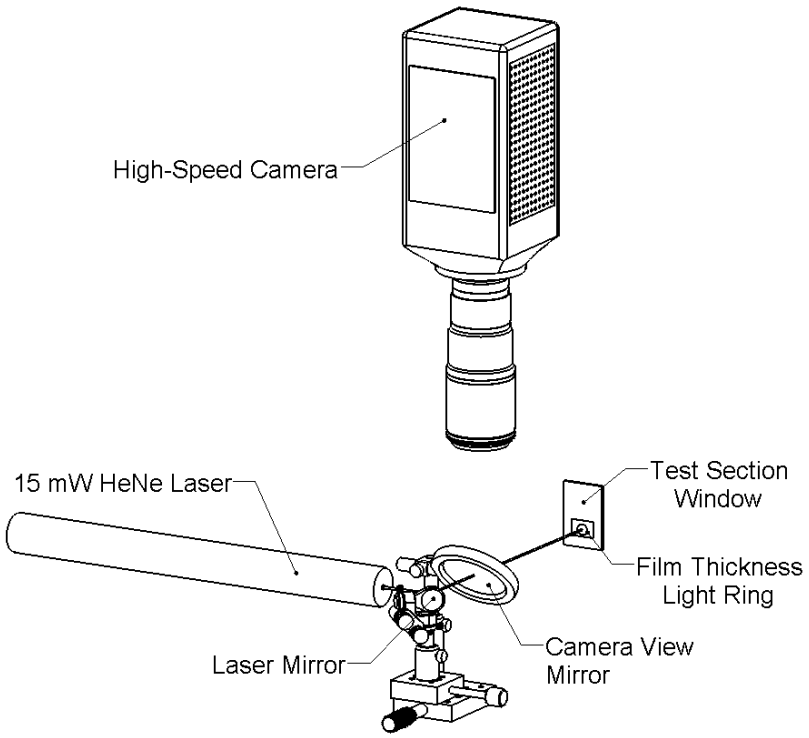

Figure 38: Film thickness optical setup

4.1.3 Calibration

The measured light ring radius with a liquid flow (R) must be calibrated to a known reference scale and requires the dry light ring radius (R_o) in order to calculate the film thickness.

Pixel Calibration

After the camera and film thickness optics are in position, the camera image is calibrated using grid paper. A single image is taken with the grid paper placed on the surface of the diffusive layer on the test section window. The image is imported into a MATLAB image processing code to find the number of pixels between the two corners of a large square on the grid paper (shown with red circles in Figure 39). This known distance (12700 µm) is used to calculate the size of a single pixel in the image.

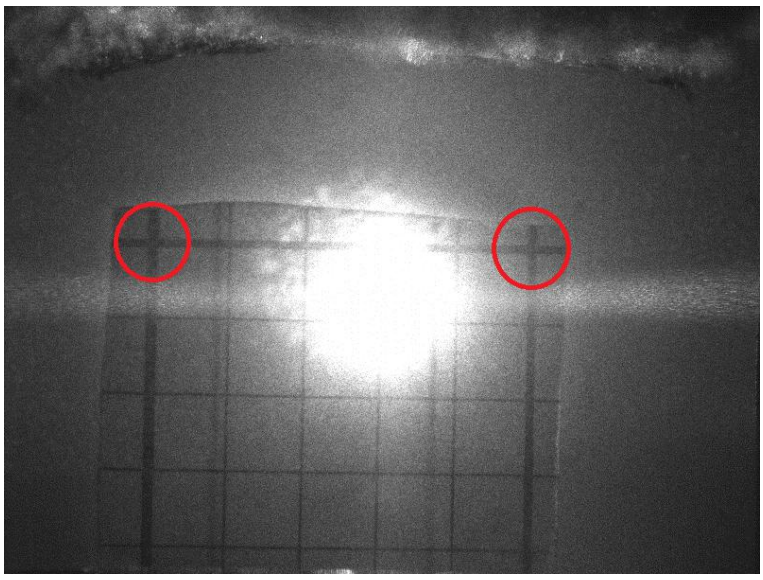

Figure 39: Pixel calibration using grid paper

Dry Calibration

Measurement of the dry light ring radius (R_o) is completed by taking images of the light ring with no liquid flow and analyzing the images using MATLAB. Typically, 500-1000 images are taken with a resolution of 800x600 pixels and a frequency of 250 frames per second. A single, cropped image of the dry light ring is shown in Figure 40 (left) with the corresponding measurement of the ring radius (right), after analysis using MATLAB. The measured radius is then converted to a length in micrometers using the pixel size from the pixel calibration.

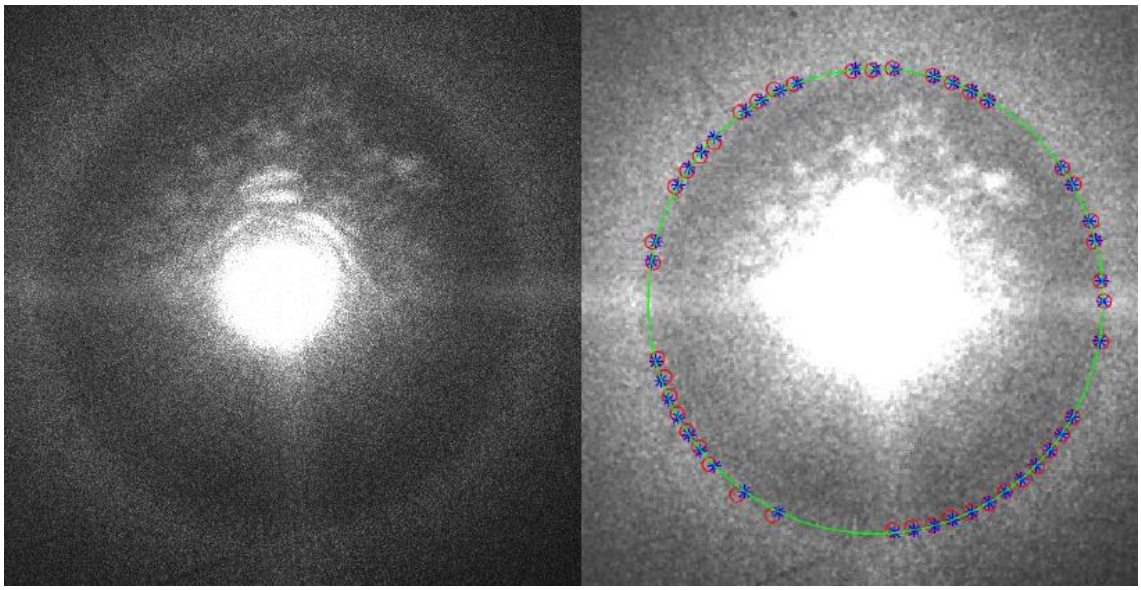

Figure 40: Left: Raw image of dry light ring; Right: MATLAB radius measurement

4.1.4 Data Processing

Film thickness measurements are completed using the same method as the dry calibration. Images of the light ring with a liquid film are taken and analyzed using a similar program in MATLAB. A cropped image of the film thickness light ring is shown on the left of

Figure 41 with the corresponding radius location estimate using MATLAB on the right. The measured radius of the light ring with liquid flow (R) and without (R_o) are used with the pixel size calibration to calculate the liquid film thickness for each image taken.

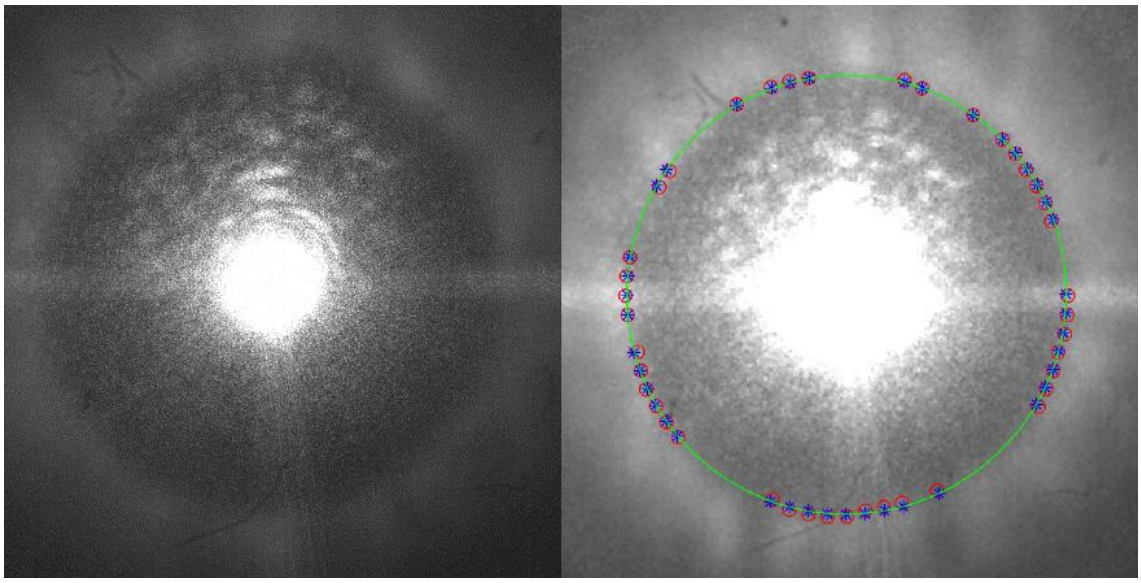

Figure 41: Left: Raw image of film thickness light ring; Right: MATLAB radius measurement

Previously, a maximum of 2000 images were captured because the MATLAB program could only analyze multipage TIFF (a standard image file format) files [4]. The original program was modified to accept individual TIFF files, allowing the analysis of as many files as desired, up to the maximum number of files that could be stored by the camera memory. At the previously captured resolution of 1280x800, the Phantom V311 could store 5000 images. This resolution was found to be unnecessary because the MATLAB analysis program crops the image to roughly the size of the light ring (slightly bigger than the image on the right side of Figure 41) before measuring the light ring radius. A more appropriate resolution of 800x600 pixels was therefore chosen instead. At this resolution, the Phantom V311 memory can store up to 10000 images, at up to approximately 6000 frames per second. Data collected at 6000 frames per second is shown in Figure 44. To

maintain data quality but save time when saving files, typically only 5000 images are taken per data set with a resolution of 800x600 pixels and a sample frequency of 250 frames per second.

4.1.5 Results and Analysis

Following image analysis, the film thickness measurements are then stored in a single-column array, with each value corresponding to a single data image. These measurements are used for further flow calculations or data reduction. The film thickness data versus time for six different steady state vapor mass flow rates is shown in Figure 42. The liquid mass flow rate was set to 10 [g/s] for all of the runs. The liquid film thickness becomes steadier at higher vapor flow rates and the average film thickness decreases.

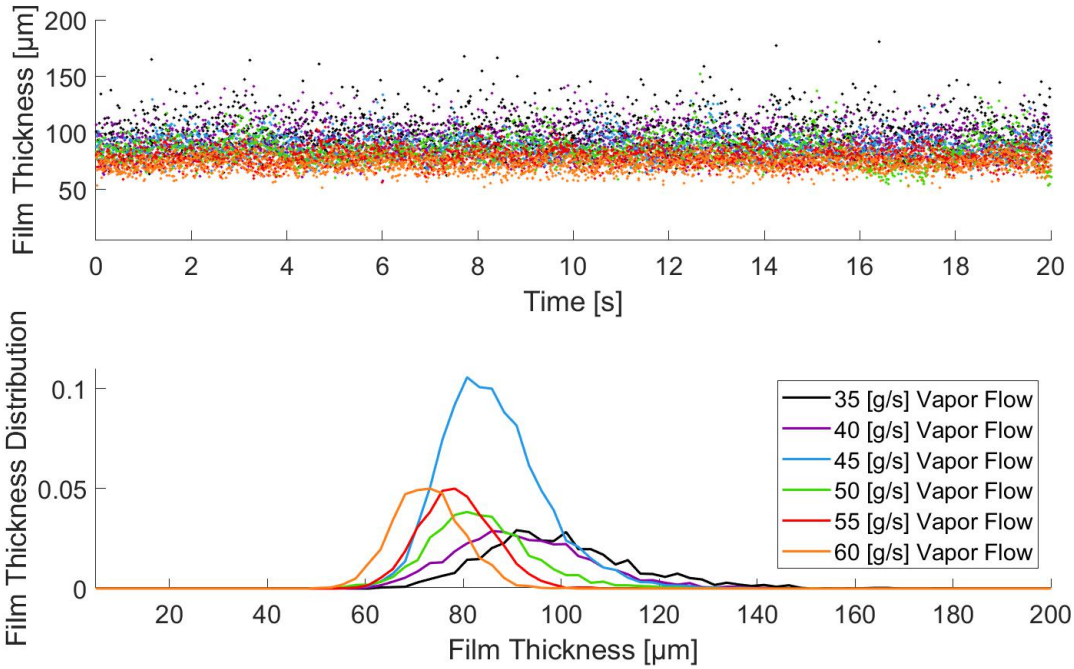

Figure 42: Film thickness for six steady state vapor flow rates

The film thickness data versus time (top) for 1 Hz pulsed data is shown in Figure

43 along with the film thickness frequency distribution (bottom left) and a Fast Fourier Transform (FFT) (bottom right). The 1 Hz pulsing frequency can be seen clearly in both the film thickness data and the FFT. The windows were heated with 15 W of electrical power and the images were captured at 250 frames per second.

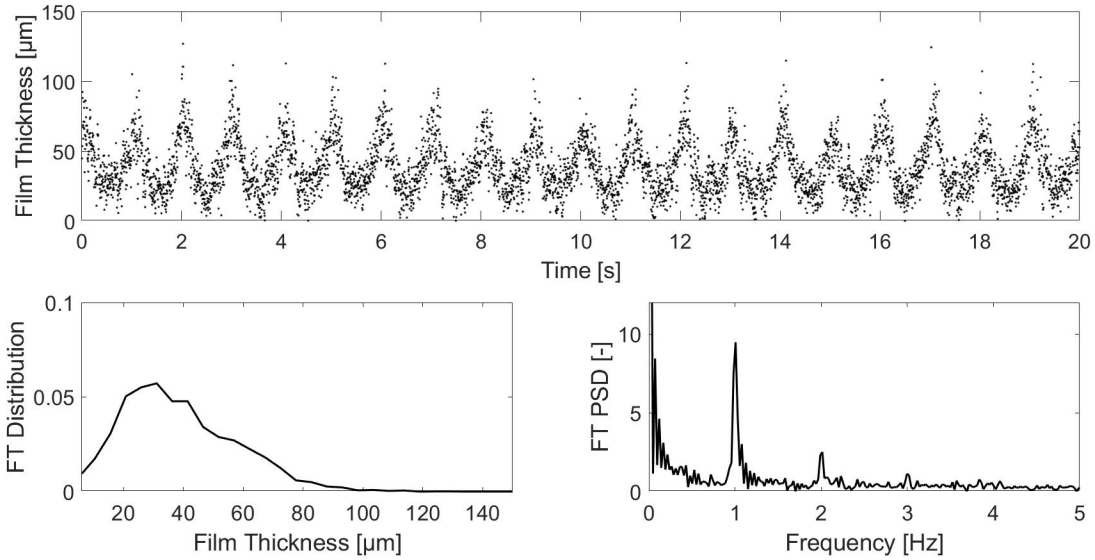

Figure 43: Film thickness with 1Hz pulses, 15W heated data

Film thickness measurements were taken at 6000 frames per second to test the high-speed capability of the technique. This was not previously feasible using the code which could not analyze individual TIFF files and while recording 1280x800 pixels per image. Data collected at 6000 frames per second for roughly 1.6 seconds (10000 images) and 0 Hz (steady) data is shown in Figure 44 along with the film thickness distribution (FT Distribution).

Error Analysis

The film thickness measurement technique is limited in accuracy by several properties of the flow, image recording, and analysis.

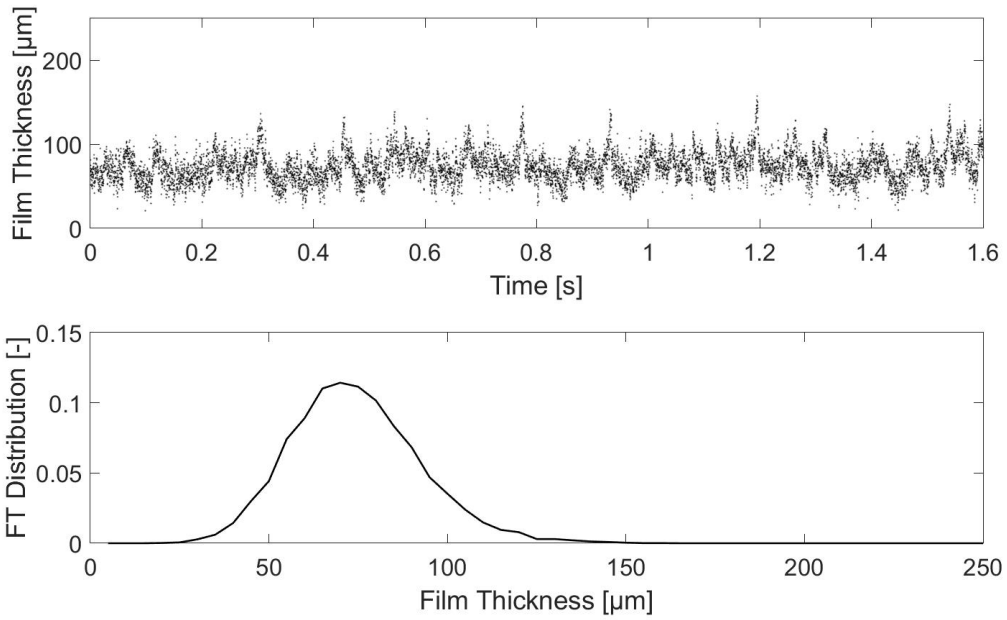

Figure 44: Film thickness data, 0 Hz (steady), 6000 fps

Changes in the index of refraction of the working fluid with temperature can cause fluctuations in the size of the light ring that are independent of changes in the film thickness. Reflection of the light which forms the light ring is dependent on the critical angle (Equation 3), which depends on the indices of refraction of the liquid and vapor. However, changes in the light ring diameter due to this effect are small when the liquid film is very thin. Measuring a film thickness of 150 µm over a range of 20-35 °C with a R245fa working fluid, the light ring diameter should change roughly 5.1 µm. This corresponds to a film thickness measurement error of 1.9 µm, or 1.3 %.

The direction of the reflected light and the range over which light is reflected at the liquid-vapor boundary can also introduce small measurement errors. The surface waviness of the liquid film in contact with the vapor boundary can change the orientation of the reflecting interface, causing changes to the light ring. This effect also gives the film thickness light ring its wavy appearance compared to the dry light ring (Figure 41

compared to Figure 40). Light is also not exclusively reflected at the critical angle. As shown by the ray trace in Figure 37, light is reflected at the liquid-vapor interface over a small range of angles after reaching critical angle at the glass-liquid interface. This results in a blurry inside edge of the light ring and decreases the precision of the image analysis.

Deviations inherent in the film thickness measurements can be seen in the dry light ring measurements used for calibrating the film thickness light ring. The dry ring film thickness depends only on static geometry and should therefore remain constant for all captured images. The dry ring film thickness measurements are shown in Figure 45 along with a reference line at zero and lines at two standard deviations above and below zero, or +/- 10 µm.

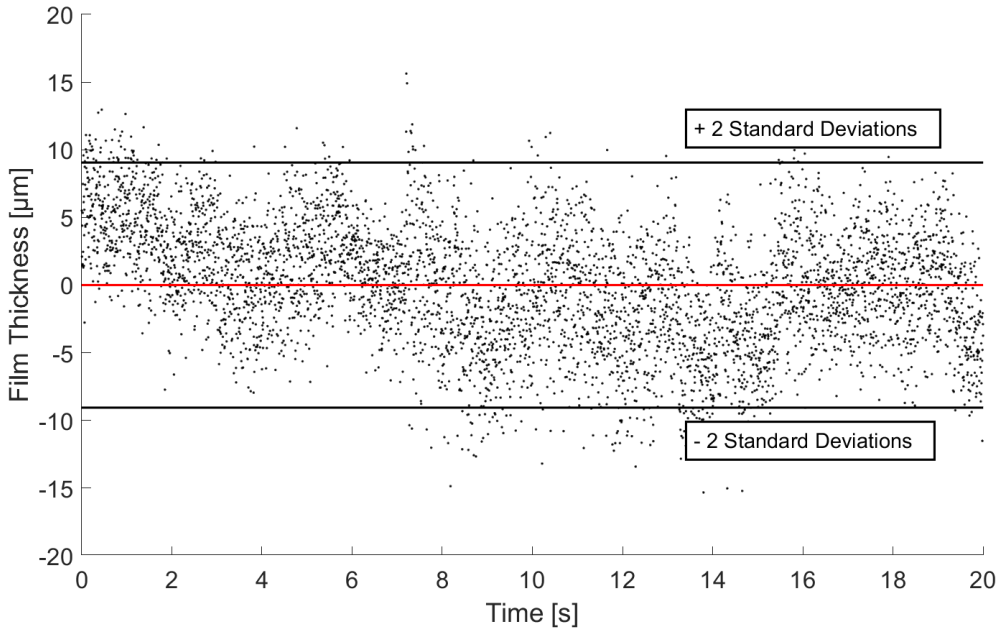

Figure 45: Film thickness dry calibration measurements

4.2 Wall Temperature Measurements

Measuring the temperature of the working fluid at the wall of the flow is necessary to calculate the heat transfer coefficient of two-phase annular flow. The temperature on the outside surface of the test section window is measured using a thermocouple and the saturation temperature of the flow is calculated by measuring the pressure in the test section. A controlled heat flux is added to the inside wall of the test section through the FTO coating. The wall and saturation temperatures and the known heat flux can then be used to calculate the heat transfer (and heat transfer coefficient) between the wall and the flow. The temperature of the outer surface is required to help correct the heat flux under transient conditions.

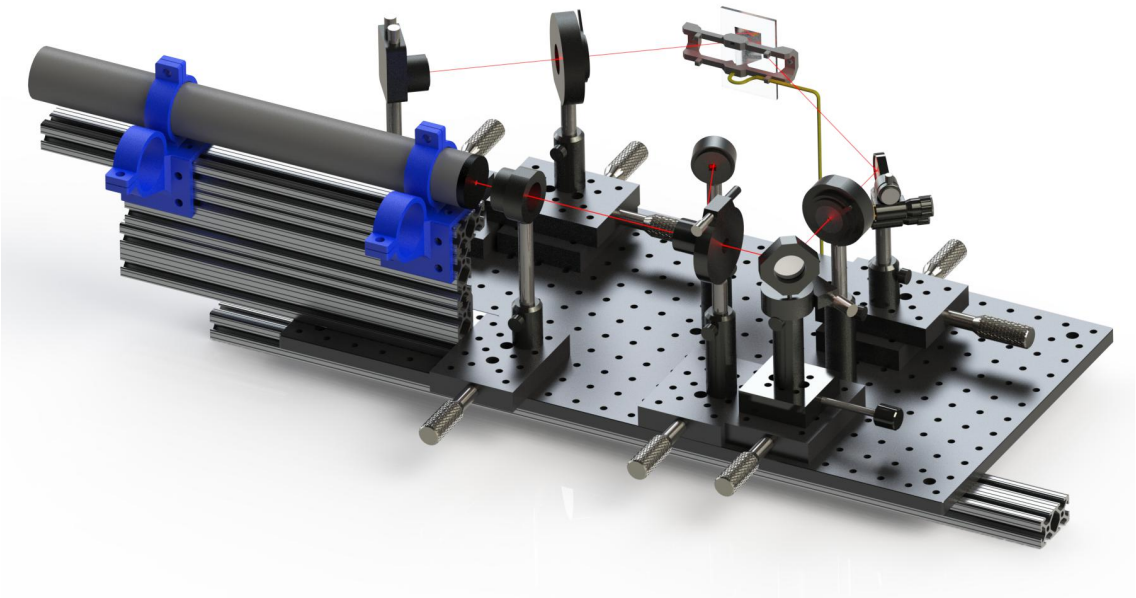

Figure 46: CAD rendering of the wall temperature measurement optical setup

4.2.1 Background

A range of techniques have been used to measure the temperature at or near the wall interface with a liquid. Fast-response thermocouple probes have been used to measure the temperature near the internal test section wall with good time resolution (16,000 Hz) [31]. However, thermocouples or other physical devices cannot be used to measure the temperature of a two-phase annular flow without disturbing the fragile liquid film, typically less than 150 µm thick in the present study.

Infrared thermometry has also been used to measure the temperature near the liquid-wall interface [22], [23]. This method has the advantage of being noninvasive (as an optical technique) and can be used to collect a field of temperatures. However, infrared thermometry requires an expensive setup and, like physical probes, cannot obtain the temperature at the liquid-wall interface.

The use of reflected light to measure temperature (termed thermoreflectance) has the benefit of reaching the liquid-wall interface while also being noninvasive to the flow. This method can be used side-by-side with other optical methods already utilizing a transparent test section wall. Thermoreflectance has been used to measure the surface temperature of solids [14], [20]. Qiu et al. [14] measured the change in temperature of pure, single-crystalline silicon using changes in surface reflectivity.

The change in reflectivity for a given temperature is greater and therefore easier to measure in a liquid. Shedd and Anderson [21] demonstrated a thermoreflectance technique for making optical and nonintrusive measurements of the temperature at the interface between a liquid and solid. Diffused light rays were reflected off of a glass-liquid interface back to the outer surface of the glass wall where they formed a measurable ring of light. The diameter of the light ring was dependent on the critical angle of incident

light at the glass-liquid interface. The critical angle was a function of the liquid index of refraction, which depended on the temperature of the liquid at the interface. The accuracy and time resolution for this method is largely dependent on the resolution and sampling frequency of the high-speed camera used.

Longtin and Fan [18], [19] were able to measure the instantaneous temperature at a liquid-solid interface using thermoreflectance. A 632.8 nm laser probe beam was reflected off of a liquid-solid interface and subsequently absorbed by a silicon photodiode. The light intensity reflected at the liquid-solid interface was dependent on the temperature-dependent refractive index of the liquid. The output voltage from the photodiode was calibrated to a known temperature before data collection and then subsequently used to measure the change in temperature at the liquid surface with good time and spatial resolution. Chen et al. [6] measured the temperature at the surface between glass and an impinging liquid droplet using a similar method as Longtin and Fan.

In the current experiment, a laser-based thermoreflectance technique was used to measure the instantaneous temperature at the wall of a two-phase annular flow. The technique was able to measure the temperature at the liquid-wall surface with a resolution greater than 0.1 °C at 2000 samples per second, without disturbing the thin liquid film. The setup was relatively inexpensive and did not interfere with the optical liquid film thickness measurements taken on the same transparent test section.

4.2.2 Optical Theory

The wall temperature measurement technique is used to calculate the instantaneous temperature at a liquid-solid interface based on the intensity of light reflected at the interface. The refractive index of the liquid changes with temperature and subsequently

changes the amount of light reflected at the interface. By measuring the intensity of reflected light, the refractive index of the liquid, and therefore temperature, can be calculated.

Temperature Dependence of the Refractive Index

The optical technique relies on the temperature dependence of the refractive index of the working fluid. Figure 47 shows the variation of the refractive index with temperature for liquid water (for reference) and liquid R245fa. The partial derivative of the refractive index of water with respect to temperature is approximately 2×10^{-3} $\frac{1}{^\circ\mathrm{C}}$ over the temperature range of interest (15-35°C) while liquid R245fa has a sensitivity of 1.1×10^{-2} $\frac{1}{^\circ\mathrm{C}}$ over the same range [2].

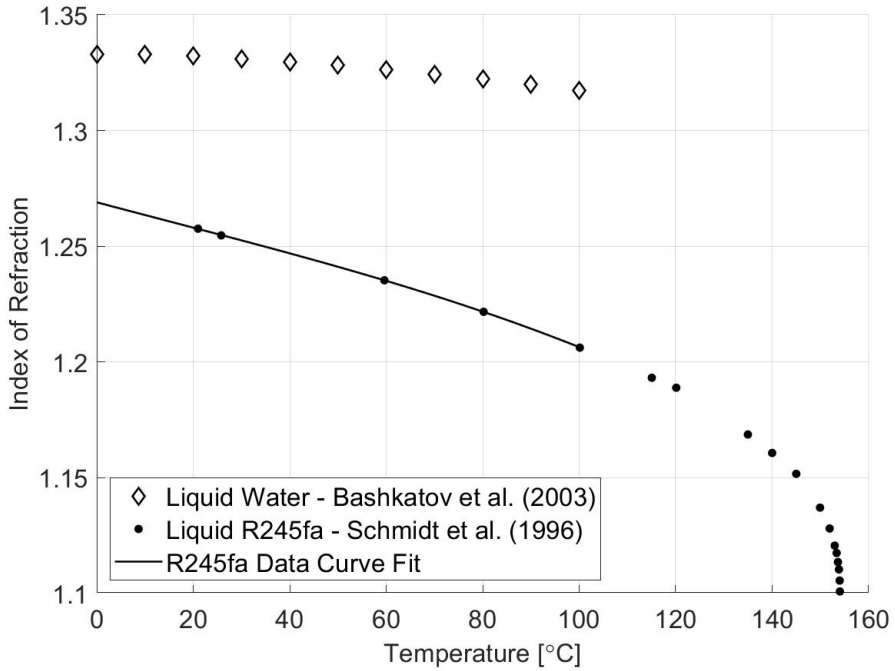

Figure 47: Refractive index of liquid water and liquid R245fa as a function of temperature, with curve fit for R245fa data, [13], [2]

The sensitivity of the index of refraction of the BK7 glass used by the optical tech-

nique is roughly 6×10^{-5} $\frac{1}{^\circ\mathrm{C}}$ over this temperature range [11]. The refractive index of glass and the other optical materials is assumed to be constant across the tested temperature range, with the exception of R245fa (liquid and vapor) and polyolester oil (POE).

Model for Simplified Interface

The indices of refraction of liquid R245fa and the wall material, as well as the angle of incidence of light hitting the interface, determine the intensity of light reflected at the interface. Therefore, the change in reflected light intensity can be measured and used to calculate the change in the index of refraction of R245fa, which in turn can be used to find the temperature of the liquid at the wall.

To construct the reflected light intensity model, a light ray is traced through the optical materials. Starting with a controlled input angle of incidence (θ_i) of the light beam at an optical interface, the angle of transmittance (θ_t) can be found using Snell's Law (Equation 7) if the index of refraction of the first (n_i) and second (n_t) material are known.

$$n_i sin(\theta_i) = n_t sin(\theta_t) \tag{7}$$

Using Equation 7, light beams were traced through a simplified optical geometry, containing only a glass wall followed by liquid and vapor R245fa (Figure 48). The input angle of incidence was varied from 55.05-56 degrees (just before the critical angle) and the indices of refraction of liquid and vapor R245fa were interpolated over a 0-50°C temperature range using data from [2] (Figure 47). The index of refraction of glass was assumed constant (1.515) over this temperature range. Only p-polarized light was used

(Equation 8) with a wavelength of 632.8 nm.

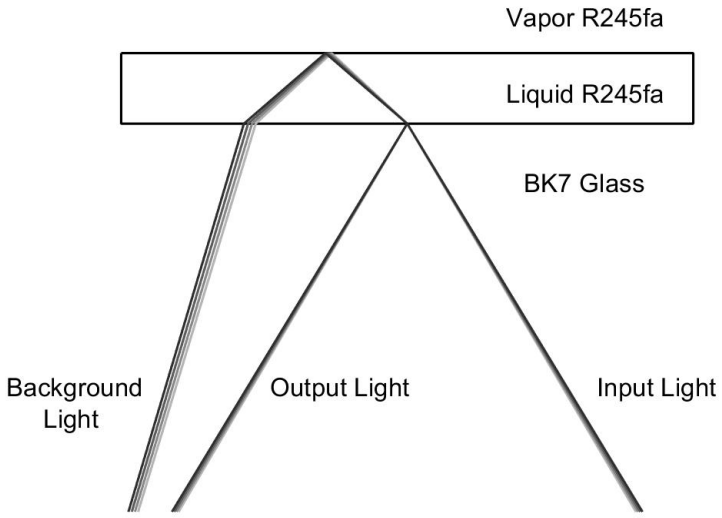

Figure 48: Trace of rays reflected off of a glass and liquid R245fa interface over a 1.5 degree range of angles just before the critical angle, shown as lines getting darker for increasing angle, material thickness not to scale

The input light beam reflects at the glass-liquid interface (the reflection of interest) as well as the liquid-vapor interface after some light is transmitted through the liquid R245fa. Both reflections exit the optics with similar trajectories. Reflections from the liquid-vapor interface are termed background reflections when discussing the simplified model as well as the more detailed model of the actual optical geometry.

After tracing the path of the light beam, the amount of light reflected at each interface can be calculated as the Fresnel coefficients, shown as Equations 8 and 9 for p-polarized and s-polarized light, respectively. The reflected light intensity for each interface is dependent on the indices of refraction, the angles of input and transmittance,

and the light polarization.

$$R_p = \left[\frac{(n_t\cos(\theta_t) - n_i\cos(\theta_i)}{(n_t\cos(\theta_t) + n_i\cos(\theta_i)}\right]^2 \tag{8}$$

$$R_s = \left[\frac{(n_t\cos(\theta_i) - n_i\cos(\theta_t)}{(n_t\cos(\theta_i) + n_i\cos(\theta_t)}\right]^2 \tag{9}$$

The intensity of light reflected at the glass-liquid and liquid-vapor interfaces are shown in Figure 49 over the same temperature range and angles used in Figure 48. The change in intensity of light reflected at the glass-liquid interface for a given change in temperature is greatest near but slightly below total internal reflection. At and above total internal reflection, the light is totally reflected at the glass-liquid interface and therefore intensity no longer changes with temperature or input angle of incidence. Further down the light intensity curve, the measured intensity becomes less sensitive to changes in temperature and therefore can be masked by measurement noise. Adjusting the input angle of incidence shifts the light intensity curve with respect to temperature (shown in Figure 49 with changing line color gradient), which can provide a means for calibrating the temperature-sensitive area of the curve to the appropriate temperature range of the experiment.

4.2.3 Experimental Setup

Wall Temperature Optical Setup

The experimental setup is represented and labeled in Figure 50. A Siemens LGK 7628 HeNe laser module is used to generate a polarized, 5 mW, 632.8 nm beam. The beam

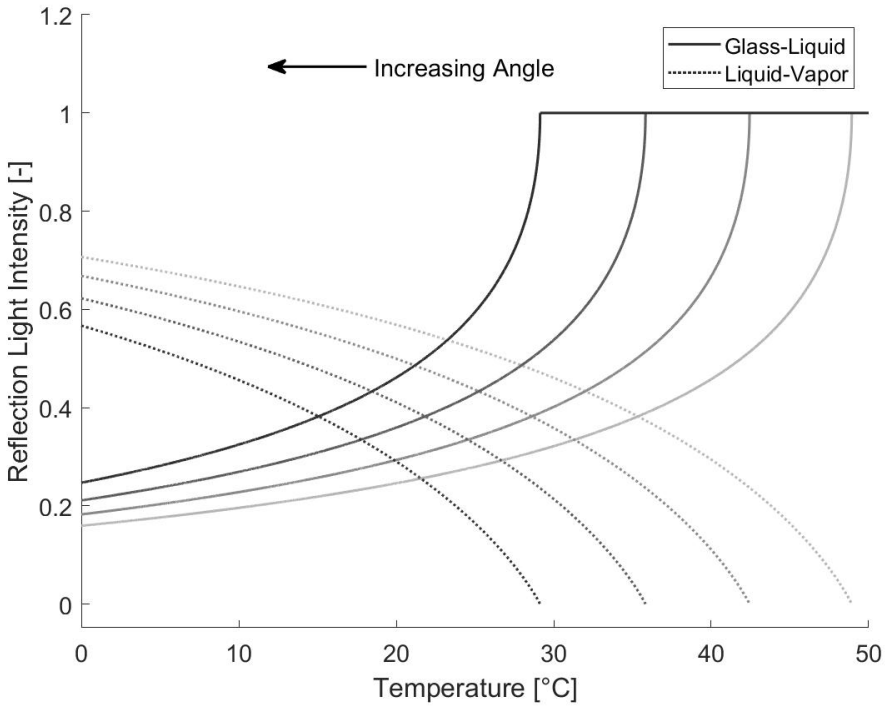

Figure 49: Calculated intensity of light reflected and transmitted at an interface of glass and liquid R245fa (Figure 48) at varying angles of incidence near and at the critical angle, shown with lines getting darker with increasing angle

is first directed through an iris diaphragm to remove stray light from the laser module. Following the first iris, the laser passes through a ThorLabs GL10-A Glan-Laser calcite polarizer to p-polarize the light (polarization parallel to the page). The polarized beam is reflected to the left at a near 90-degree angle using a mirror and passes through a second iris diaphragm to remove stray light produced in the polarizer. The beam is redirected left (about 50 degrees) towards the test section optics by a second mirror. After exiting the test section optics, the beam passes through two final iris diaphragms to minimize undesirable reflections from the R245fa liquid-vapor interface in the test section. The beam is then absorbed by a Thorlabs PDA36A switchable gain, amplified silicone light detector (referenced as the main photodiode).

A portion of the main laser beam is reflected in the Glan-Laser polarizer and escapes

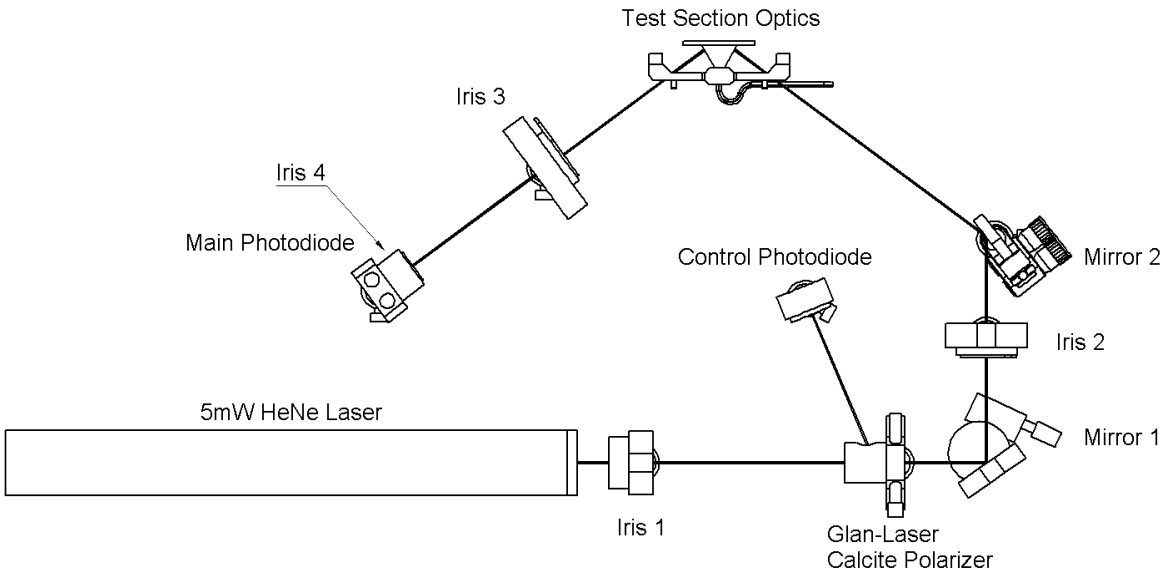

Figure 50: Simplified wall temperature optics setup, shown from above with components labeled

out of a side port on the left side of the lens holder. The reflected light is absorbed by a Thorlabs PDA55 silicone light detector (referenced as the control photodiode) and is used to calibrate the main beam.

The laser module was fixed directly to the platform while the other optical components were mounted on fine-adjustment stages. The second mirror was mounted on a Thorlabs GMB1 full gimbal mount for precise adjustment of the input angle into the test section optics.

Test Section Optics

The test section optical setup is shown in Figure 51 with all optical materials included. The laser beam first contacts the test section optics at the air-prism interface, typically at a low angle of incidence (α) such as 6-7 degrees. The beam then travels through the

BK7 equilateral prism, immersion oil, BK7 test section window, fluorine-doped tin oxide (FTO) coating, and POE compressor oil before reaching the POE-liquid interface (the interface of interest). The beam undergoes slight changes to trajectory and loses some light intensity to reflection and absorption. Some light is refracted and lost through the POE-liquid interface but most is reflected and passes back out of the test section optics using a similar path as the input light, shown in Figure 51.

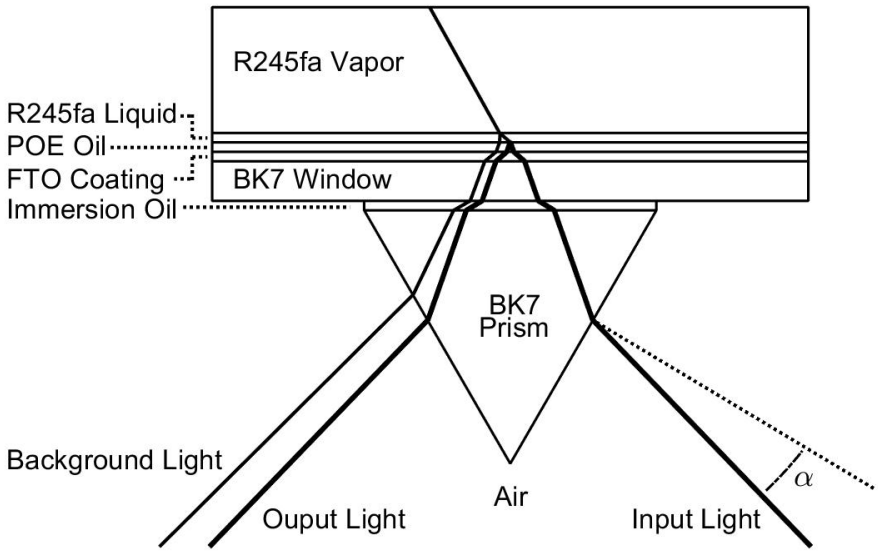

Figure 51: Test section optics with laser beam path, dimensions not to scale and light ray angles exaggerated

Starting with the input angle of incidence, (α), the angles of input and transmittance at each interface are found using Snell's Law (Equation 7) and the material indices of refraction, shown in Table 8.

After calculating the light angles and tracing the path of the laser, the amount of light reflected at each interface is calculated using the Fresnel coefficients (Equations 7

Table 8: Test section optical materials in the order encountered by the input laser beam, refractive indices for 632.8 nm light wavelength and a 15-35 °C temperature range

Order	Material	Refractive Index
1	Air	1.0002 [a]
2	BK7 Prism	1.515 [b]
3	Immersion Oil	1.515 [c]
4	BK7 Window	1.515 [b]
5	FTO Coating	1.85 [d]
6	Polyolester Oil	1.458-1.451 [e]
7	R245fa Liquid	1.261-1.250 [f]
8	R245fa Vapor	0.999-1.003 [f]

[a] Ciddor [10]
[b] Schott, [12]
[c] Fisher Scientific, catalog # 50-753-2972
[d] Delta Technologies [15]
[e] Semenyuk et al. [16]
[f] Schmidt et al. [2]

and 8). The light intensity transmitted at a given interface is calculated as the reflected light subtracted from unity, shown in Equation 10.

$$T_p = (1 - R_p) \tag{10}$$

The ratio of light intensity exiting the prism to the input light intensity is given in terms of light reflected and transmitted at each interface, shown in final form in Equation 11 (referenced later as the reflectance model) using optical interface labels from Table 9.

$$\frac{I_{\text{out}}}{I_{\text{in}}} = T_{1,2,3}^2 R_4 + T_{1,2,3,4}^2 R_5 + T_{1,2,3,4,5}^2 R_6 \tag{11}$$

The light transmission coefficients are squared to account for light transmitting

through the interfaces a second time while exiting the test section optics. Even though the reflection off of the sixth interface is of the greatest interest, light reflected from the fourth and fifth interfaces follows a similar exit trajectory and is also absorbed by the main photodiode.

Table 9: Test section material interfaces for reference in Equation 11

Interface Label	Materials
1	Air — BK7 Prism
2	BK7 Prism — Immersion Oil
3	Immersion Oil — BK7 Glass
4	BK7 Glass — FTO Coating
5	FTO Coating — POE Compressor Oil
6	POE Compressor Oil — R245fa liquid
7	R245fa liquid — R245fa vapor

4.2.4 Calibration

The calibration procedure seeks to convert measured intensity ratio data to an absolute wall temperature by means of a physics-based calibration curve (the reflectance model, Equation 11). The intensity ratio and absolute pressure in the test section are measured while slowly increasing the absolute pressure in the test section. The flow in the test section is assumed to be a saturated mixture throughout the procedure as no heat is added at the wall. The absolute pressure is then converted to the saturation temperature in the test section using the Helmholtz energy equation of state [1] adapted for R245fa [36] and programmed into EES [17].

The measured intensity ratio is plotted against the calculated saturation temperature. The reflectance model curve is manually fit to the plotted data using the curve fitting parameters described in the subsequent section. The model, after curve fitting, is

then used to convert measured intensity ratio data to wall temperature.

Curve Fitting Parameters

Six parameters in the reflectance model have the greatest effect on the shape and position of the curve and are used to fit the curve to the calibration data. These parameters include the input angle of incidence, the critical angle cutoff ratio, the percentage of light reflected at the liquid-vapor interface (background light), the polarization of the light, the absorption extinction coefficient of frustrated total internal reflection, and the divergence of the laser beam.

The effect of three of these parameters on the model curve is illustrated in Figure 52. Increasing the input angle of incidence shifts the entire curve to the right without altering the shape of the curve. The cutoff ratio shifts the entire curve up or down in intensity ratio by setting the highest limit of the curve, also without changing the shape of the curve. Increasing the background light raises the curve at otherwise low values of intensity ratio.

The effect of frustrated total internal reflection (FTIR) must also be included in the reflectance model due to the thin layer of FTO at the boundary of total internal reflection. To implement FTIR, an imaginary, out-of-phase, absorptive component, κ, is added to the real index of refraction of R245fa, shown in Equation 12.

$$N_{\mathrm{R245fa}} = n_{\mathrm{R245fa}} + i\kappa \tag{12}$$

The value of κ becomes one of the reflectance model curve fitting parameters. Increasing κ from zero removes the discontinuity and smooths the transition between the

model curve and the cutoff ratio.

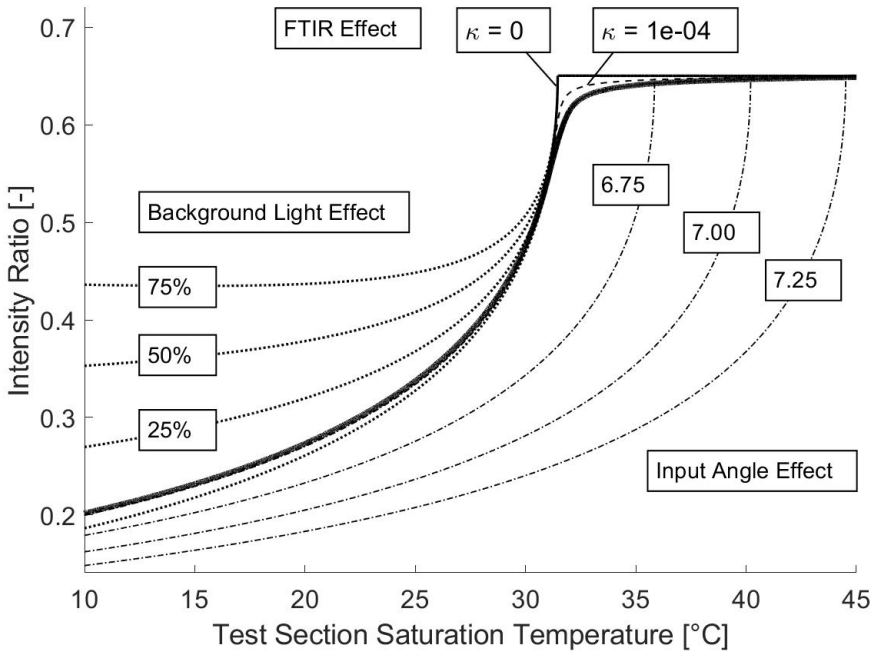

Figure 52: Effects of a few of the curve fitting parameters (input angle of incidence, background light, and frustrated total internal reflection), final curve shown by the dark, solid line

The polarization and beam divergence each share similar effects with one of the parameters shown in Figure 52. Decreasing the percentage of p-polarization (increasing s-polarization) of the laser light raises the model curve at lower temperatures, similar to the effect of increasing the background light. Increasing the angle of laser beam divergence smooths the curve just before the cutoff ratio, similar to the effect of FTIR.

Calibration Procedure Results

Data from a single calibration procedure is shown in Figure 53 with the resulting reflectance model curve fit. The parameters used in the model curve are presented in Table 10.

The reflectance model curve fits within the bounds of the measured data, providing a good intensity ratio to wall temperature conversion over the range of temperature shown.

Table 10: Curve fitting parameters used in Figure 53

Parameter	Value
α	6.34°
Cutoff Ratio	0.585 [-]
Background Light	5%
P-polarization	95%
κ	9.5e-05 [-]
Beam Divergence	0.021°

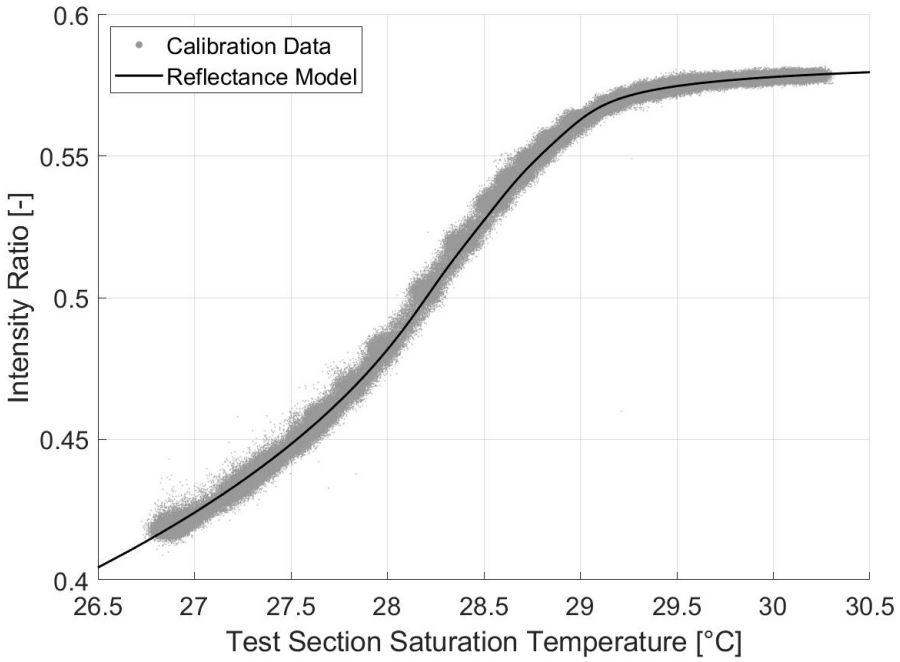

Figure 53: Calibration data with reflectance model curve fit, applied using parameters from Table 10

Sensitivity to Film Thickness

The measured intensity ratio and the corresponding calculated wall temperature are independent of changes in the liquid film thickness. The calculated wall temperature, normalized with the saturation temperature in the test section, for two calibration data sets are shown in Figure 54 as a function of liquid film thickness. Wall temperature data above 29 °C was omitted due to the significant error introduced near the cutoff ratio.

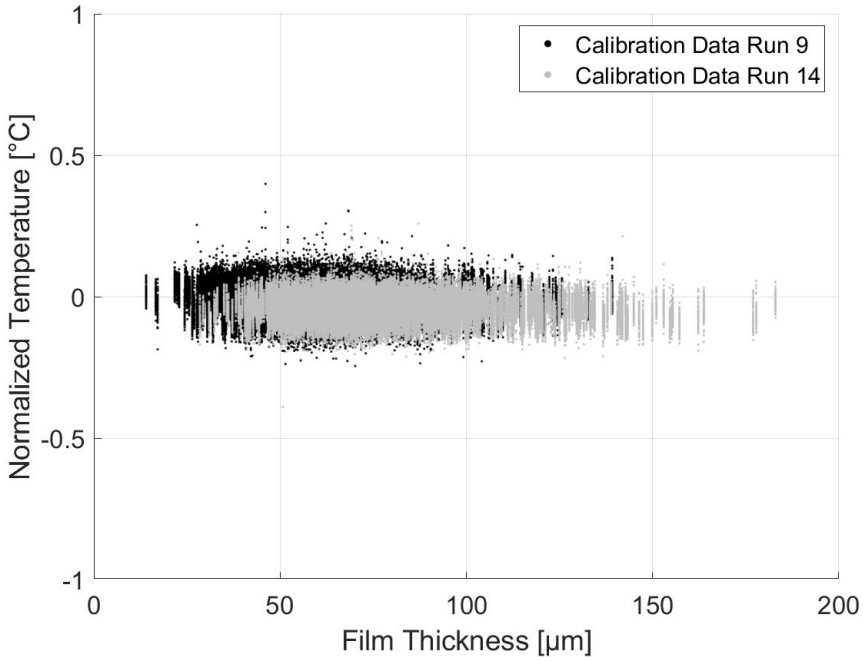

Figure 54: Normalized wall temperature variation with liquid film thickness

4.2.5 Results and Analysis

The calibrated wall temperature results from a pulsatile flow at a frequency of 10 Hz are shown in Figure 55 over a 4 second time period. The light intensity ratio was measured while forcing a consistent train of vapor pulses through the test section. The measured intensity ratio was then converted to wall temperature using the calibration model curve

(Figure 54). Temperature fluctuations at the test section wall can be seen clearly in the resulting data despite the small oscillation amplitude of 0.1°C.

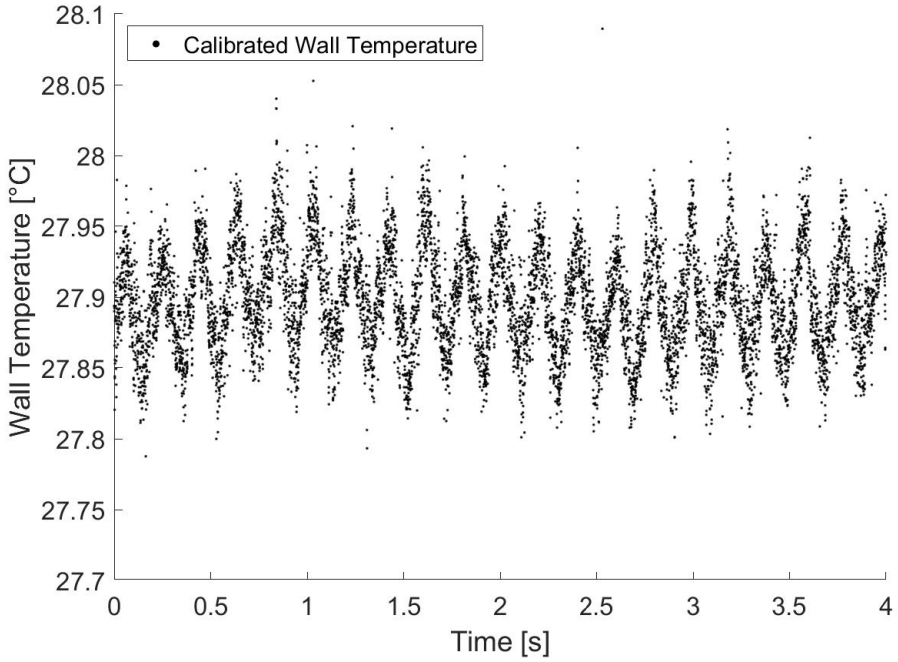

Figure 55: Calibrated wall temperature vs time, measured intensity ratio converted to wall temperature using the calibration reflectance model curve (Figure 53)

Error Analysis

Several of the most significant sources of error in the optical wall temperature technique have been recognized and adjusted for in the reflectance model, using the curve fitting parameters (Table 10), to provide good agreement with the collected data.

Despite fixing the optical components and the input angle of incidence of the light beam, the trajectory of the output light beam is not perfectly constrained. Over a large range in temperature, the output beam can shift due to thermal expansion of the optical components. This slight shift can cause part of the output beam to be blocked by Iris 3 and 4 (Figure 50), leading to an inaccurate intensity ratio measurement. However,

the output beam shifts so little that increasing the diameter of the irises was enough to eliminate this error.

Some light intensity is lost while passing through each optical material, resulting in a lower absolute measured intensity ratio compared to the reflectance model. This simply causes a shift in the absolute position of the curve and can be correctly adjusted using the cutoff ratio curve fitting parameter.

Background light from the liquid-vapor interface can introduce significant measurement noise at intensity ratios far from the critical angle cutoff ratio. At a low measured intensity ratio, more light reaches and is reflected at the liquid-vapor interface. Furthermore, the intensity ratio is less sensitive to changes in temperature in this portion of the reflectance model curve and more sensitive to measurement noise. Background light was added as a curve fitting parameter to the reflectance model to account for the model curve rising in the low sensitivity portion of the model.

The laser beam is highly polarized in the parallel direction (i.e. parallel to the page in Figure 50) after the Glan-Laser Calcite Polarizer, but whether it remains 100% p-polarized depends on the alignment of the optical components and the test section. To account for some s-polarized light, both Fresnel reflection coefficients (Equations 7 and 8) are used in the reflectance model and the amount of p-polarized light is specified as a curve fitting parameter.

The size and divergence of the laser beam limits the spatial resolution of the optical technique. Even though the laser beam is produced with a diameter of 0.8 mm and the diameter is reduced slightly by the iris diaphragms, the beam is still quite large for a point measurement. In addition, the beam likely diverges up to a few milliradians which effectively causes the light to contact the interface of interest at a range of different

angles. The beam divergence curve fitting parameter includes a small range of angles in addition to the input angle of incidence to account for the decreased spatial resolution of the actual laser beam. This error could be reduced further by concentrating the source light to a smaller, starting diameter.

Although dependent on temperature, the indices of refraction of the test section optical materials are assumed to be constant with temperature in the reflectance model, with the exception of R245fa and the POE oil. This may introduce some error, most significantly in predicting the exact input angle of incidence, due to the change in refractive index of air with the room temperature. However, holding the refractive indices constant may be a decent approximation because the change in refractive index of BK7 glass (roughly 6×10^{-5} °C) is several orders of magnitude smaller than the R245fa and POE oil and the reflectance model is unaffected by small changes in the refractive index of either the immersion oil or the FTO coating.

5 Vertical Annular Two-Phase Pulsatile Flow

Vertical annular two-phase flow results are presented at a variety of pulsing frequencies between 0.5-10 Hz with each window of the test section heated with 20 W of power. The wall temperature and film thickness were measured using methods described in the Measurement Methods and Results section and time-synchronized using the trigger signal from the high-speed camera. The pulse generator vapor mass flow rate was calculated using pressure differential data from the Dwyer Pitot tube, located just before the pulse generator stepper motor-controlled valve. The temperature and pressure data were collected at 2000 Hz and the film thickness sample frequency was 250 Hz for all runs presented. The following data was collected on 2018-6-20. Acronyms were used to shorten the axis labels and prevent cluttering on the subplots. The meaning of each acronym label is shown in Table 11.

Table 11: Subplot labeling nomenclature

Acronym	Meaning
FT	Film Thickness
WT	Wall Temperature
PGV MF	Pulse Generator Vapor Mass Flow Rate
FFT	Fast Fourier Transform
PSD	FFT Power Spectral Density
Avg	Average
Std Dev	Standard Deviation

5.1 Results

The wall temperature, film thickness, and pulse generator mass flow rate for 0.5 Hz and 3 Hz pulsed data are shown in Figures 56 and 57. Changes in the wall temperature and

film thickness are clearly visible for both pulsing frequencies. The pulse generator vapor mass flow rate measurements have a high sampling error. Work is currently being done to improve these measurements.

The film thickness for 0.5 Hz and 4 Hz pulsed data is shown in Figure 56 and 59 and are presented along with the film thickness frequency distribution and Fast Fourier transform power spectrum density. A spike is clearly visible at each pulsing frequency and the oscillating effects can be seen in each film thickness time trace.

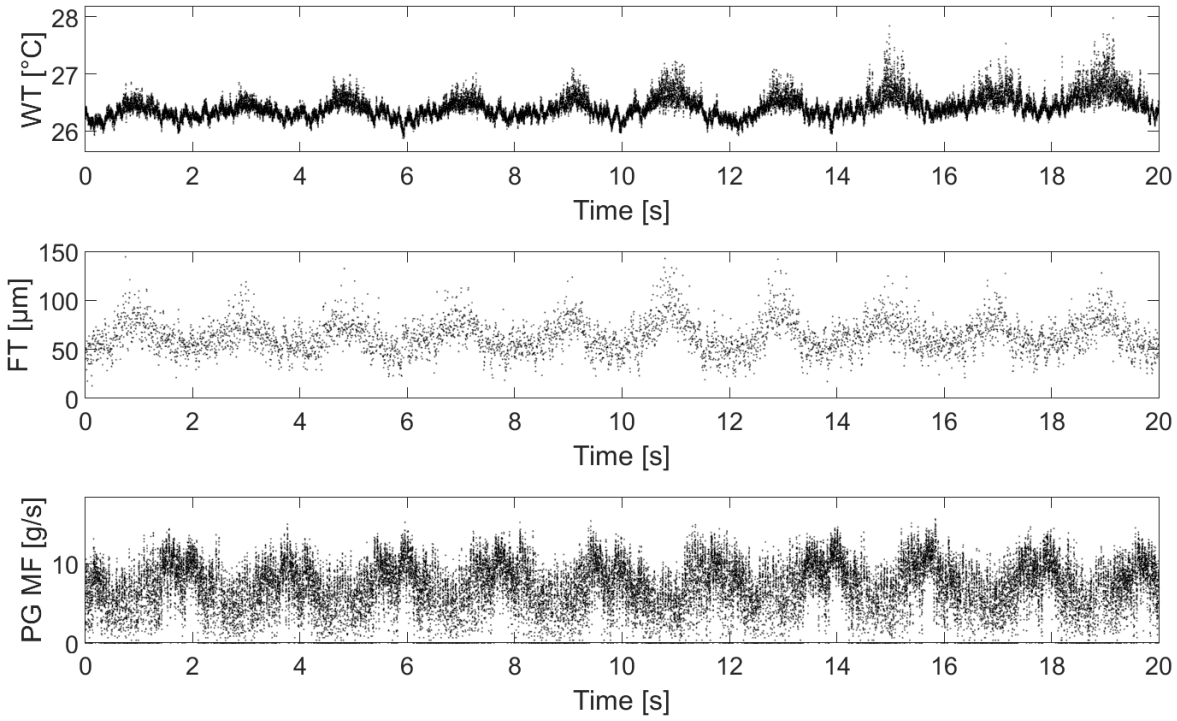

Figure 56: 0.5 Hz pulsed, 20W heated data

The average film thickness and the standard deviation are shown in Figure 60 for pulsing frequencies 0-10 Hz and window heating power of 20 W. Despite the instantaneous fluctuations in the film thickness (shown most clearly by Figures 56) in pulsatile flow, the average film thickness and deviation change little for the different pulsing frequencies (Figure 60). The most significant difference exists between the pulsed data and the

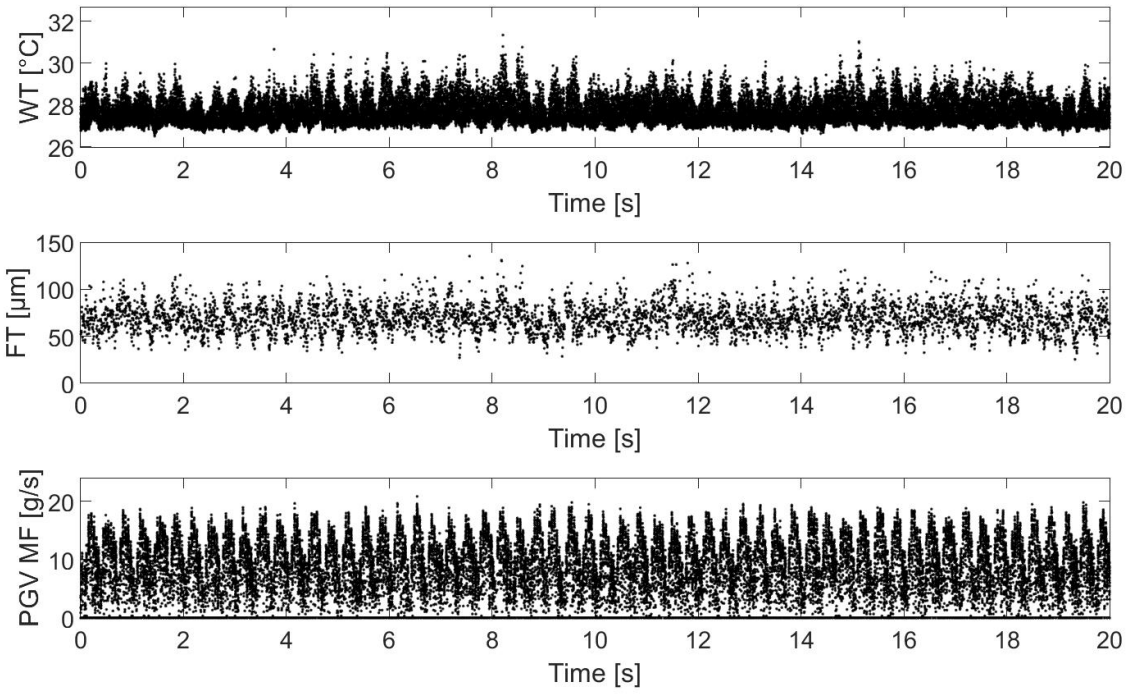

Figure 57: 3 Hz pulsed, 20W heated data

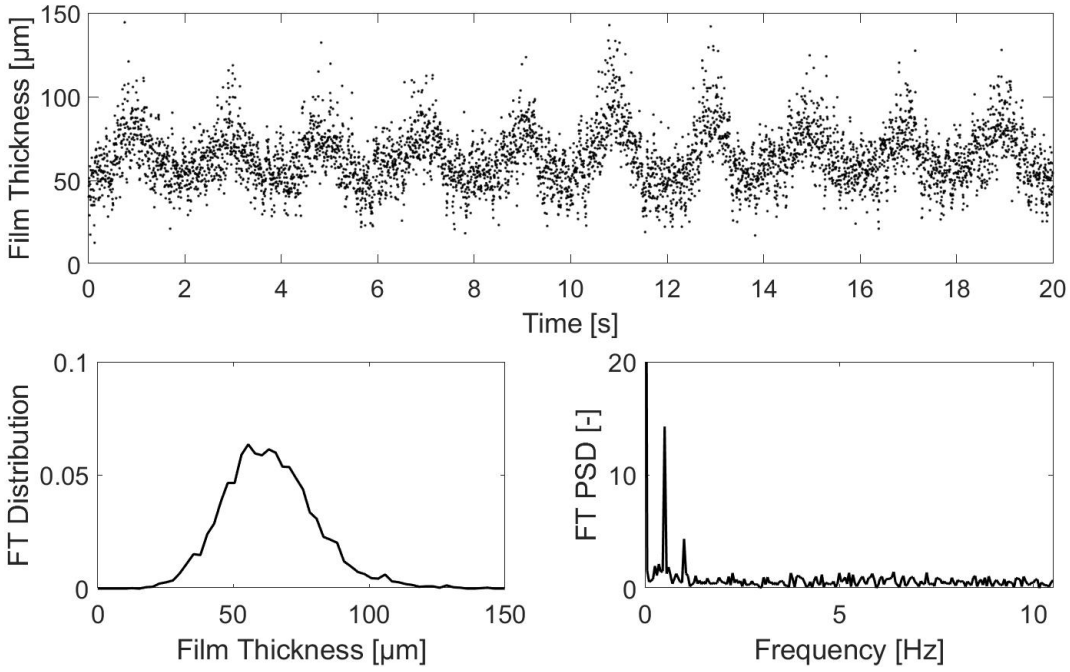

Figure 58: Film thickness for 0.5 Hz pulsed, 20 W heated data

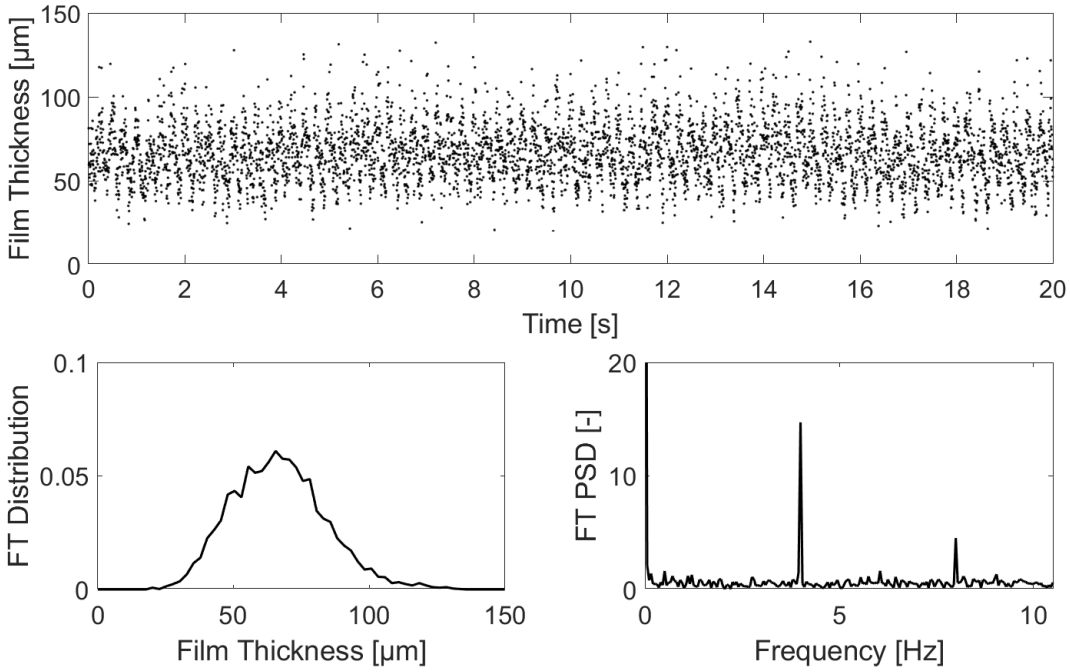

Figure 59: Film thickness for 4 Hz pulsed, 20 W heated data

steady data point. Both the average film thickness and standard deviation decrease once the flow is pulsatile. Increasing the vapor flow rate and consequently the pressure in the test section has consistently had the effect of decreasing the average film thickness and increasing the stability of the flow.

The time trace, temperature distribution, and Fast Fourier transform of the wall temperature with 0.5 Hz pulses is shown in Figure 61.

The wall temperature and fluctuation range (+/- 2 standard deviations) for pulsing frequencies between 0.5-10 Hz are shown in Figure 62. The wall temperature increases around 3 Hz but then decreases to previous levels around 7 Hz in the data presented. This may be an effect of the pulse generator vapor temperature increasing around the same range of pulsing frequencies. The wall temperature, normalized with the saturation temperature, is shown for pulsing frequencies of 0.5, 3, 7.5, and 10 Hz (Figures 63, 64,

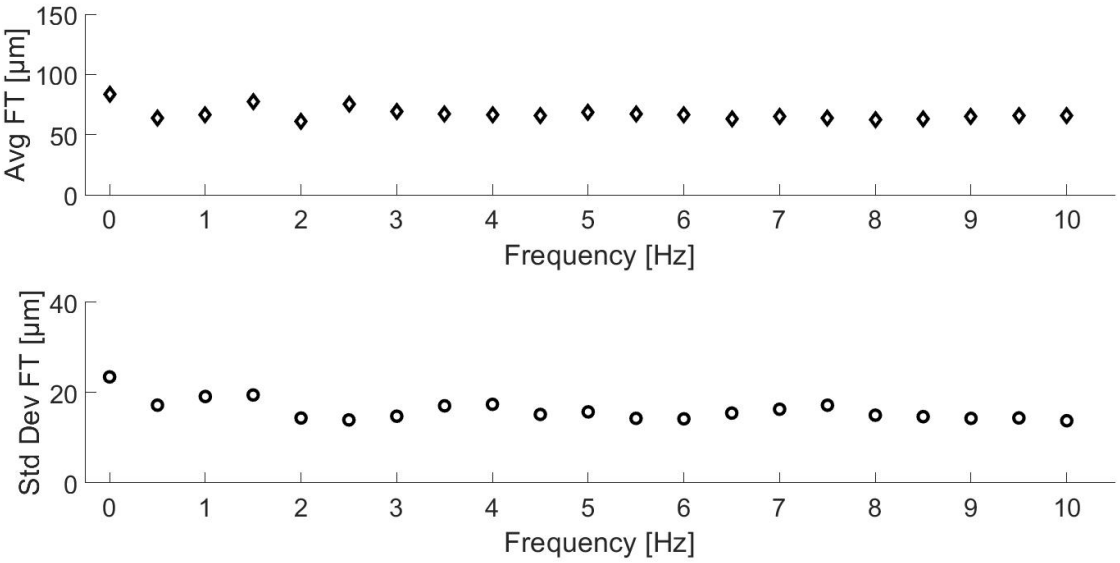

Figure 60: Average film thickness and the standard deviation for different pulsing frequencies

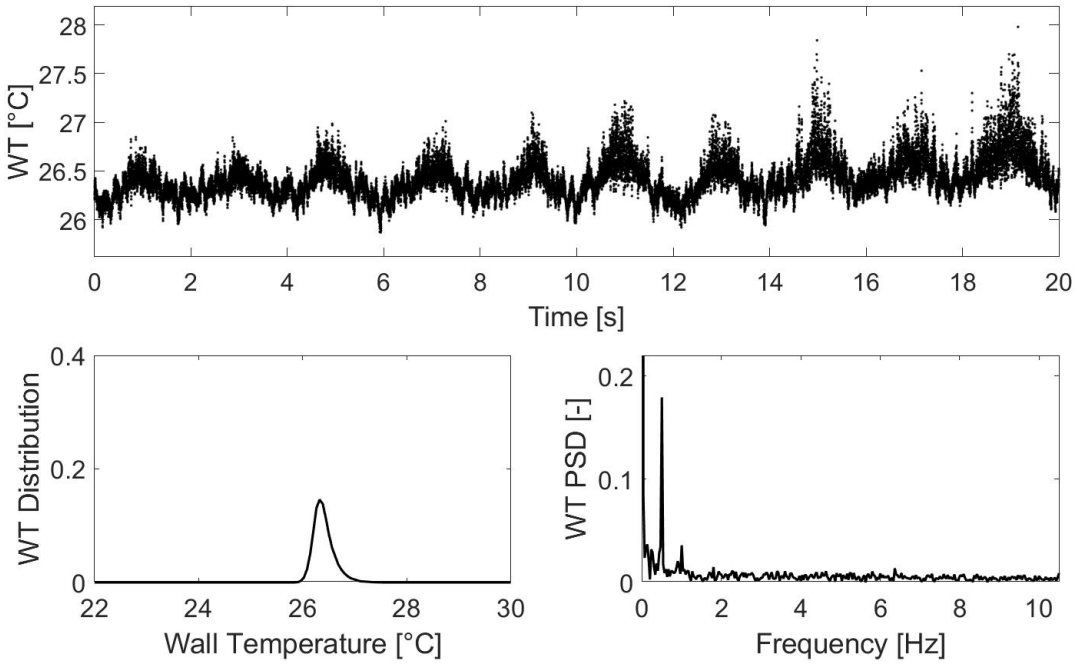

Figure 61: Wall temperature for 0.5 Hz pulsed, 20 W heated data

65, 66). The frequency detected by the FFT was stronger once the temperatures were normalized, shown by the temperature power spectrum density scale increase between

Figure 61 and 63.

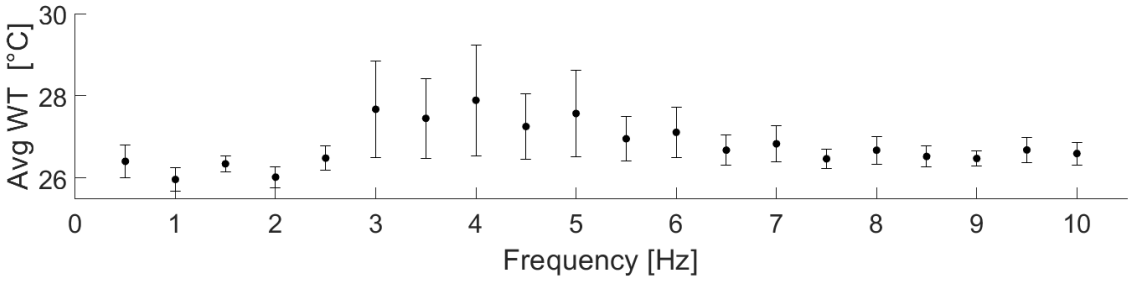

Figure 62: Average wall temperature with fluctuations of +/- 2 standard deviations for different pulsing frequencies

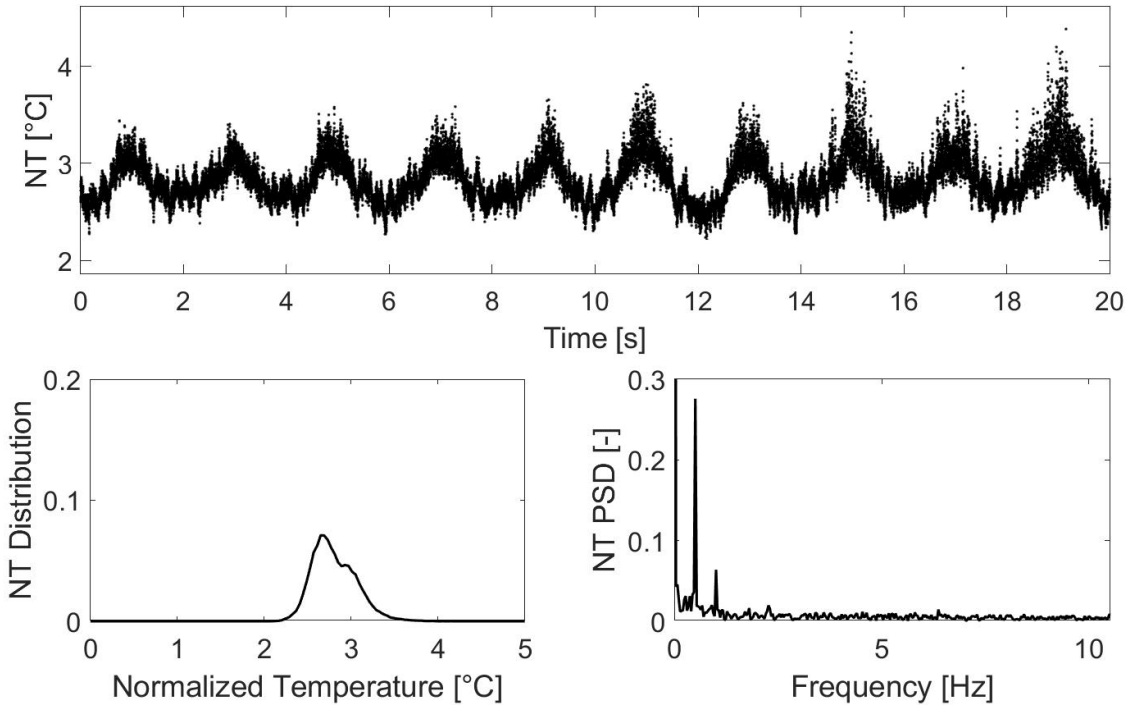

Figure 63: Normalized temperature for 0.5 Hz pulsed, 20 W heated data

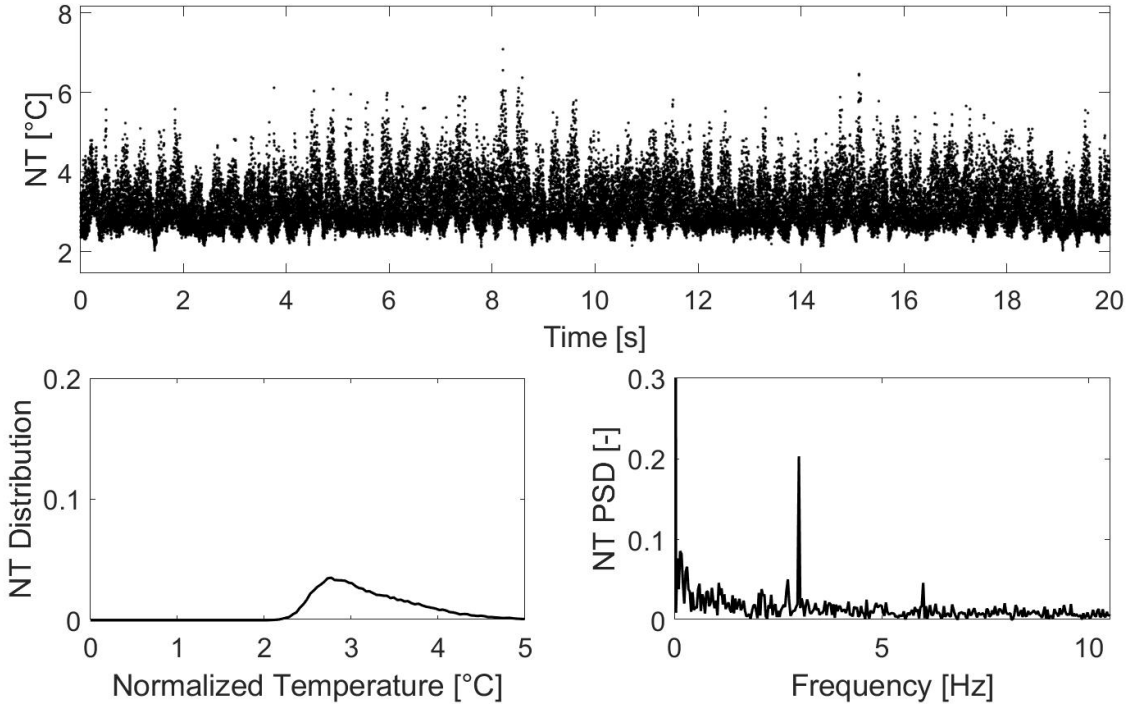

Figure 64: Normalized temperature for 3 Hz pulsed, 20 W heated data

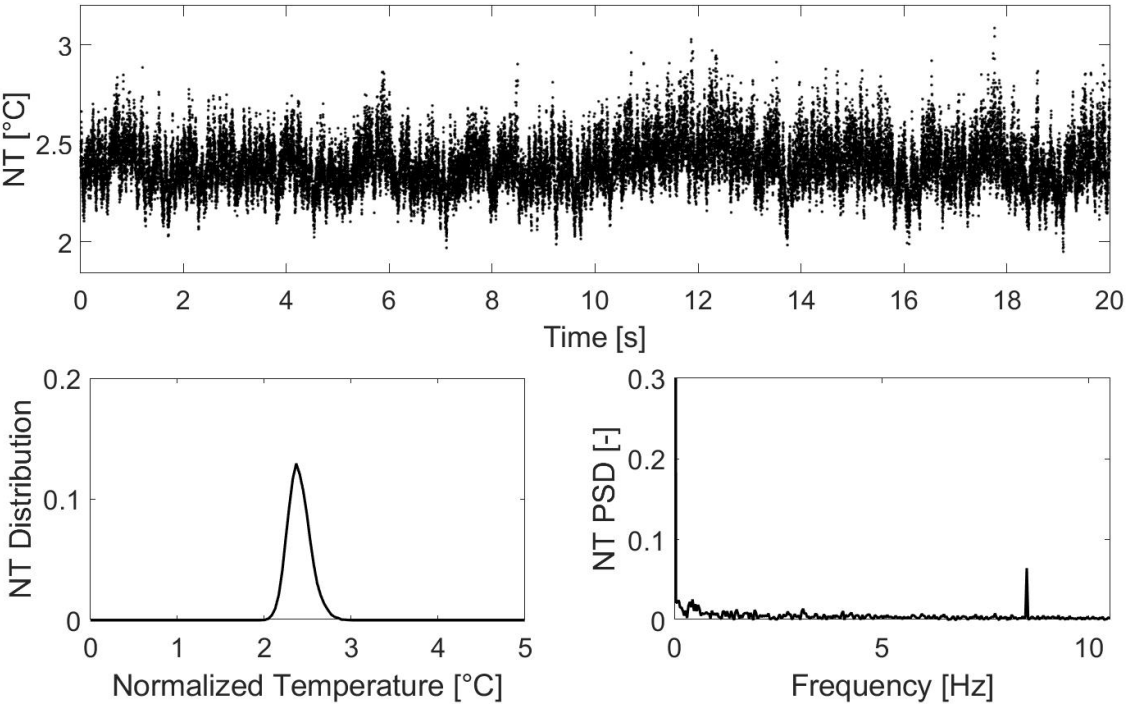

Figure 65: Normalized temperature for 7.5 Hz pulsed, 20 W heated data

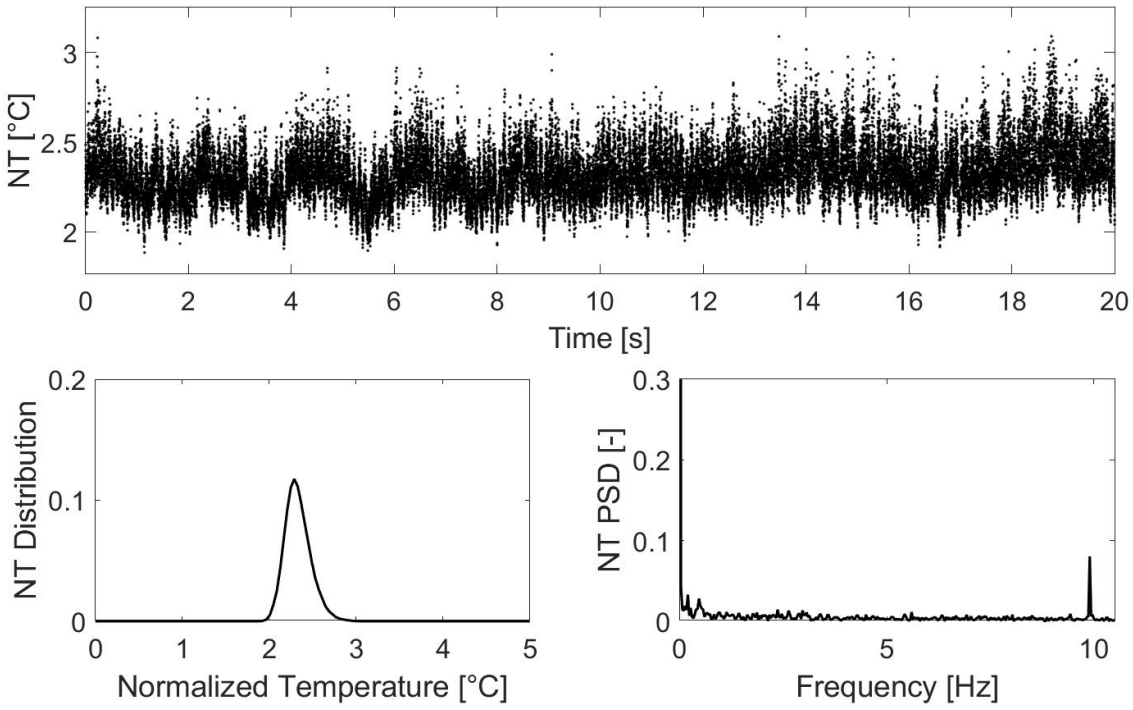

Figure 66: Normalized temperature for 10 Hz pulsed, 20 W heated data

6 Conclusions

A pulse generator was designed, constructed, and installed in the Annular Flow facility in order to develop and study vertical annular two-phase pulsatile flow. The optical techniques used to measure the liquid film thickness and wall temperature were greatly improved and synchronized for direct comparison and further calculations. The instantaneous film thickness and wall temperature were measured and synchronized for a variety of pulsing frequencies. These measurements can be used to calculate the wall shear and heat transfer coefficient of vertical annular two-phase pulsatile flow.

References

[1] S. Klein and G. Nellis. *Thermodynamics*. Cambridge University Press (2012).

[2] J. Schmidt, E. Carillo-Nava, and M. Moldover. "Partially halogenated hydrocarbons CHFCl-CF3, CF3-CH3, CF3-CHF-CHF2, CF3-CH2-CF3, CHF2-CF2-CH2F, CF3-CH2-CHF2, CF3-0-CHF2: critical temperature, refractive indices, surface tension and estimates of liquid, vapor and critical densities." *Fluid Phase Equilibria* Vol. 122 (1996): pp 187-206.

[3] M. Rodarte. "Liquid Film and Droplet Behavior in Adiabatic and Diabatic Vertical Annular Flow." Ph.D. Thesis. University of Wisconsin-Madison. 2015.

[4] S. Vanden Hogen. "Micro-scale Visualization and Characterization of Vertical Annular Flow: A Study of Working Fluid and Tube Geometry." M.S. Thesis. University of Wisconsin- Madison. 2013.

[5] D. Rodriguez. "Characterization of Bubble Entrainment, Interfacial Roughness and the Sliding Bubble Mechanism in Horizontal Annular Flow." Ph.D. Thesis. University of Wisconsin-Madison. 2004.

[6] Q. Chen, Y. Li, and J.P. Longtin. "Real-time laser-based measurement of interface temperature during droplet impingement on a cold surface." *International Journal of Heat and Mass Transfer* Vol. 46 (2003): pp. 879-888.

[7] E. Hurlburt and T. Newell. "Optical measurement of liquid film thickness and wave velocity in liquid film flows. Experiments in Fluids." 21:357-362.

[8] G. Hewitt, and N. Hall-Taylor. *Annular Two-Phase Flow*. Pergamon Press (1969).

[9] E. Hurlburt and T. Newell. "Characteristics of Refrigerant Film Thickness, Pressure Drop, and Condensation Heat Transfer in Annular Flow." *HVAC&R Research* Vol. 5 No. 3 (1999): pp. 229-249.

[10] P. Ciddor. "Refractive Index of Air: New Equations for the Visible and Near Infrared." *Applied Optics* Vol. 35 No. 9 (1995): pp. 1566-1573.

[11] Schott Advanced Optics. "Temperature Coefficient of the Refractive Index." TIE-19 (2016): pp. 1-10.

[12] Schott Advanced Optics. "Optical Glass Data Sheets." (2017): pp. 17.

[13] A. Bashkatov and E. Genina. "Water Refractive Index in Dependence on Temperature and Wavelength: a Simple Approximation." *Optical Technologies in Biophysics and Medicine* Vol. 5068 (2003): pp. 393-395.

[14] T. Q. Qiu, C. P. Grigoropoulos, and C. L. Tien. "Novel Technique for Noncontact and Microscale Temperature Measurements." *Experimental Heat Transfer* Vol. 6 (1993): pp. 231-241.

[15] Delta Technologies. *delta-technologies.com*

[16] Y. V. Semenyuk, V. V. Sechenyh, V. P. Zhelezny, and P. V. Skripov. "Thermophysical Properties of Compressor Oils for Refrigerating Plant." *Journal of Synthetic Lubrication* Vol. 25 (2008): pp. 57-73.

[17] S. A. Klein. *Enginering Equation Solver*. F-Chart Software. (2018). www.fChart.com

[18] J. P. Longtin and C. H. Fan. "Laser-Based Temperature Measurement at a Liquid Surface." *Heat Transfer* Vol. 4 (1998): pp. 119-123.

[19] C. H. Fan and J. P. Longtin. "Laser-Based Measurement of Liquid Temperature or Concentration at a Solid-Liquid Interface." *Experimental Thermal and Fluid Science* Vo. 23 (2000): pp 1-9.

[20] A. S. Lee and P. M. Norris. "A New Optical Method for Measuring Surface Temperature at Large Incident Probe Angles." *Review of Scientific Instruments* Vol. 68 (1996): pp. 1307-1311.

[21] T. A. Shedd and B. W. Anderson. "An Automated Non-Contact Wall Temperature Measurement Using Thermoreflectance." *Measurement Science and Technology* Vol. 16 (2005): pp. 2483-2488.

[22] T. H. Kim, E. Kommer, S. Dessiatoun, J. Kim. "Measurement of Two-Phase Flow and Heat Transfer Parameters Using Infrared Thermometry." *International Journal of Multiphase Flow* Vol. 40 (2012): pp. 56-67.

[23] C. Gerardi, J. Buongiorno, L. Hu, T. McKrell. "Study of Bubble Growth in Water Pool Boiling through Synchronized, Infrared Thermometry and High-speed Video." *International Journal of Heat and Mass Transfer* Vol. 53 (2010): pp. 4185-4192.

[24] S. Kim and I. Mudawar. "Theoretical Model for Local Heat Transfer Coefficient for Annular Flow Boiling in Circular Mini/Micro-Channels." *International Journal of Heat and Mass Transfer* Vol. 73 (2014): pp. 731-742.

[25] T. Okawa, T. Goto, J Minamitani, and Y. Yamagoe. "Liquid Film Dryout in a Boiling Channel under Flow Oscillation Conditions." *International Journal of Heat and Mass Transfer* Vol. 52 (2009): pp. 3665-3675.

[26] T. Okawa, A. Kotani, I Kataoka, and M. Naito. "Prediction of Critical Heat Flux in Annular Flow Using a Film Flow Model." *Journal of Nuclear Science and Technology* Vol. 40 No. 6 (2003): pp. 388-396.

[27] T. Okawa, T. Goto, and Y. Yamagoe. "Liquid Film Behavior in Annular Two-Phase Flow under Flow Oscillation Conditions." *International Journal of Heat and Mass Transfer* Vol. 53 (2010): pp. 962-971.

[28] D. Groeneveld. "Post-Dryout Heat Transfer at Reactor Operating Conditions." *National Topical Meeting on Water Reactor Safety.* Salt Lake City, UT, March 26-28, 1973.

[29] D. Schubring, A. C. Ashwood, T. A. Shedd, and E. T. Hurlburt. "Planar Laser-Induced Fluorescence (PLIF) Measurements of Liquid Film Thickness in Annular Flow. Part I: Methods and Data." *International Journal of Multiphase Flow* Vol. 36 (2010): pp. 815-824.

[30] J. Klausner, L. Zeng, and D. Bernhard. "Development of a Film Thickness Probe Using Capacitance for Asymmetrical Two-Phase Flow with Heat Addition." *Review of Scientific Instruments* Vol. 63 (1992): pp. 3147-3152.

[31] A. Cokmez-Tuzla, K. Tuzla, and J. Chen. "Experimental Assessment of Liquid-Wall Contacts in Post-CHF Convective Boiling." *Nuclear Engineering and Design* Vol. 139 (1993): pp. 97-103.

[32] M. Ozawa, H. Umekawa, K. Mishima, T. Hibiki, and Y. Saito. "CHF in Oscillatory Flow Boiling Channels." *Transactions of the Institution of Chemical Engineers* Vol. 79 (2001): pp. 389-401.

[33] J. Asali and T. Hanratty. "Interfacial Drag and Film Height for Vertical Annular Flow." *American Institute of Chemical Engineers* Vol. 31 No. 6 (1985): pp. 895-902.

[34] G. Wallis. "Annular Two-Phase Flow Part1: A Simple Theory." *Journal of Basic Engineering* (1970): pp. 59-72.

[35] B. Azzopardi. "Drops in Annular Two-Phase Flow." *International Journal of Multiphase Flow* Vol. 23 (1997): pp. 1-53.

[36] E. Lemmon. "Short Fundamental Equations of State for 20 Industrial Fluids." *Journal of Chemical Engineering Data* Vol. 51 (2006): pp. 785-850.

[37] Honeywell. "Honeywell Enovate 245fa Technical Information." (2017). https://www.fluorineproducts-honeywell.com/blowingagents/wp-content/uploads/2018/12/470-Solstice-Enovate-245fa-Tech-Datasheet-v4-WEB.pdf.

7 Appendix

7.1 Part Drawings

The CAD models included in this thesis differ in dimensional tolerance depending on the creator of the individual component and the design intentions for the CAD model. Mark Rodarte's test section was constructed several years ago and no complete CAD models could be located. A new CAD model was built based on drawings from Mark's thesis and measurements of the actual structure. The model was made as accurate as possible to allow other components to be designed from model dimensions. Most of the remaining CAD models were created before production and don't include tolerances or manufacturing mistakes.

All dimensions in the following drawings are in inches.

7.1.1 Test Section

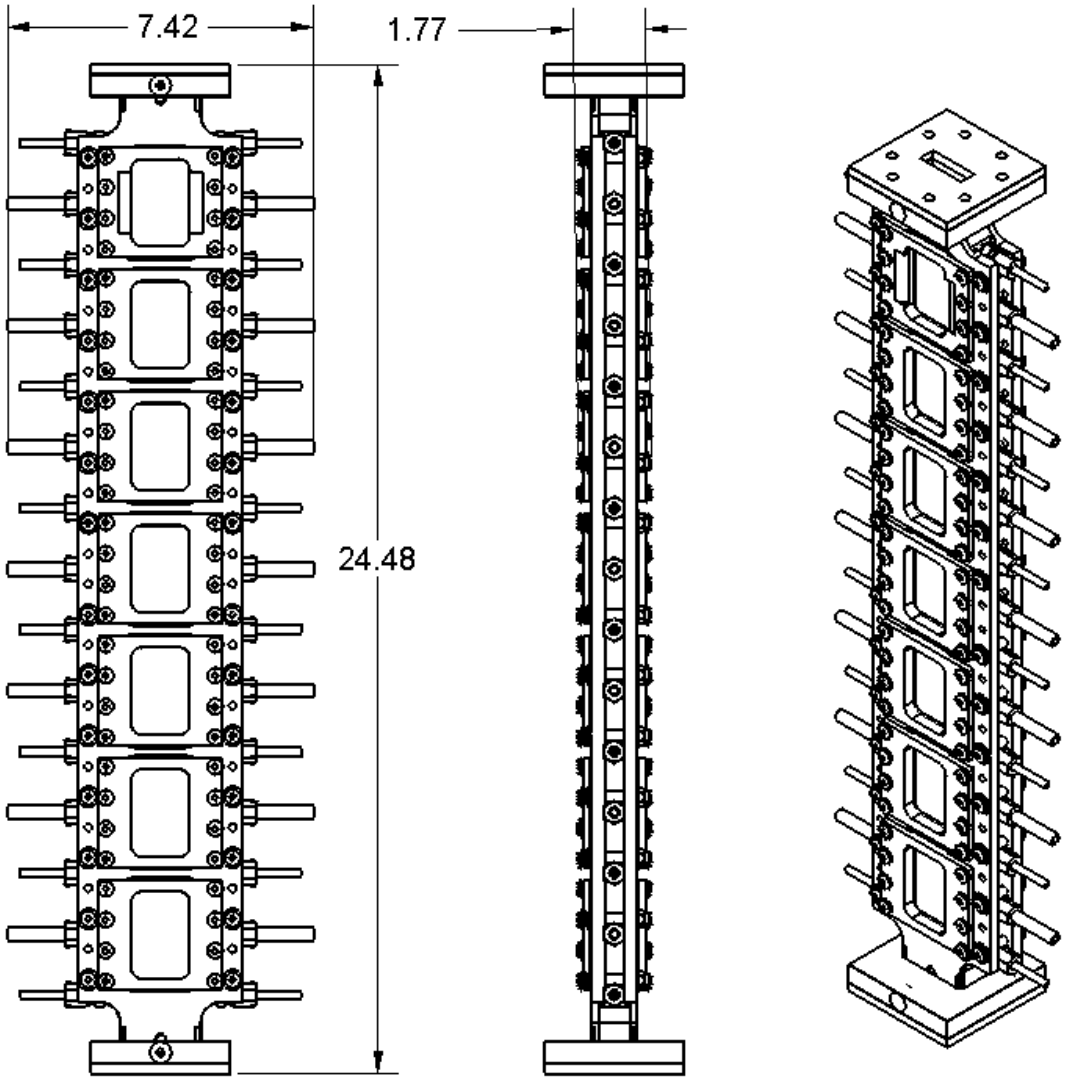

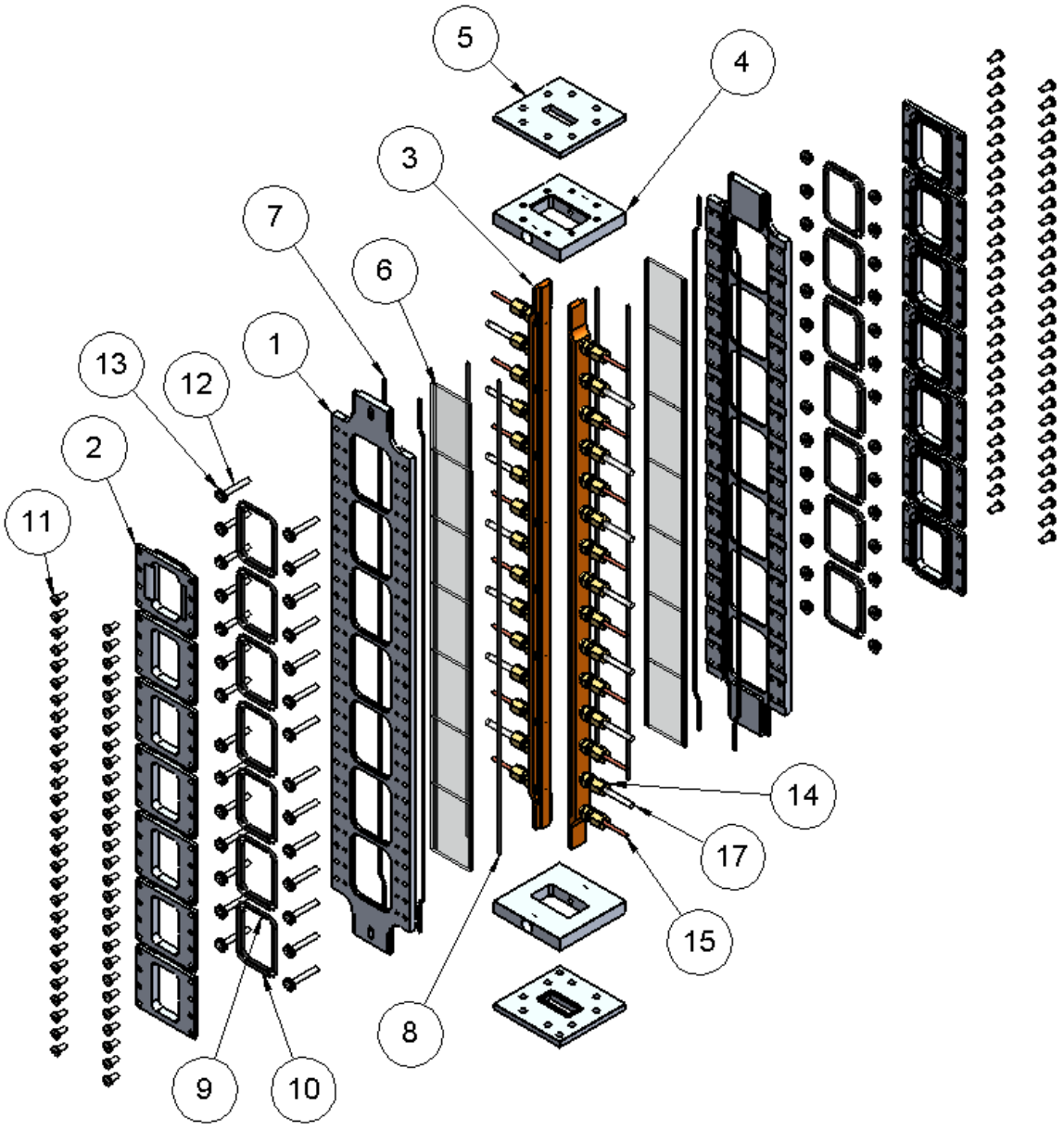
5
4
3
7
6
1
13
12
2
11
14
17
15
8
9
10

1 - Front/Back Plate

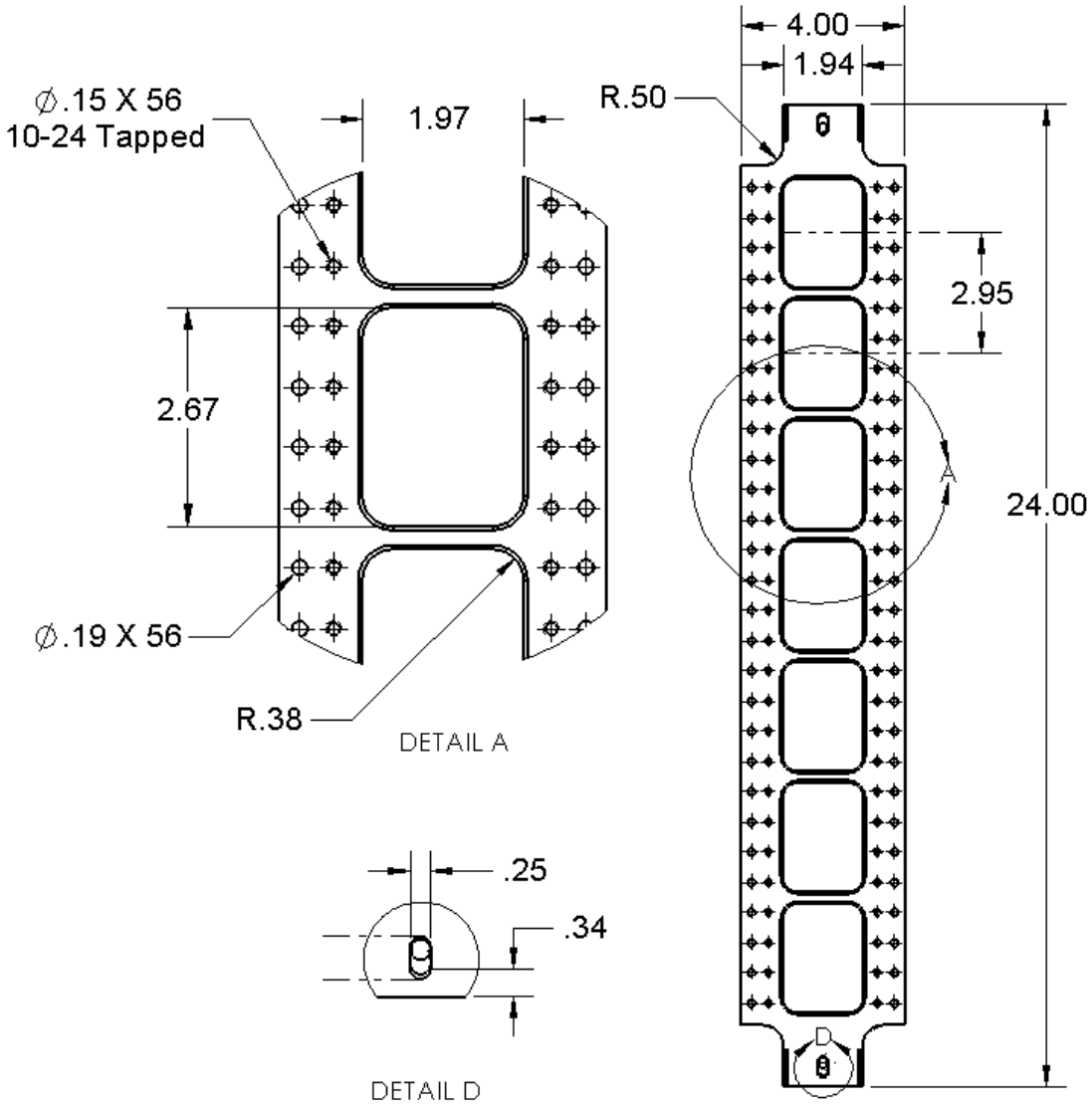

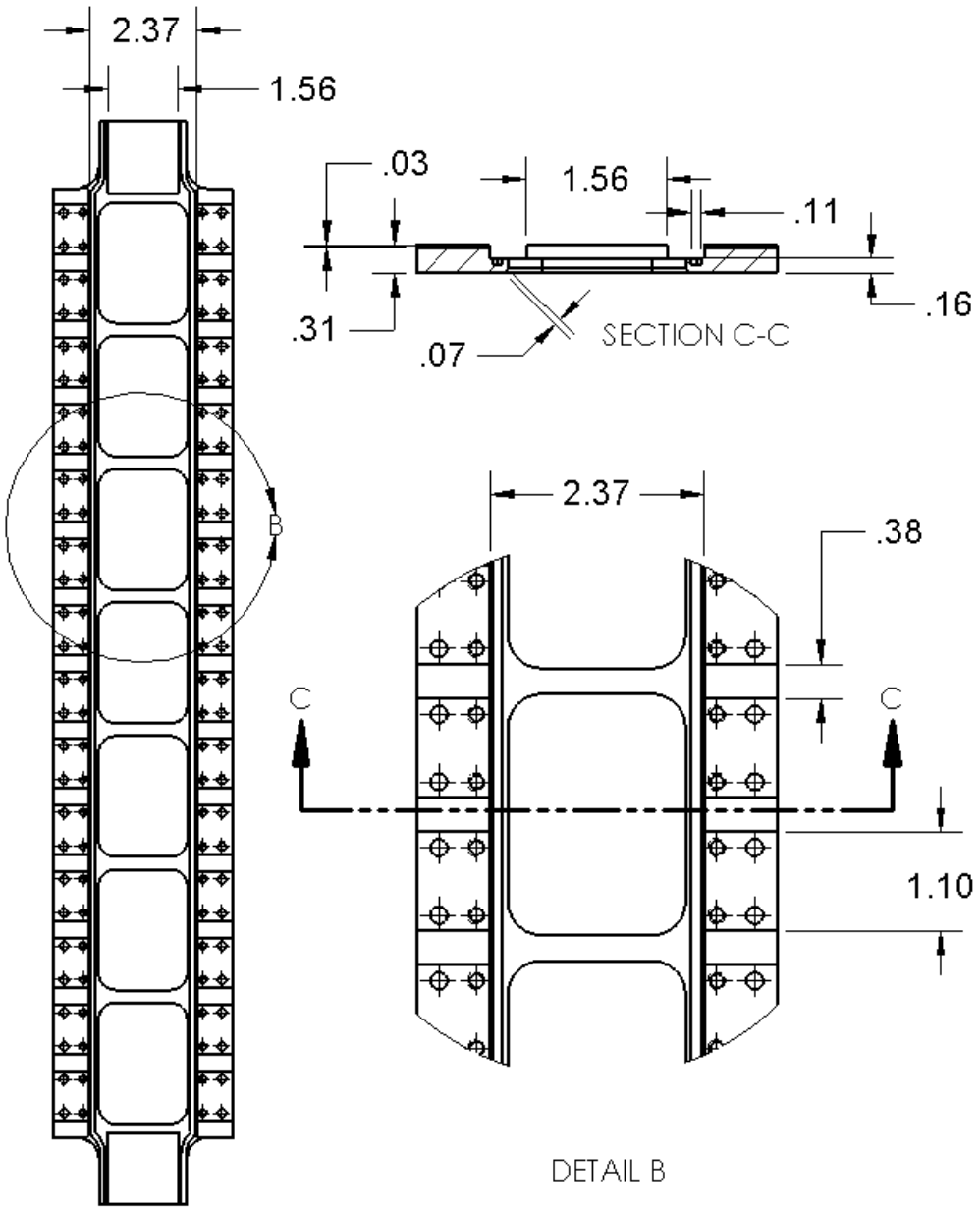
2.37
1.56
.03
1.56
.11
.16
.31
.07
SECTION C-C
B
2.37
.38
C
C
1.10
DETAIL B

2 - Window Flange

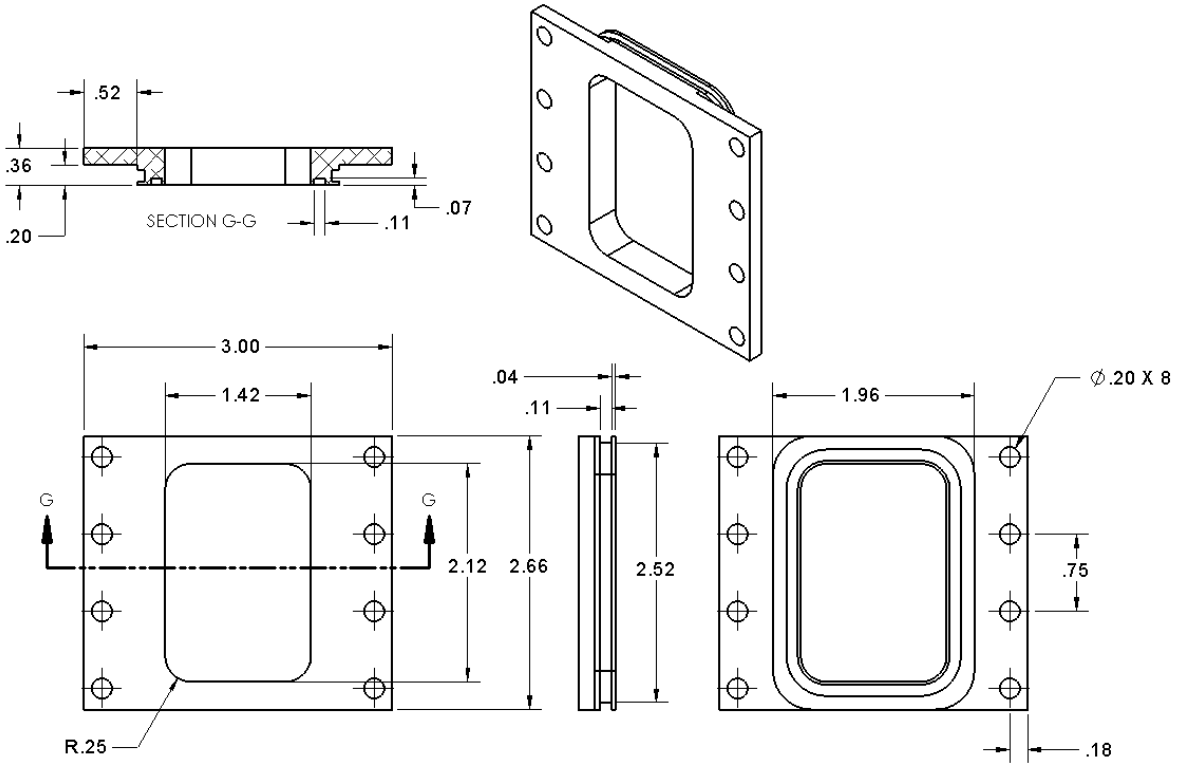

3 - ULTEM Side Piece

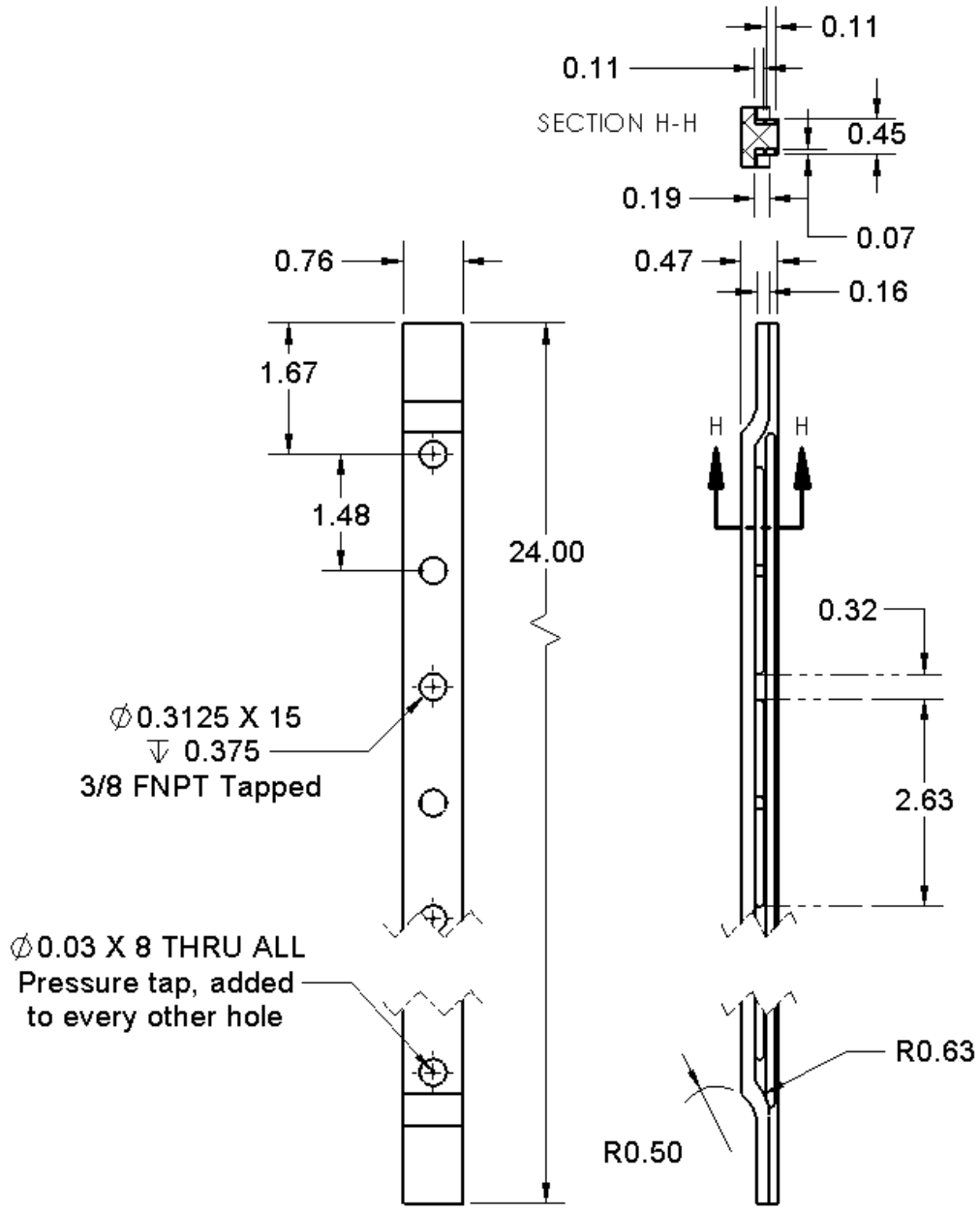

4 - Mounting Flange Block

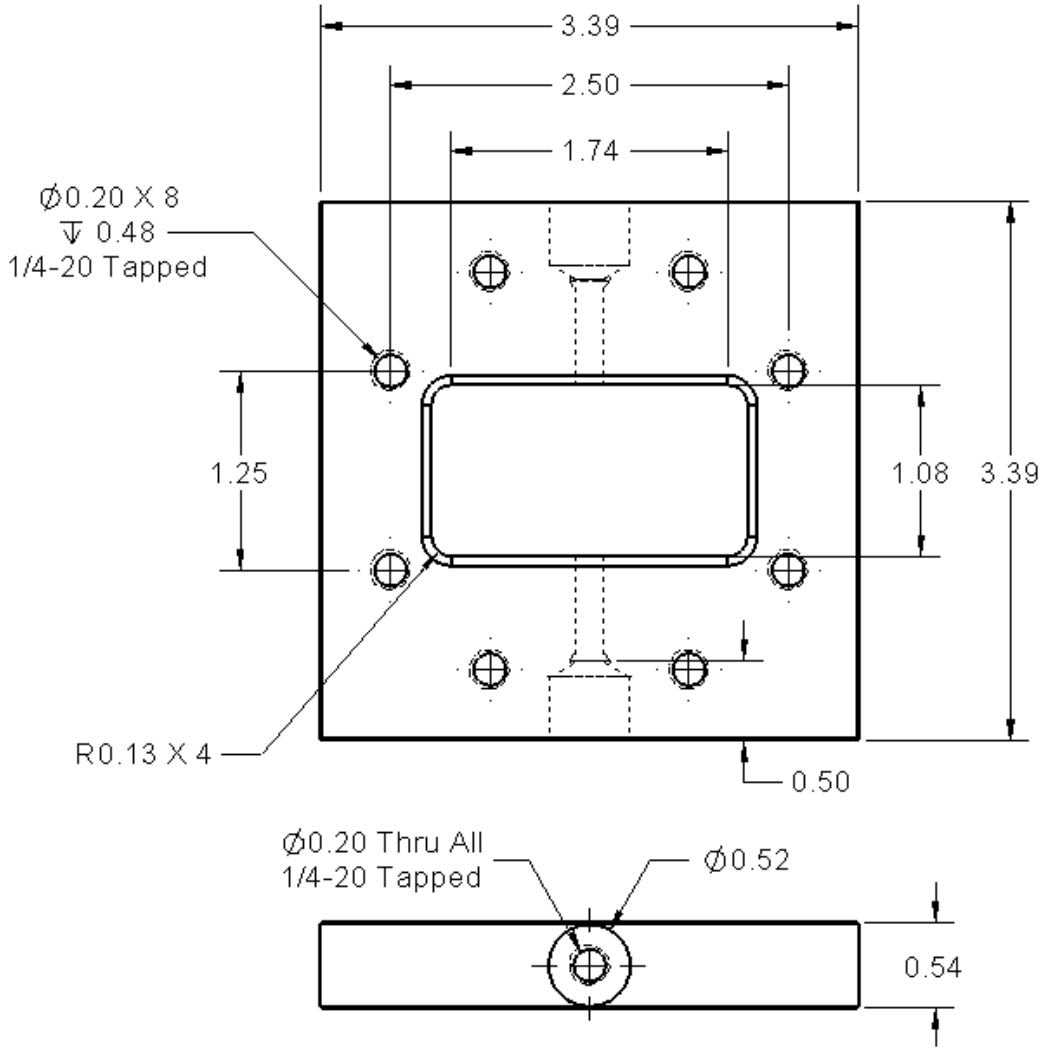

5 - Mounting Flange

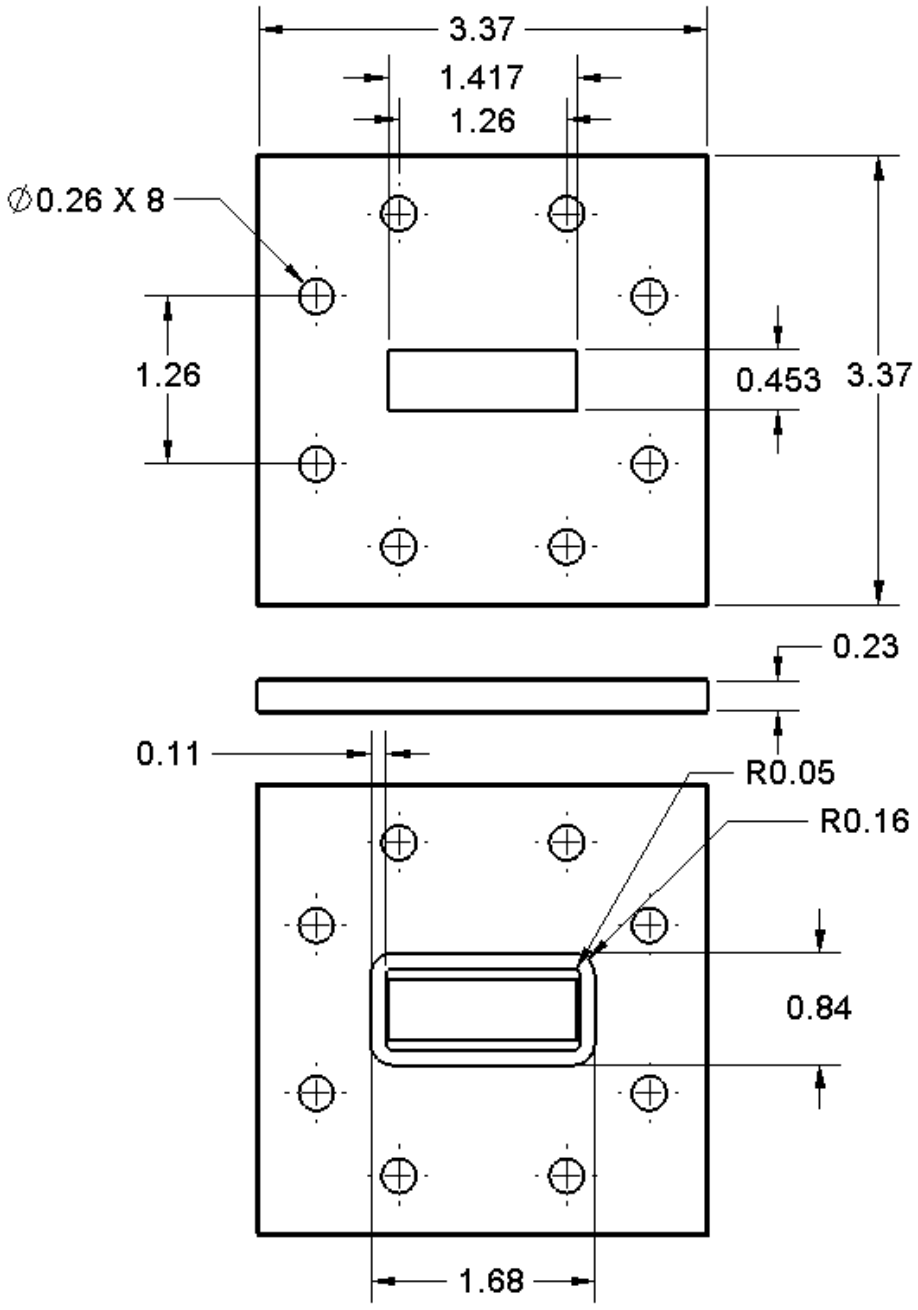

6 - Glass Window / 14 - Sensor Tap Fitting / 15 - Pressure Tap Tube / 17 - Window Wire Tap Tube

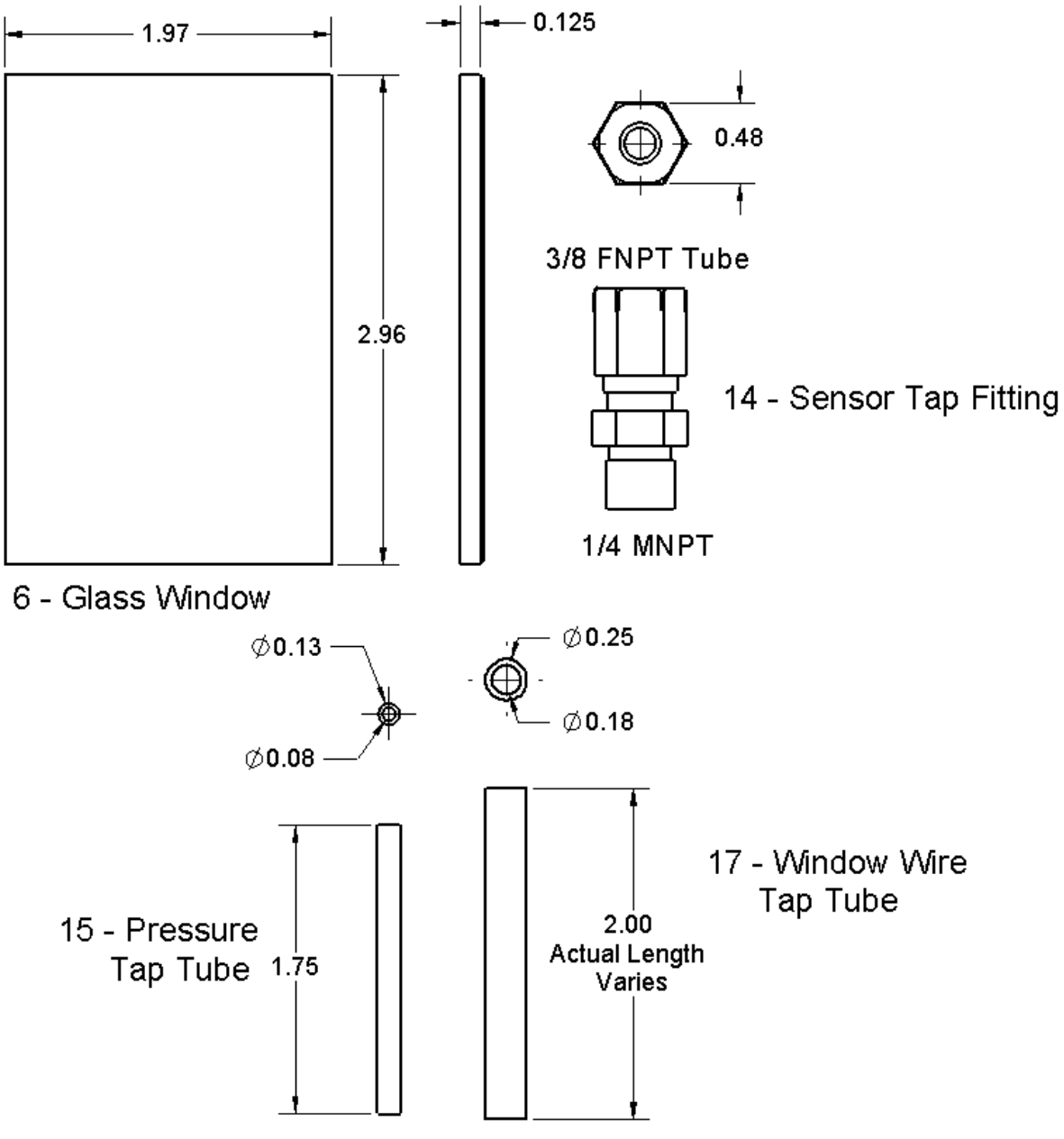

7.1.2 Pulse Generator

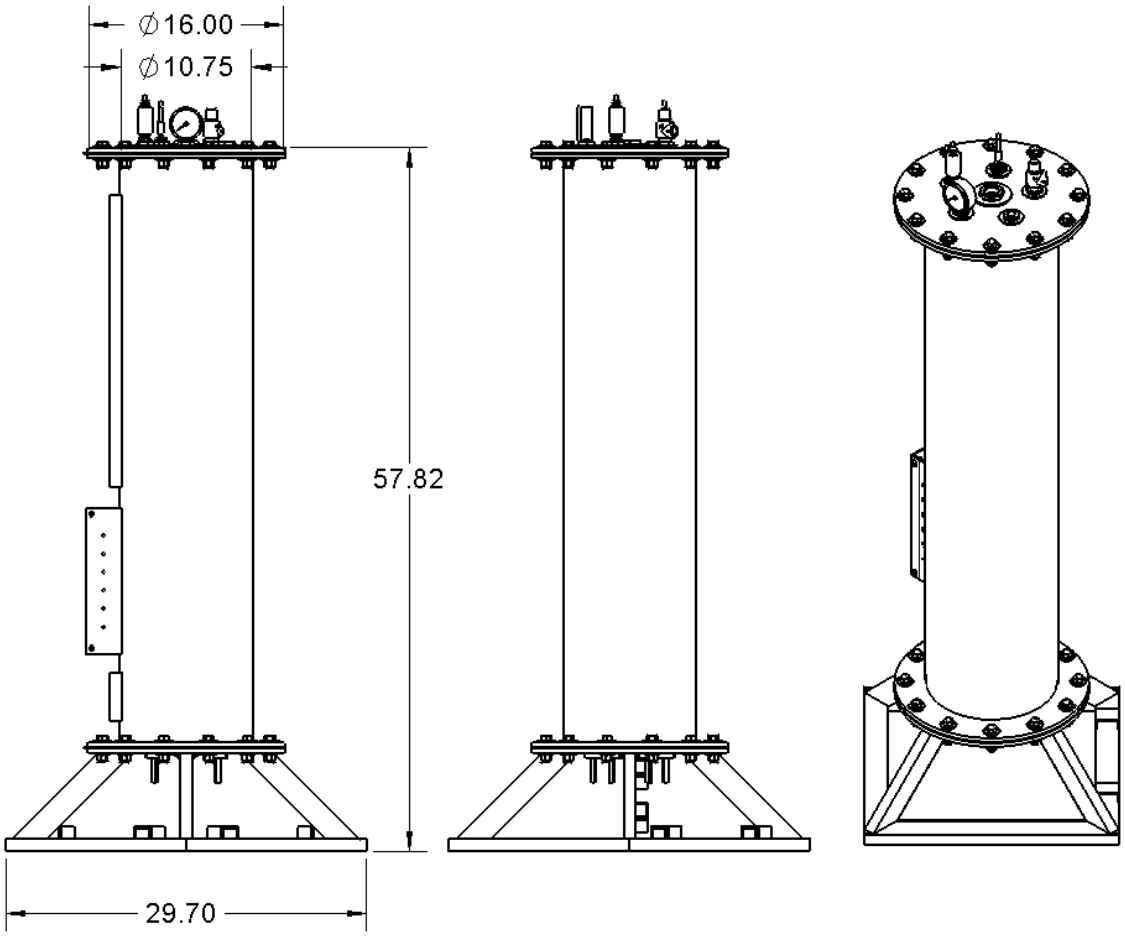

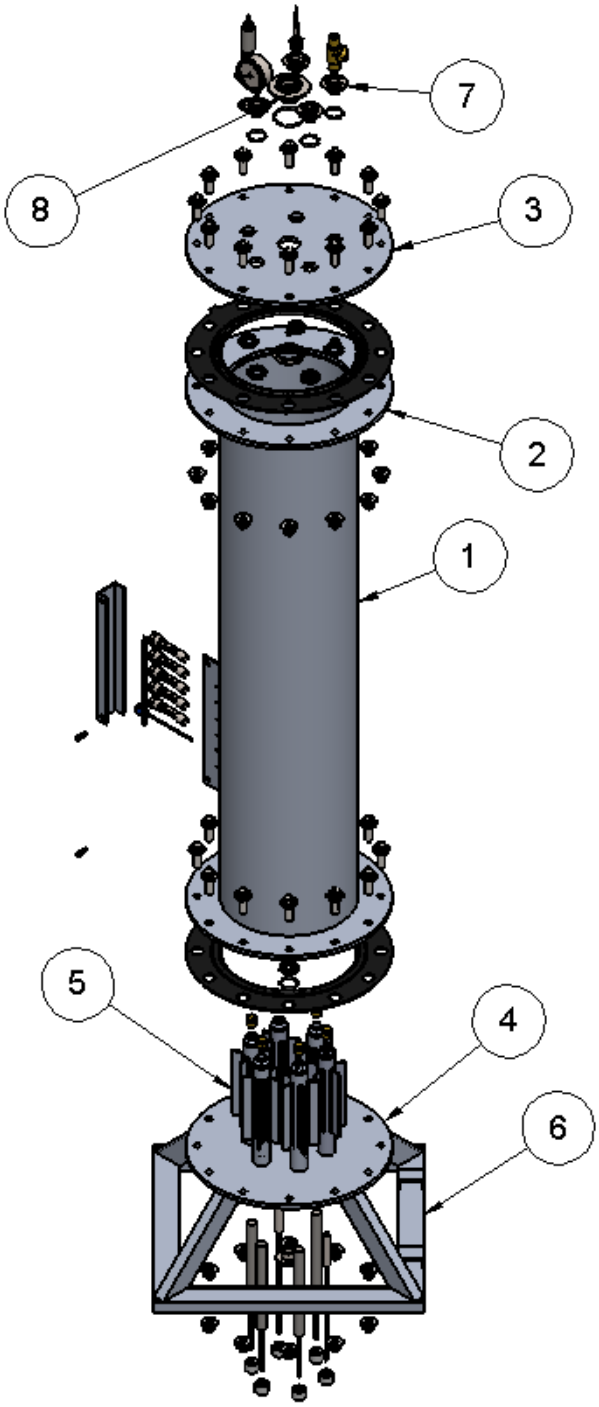
7
8
3
2
1
5
4
6

1 - Tank

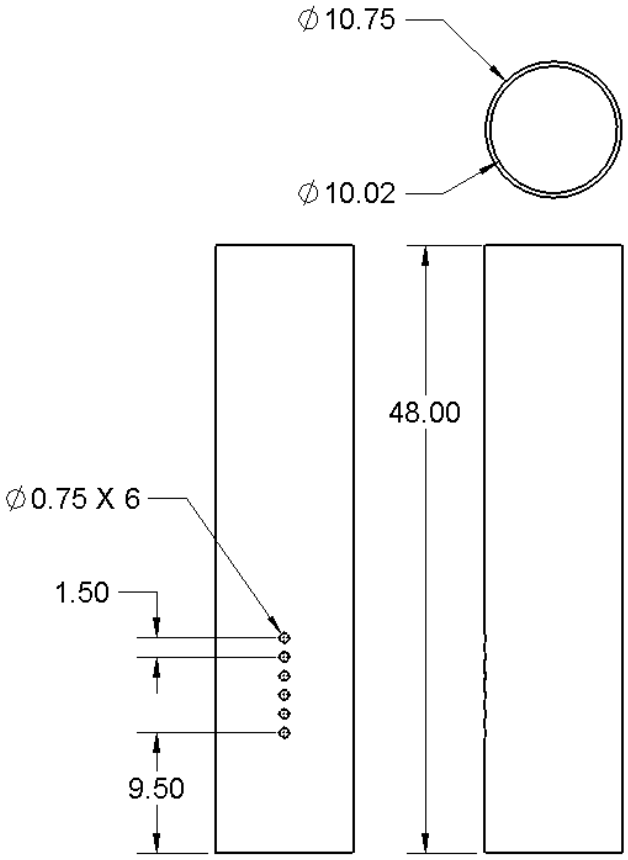

2 - Pipe Flange / 3 - Top Flange Plate / 4 - Bottom Flange Plate

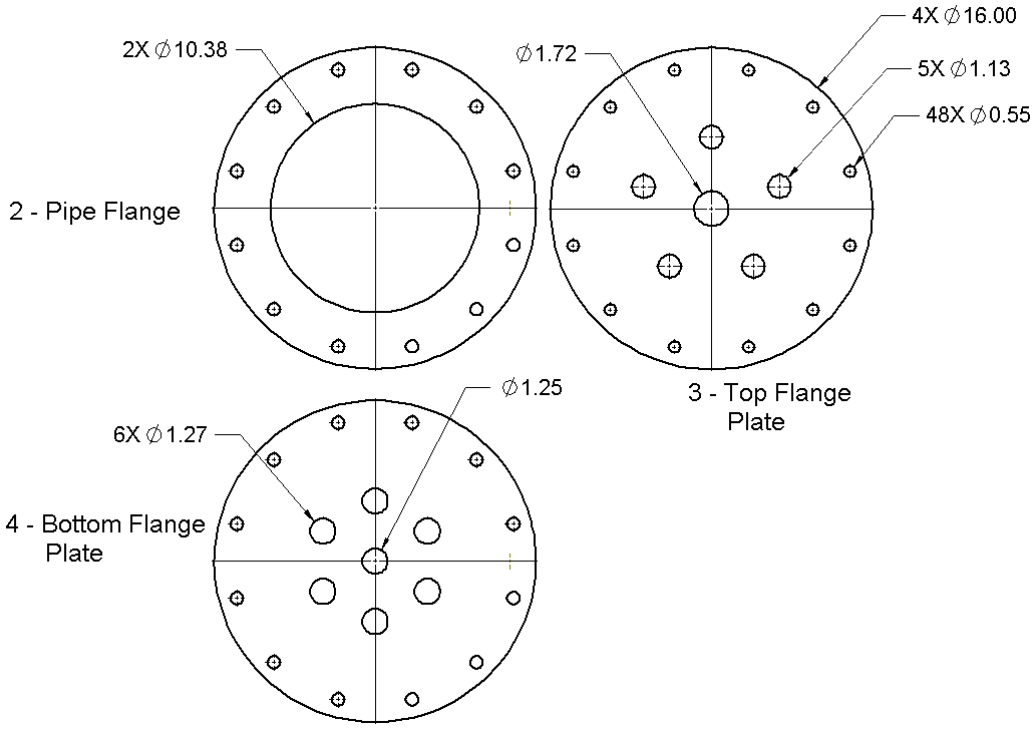

5 - Cartridge Heater Sleeve

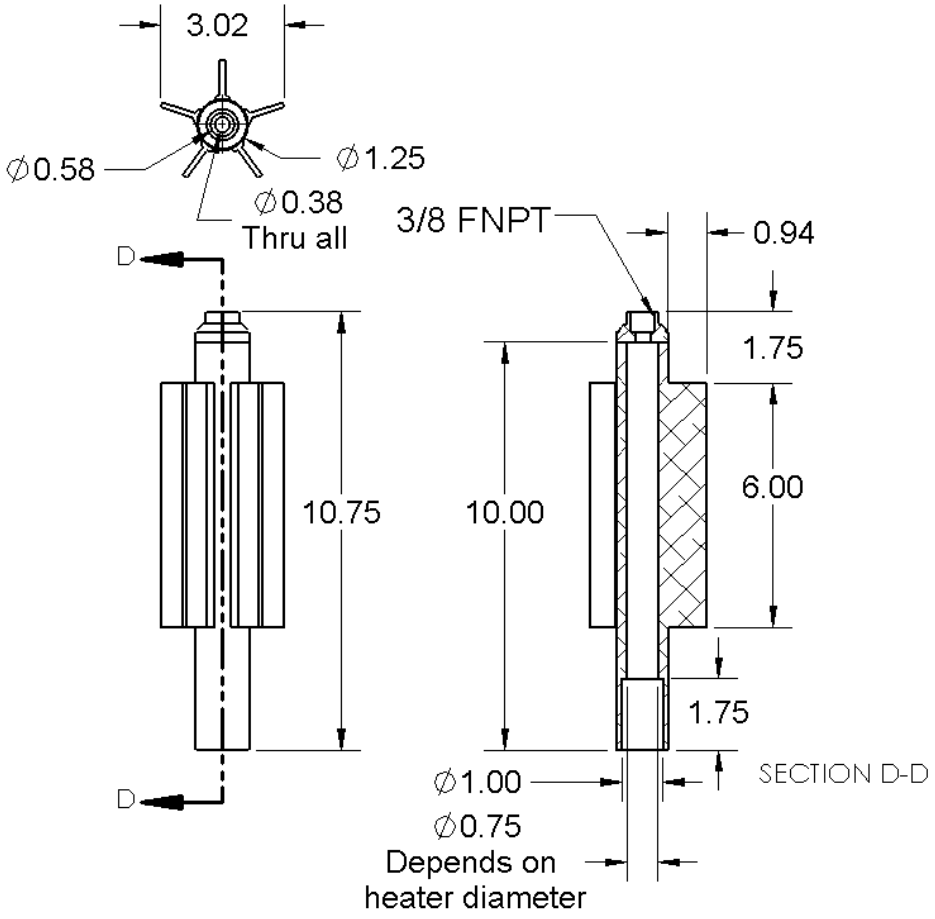

6 - Cartridge Sleeve Weldment

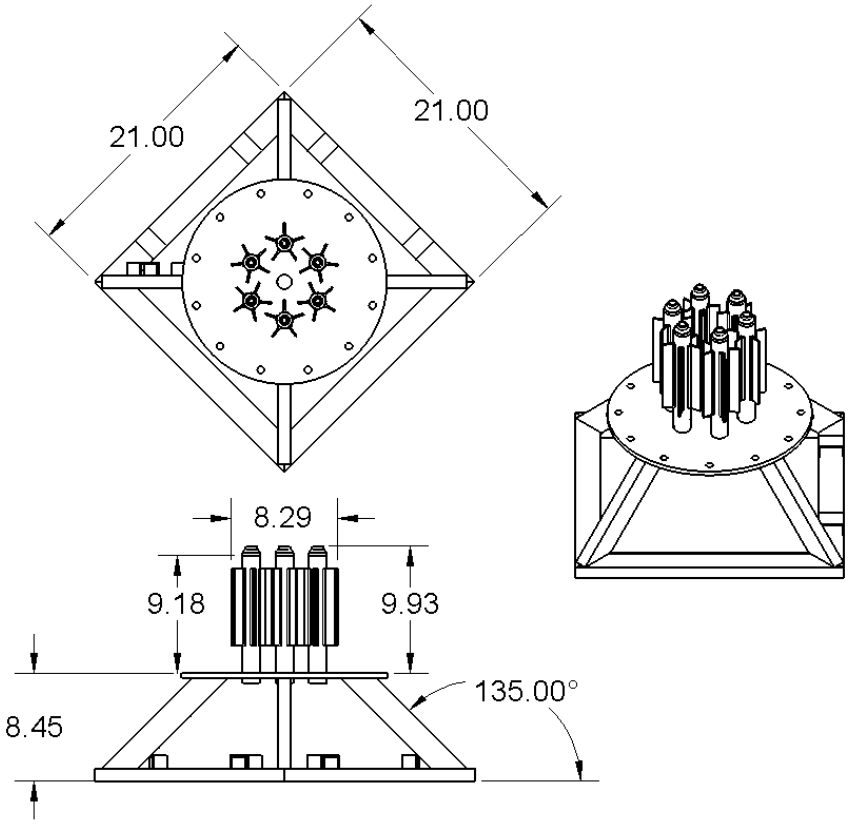

7.1.3 Development Section

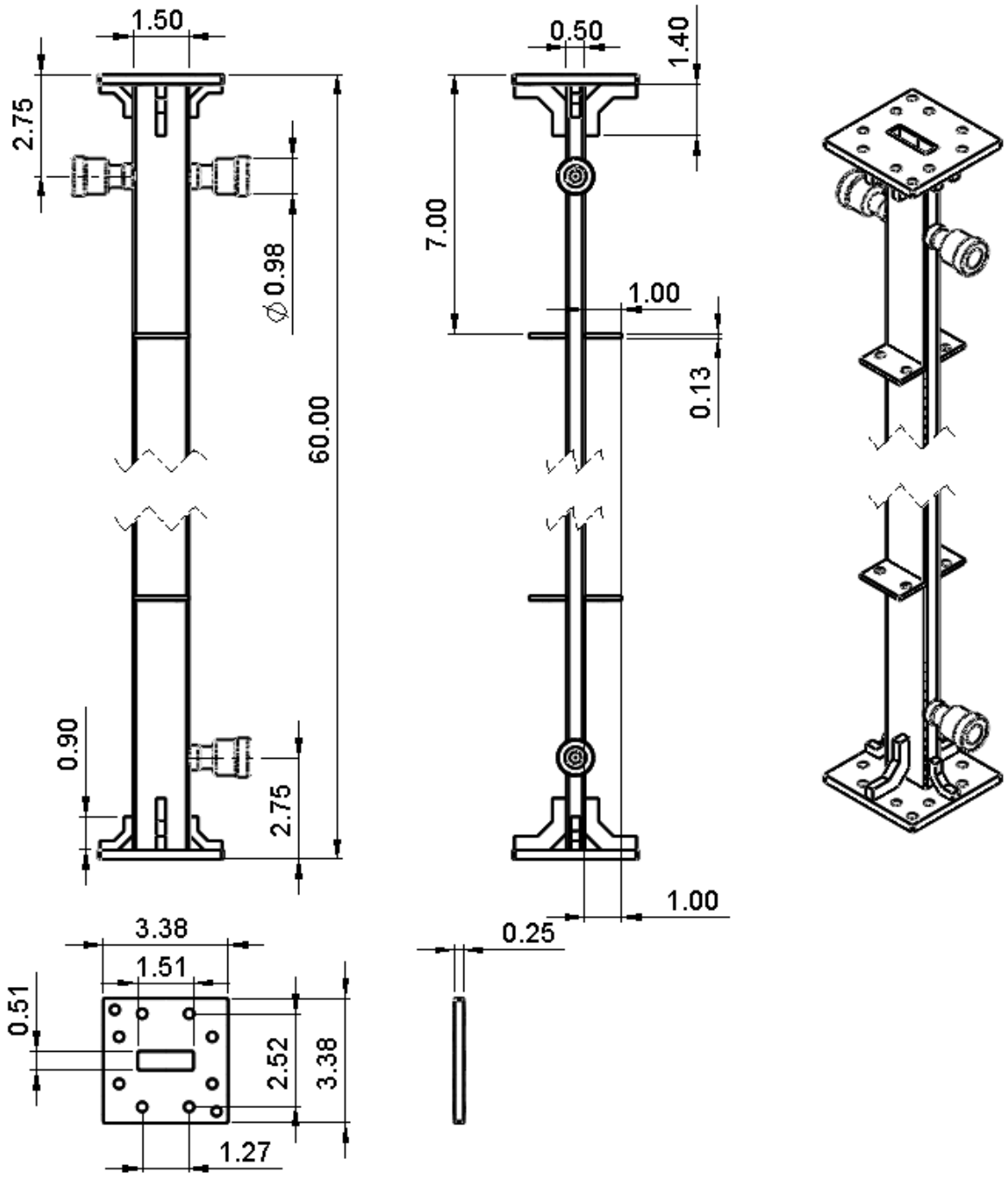

7.1.4 Test Section / Development Section Flow Converter

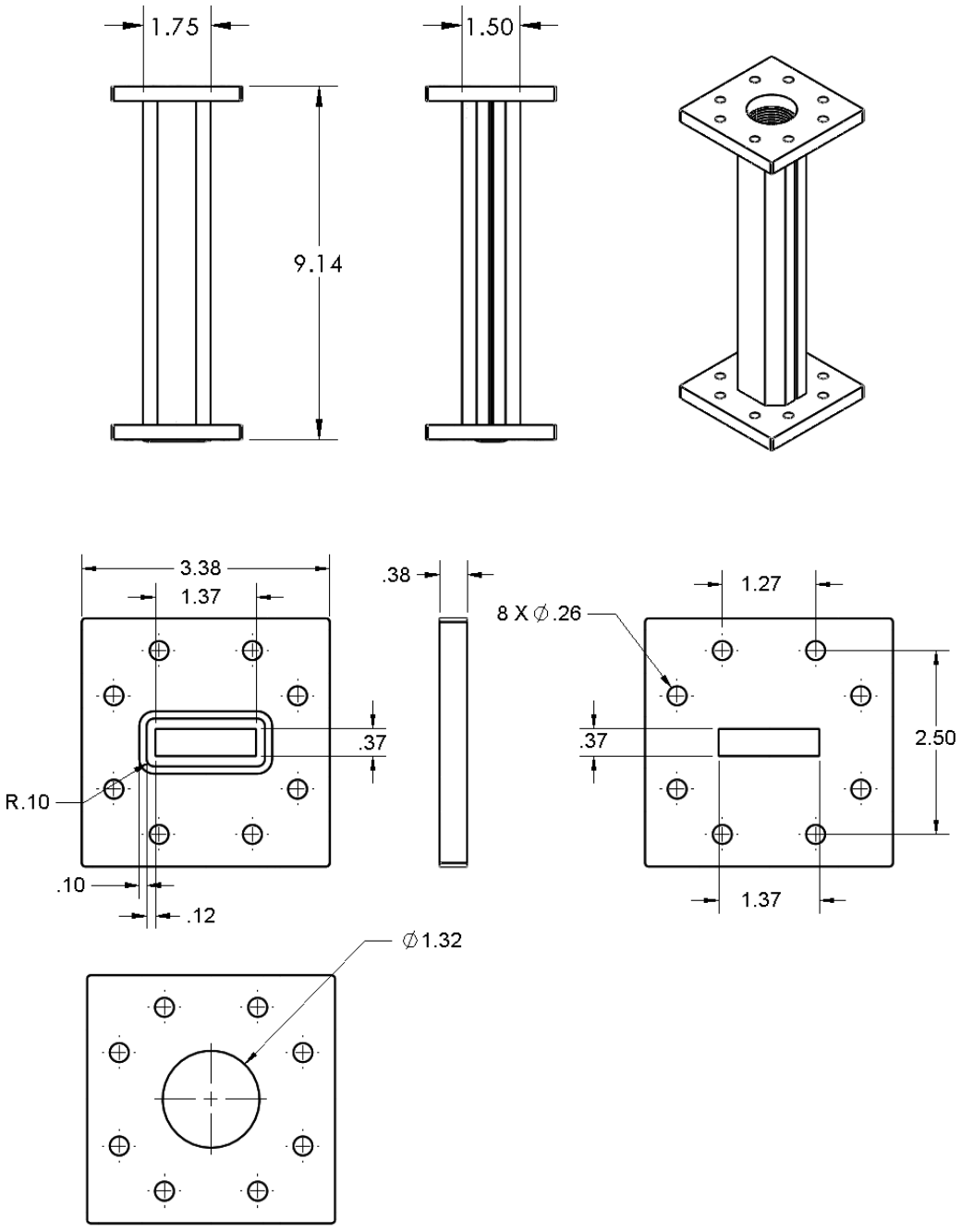

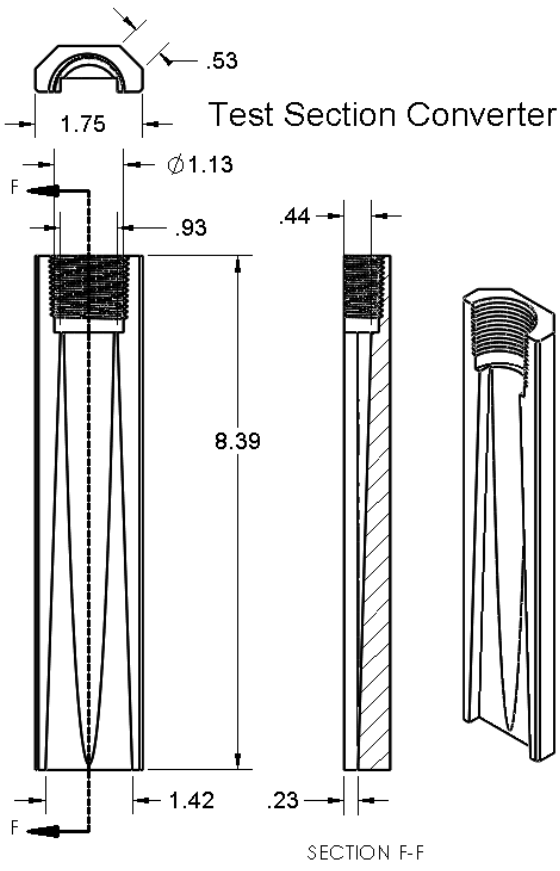
.53
1.75
Test Section Converter
∅1.13
F
.93
.44
8.39
1.42
.23
F
SECTION F-F

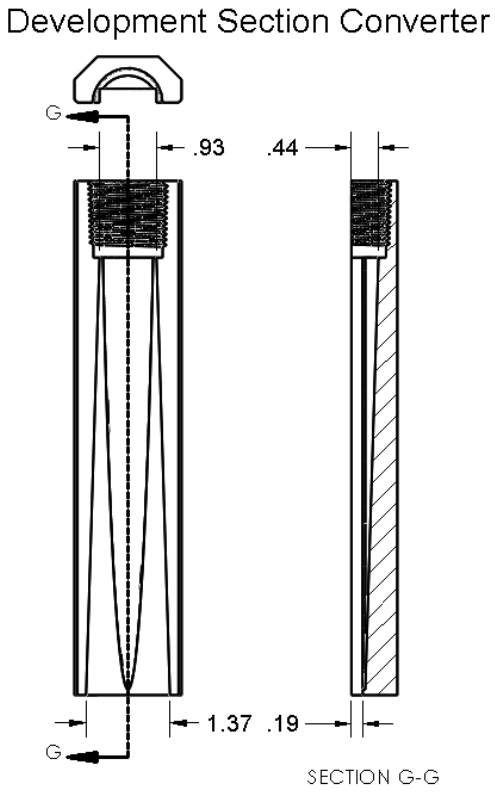
Development Section Converter
G
.93
.44
1.37
.19
G
SECTION G-G

7.1.5 Development to Test Section Converter

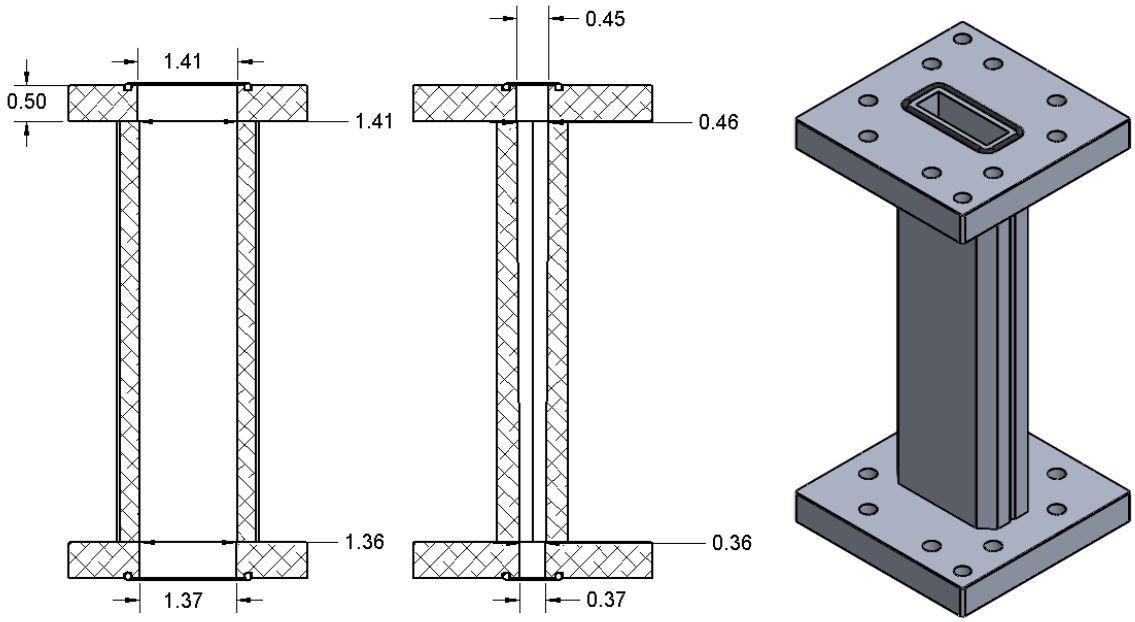

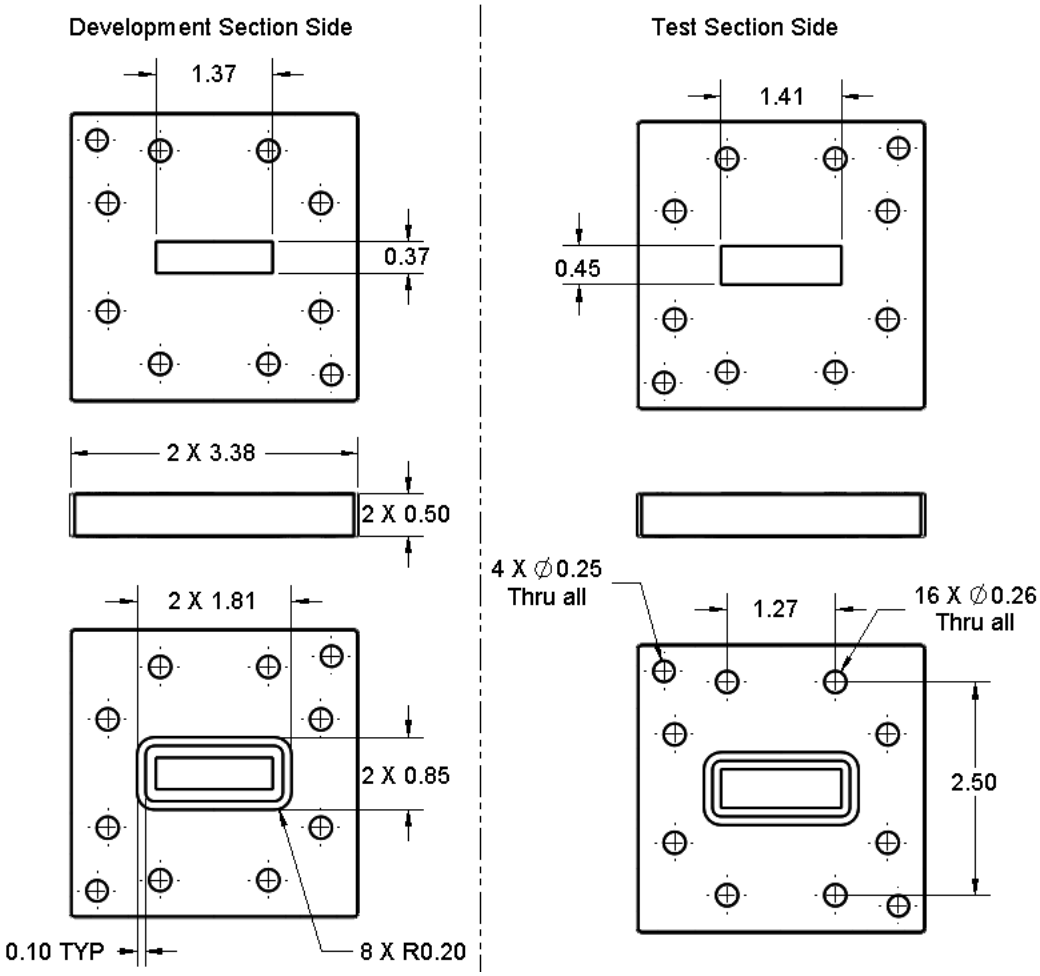
Development Section Side
1.37
0.37
2 X 3.38
2 X 0.50
2 X 1.81
2 X 0.85
0.10 TYP
8 X R0.20
Test Section Side
1.41
0.45
4 X ∅0.25
Thru all
1.27
16 X ∅0.26
Thru all
2.50

7.1.6 3D-Printed Prism Holder

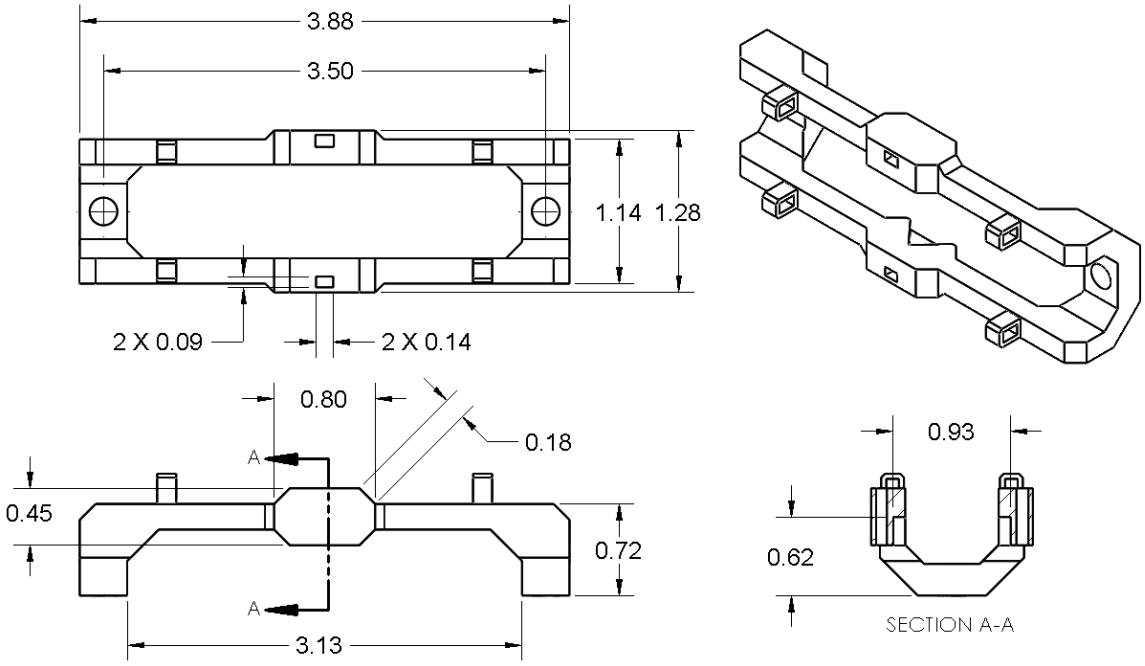

7.1.7 3D-Printed Double Laser Holder

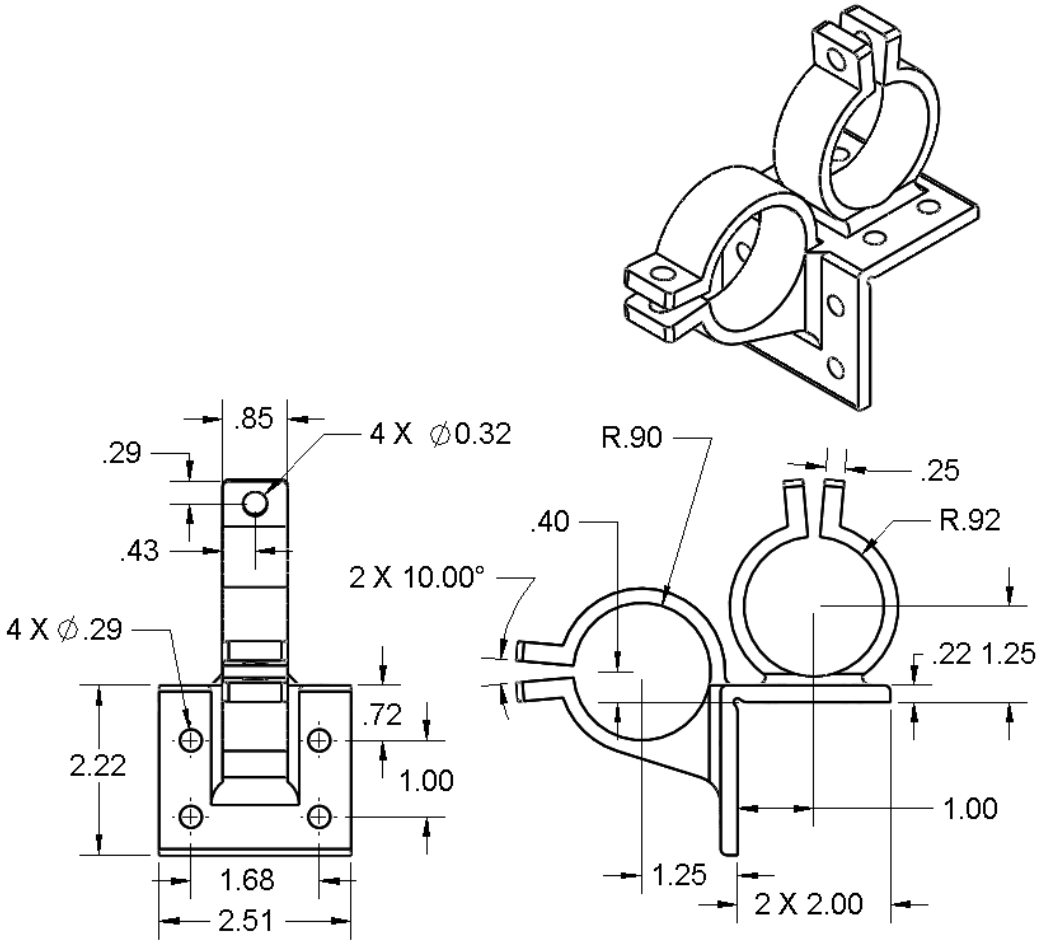

7.2 Pulse Generator

7.2.1 Thermodynamic Model EES Code

```
// MFVAL Pulse Generator Model Ultron          July 25th 2017

$UnitSystem K kPa J rad
$TabStops 0.25 2.5 4

// Set conditions //
//m_dot_pulse_gram = 16
m_dot_pulse = m_dot_pulse_gram*convert(g/s,kg/s)                    // Average mass flow from pulse generator, used to find initial required evaporization power

P_atm = 101.325
T_room = converttemp(C,K,22)

// Vapor at Outlet Properties //
T_vapor_outlet = 315
//P_vapor_outlet = 220
rho_vapor_outlet = density(R245fa,T=T_vapor_outlet,P=P_vapor_outlet)
h_vapor_outlet = enthalpy(R245fa,T=T_vapor_outlet,P=P_vapor_outlet)

// Liquid at Inlet Properties //
//T_liquid_inlet = 285
T_liquid_inlet = T_vapor_outlet - delta_T
P_liquid_inlet = 250
rho_liquid_inlet = density(R245fa,T=T_liquid_inlet,P=P_liquid_inlet)
h_liquid_inlet = enthalpy(R245fa,T=T_liquid_inlet,P=P_liquid_inlet)

// Saturation Conditions and Properties //
T_sat = t_sat(R245fa,P=P_vapor_outlet)
h_vap = enthalpy_vaporization(R245fa,T=T_sat-0.01[K])
h_sat_liquid = enthalpy(R245fa,T=T_sat-0.01[K],P=P_vapor_outlet)
h_sat_vapor = enthalpy(R245fa,T=T_sat+0.01[K],P=P_vapor_outlet)
rho_sat_liquid = density(R245fa,T=T_sat-0.01[K],P=P_vapor_outlet)
rho_sat_vapor = density(R245fa,T=T_sat+0.01[K],P=P_vapor_outlet)
m_sat_liquid = rho_sat_liquid*V_liquid
m_sat_vapor = rho_sat_vapor*V_vapor
m_sat_total = m_sat_liquid + m_sat_vapor
quality = m_sat_vapor/m_sat_liquid
```

```
// Pulse Generator Geometry //
id_tank = 10.02*convert(in,m)
ht_tank = 48*convert(in,m)

id_flange = 10.375*convert(in,m)
ht_flange = 0.375*convert(in,m)

id_gasket = 9.796875*convert(in,m)
ht_gasket = 0.078125*convert(in,m)

V_tank = ((pi*id_tank^2)/4)*ht_tank
V_flange = ((pi*id_flange^2)/4)*ht_flange
V_gasket = ((pi*id_gasket^2)/4)*ht_gasket
V_pg_total = V_tank + 2*V_flange + 2*V_gasket

// Cartridge Heater Geometry //
od_sleeve = 1.25*convert(in,m)
//ht_sleeve_inch = 8.875
ht_sleeve = ht_sleeve_inch*convert(in,m)
lg_fin = 6.5*convert(in,m)
wd_fin = 0.04*convert(in,m)
ht_fin = 0.5*convert(in,m)
n_sleeve = 6
n_fin = 5*n_sleeve

V_fin = wd_fin*ht_fin*lg_fin*n_fin
V_sleeve = ((pi*od_sleeve^2)/4)*ht_sleeve
V_pg_total2 = V_pg_total - V_fin - V_sleeve
```

```
// Liquid Refrigerant Fill //
//ht_liquid_inch = 16                                          // Height from bottom plate
ht_liquid = ht_liquid_inch*convert(in,m)
//ht_sensor_inch = 10
ht_sensor = ht_sensor_inch*convert(in,m)
//ht_betweenSensor = 2*convert(in,m)
ht_betweenSensor_inch = ht_betweenSensor*convert(m,in)
ht_sensor_inch[1] = ht_sensor*convert(m,in)
ht_sensor_inch[2] = ht_sensor_inch[1] + ht_betweenSensor_inch
ht_sensor_inch[3] = ht_sensor_inch[2] + ht_betweenSensor_inch
ht_sensor_inch[4] = ht_sensor_inch[3] + ht_betweenSensor_inch
ht_sensor_inch[5] = ht_sensor_inch[4] + ht_betweenSensor_inch

V_fill = ((pi*id_tank^2)/4)*(ht_liquid - ht_gasket - ht_flange) + V_flange + V_gasket
V_liquid = V_fill - V_sleeve
V_liquid_gal = V_liquid*convert(m^3,gal)
V_vapor = V_pg_total2 - V_liquid
V_vapor_gal = V_vapor*convert(m^3,gal)
V_liquid_safe = ((pi*id_tank^2)/4)*(ht_liquid - ht_sleeve)
V_sensor_safe = ((pi*id_tank^2)/4)*(ht_sensor - ht_sleeve)
V_betweenSensor = ((pi*id_tank^2)/4)*(ht_betweenSensor)

rho_tank_liquid = density(R245fa,T=305[K],P=220[kPa])
m_sensor_safe = rho_tank_liquid*V_sensor_safe
m_liquid_safe = rho_tank_liquid*V_liquid_safe
t_sensor_safe = (m_sensor_safe/m_dot_pulse)*convert(s,min)
t_liquid_safe = (m_liquid_safe/m_dot_pulse)*convert(s,min)

m_betweenSensor = rho_tank_liquid*V_betweenSensor
t_betweenSensor = (m_betweenSensor/m_dot_pulse)*convert(s,min)

// Vapor Generation Heat Transfer Analysis //
h_vap2 = h_sat_vapor - h_sat_liquid

Power_vap = h_vap*m_dot_pulse
//Power_in = (h_vapor_outlet - h_liquid_inlet)*m_dot_pulse
//Power_in = 3900
Power_heat = ((h_sat_liquid - h_liquid_inlet) + h_vap )*m_dot_pulse

t_heatup =  (((h_vapor_outlet - h_liquid_inlet)*((pi*id_tank^2)/4)*(ht_liquid)*rho_liquid_inlet)/Power_in)*convert(s,min)

// Pressure Loss Per Pulse //
h_beforePulse = Enthalpy(R245fa,x=quality,P=P_vapor_outlet)
vspec_beforePulse = V_vapor/(m_sat_vapor)

quality2 = (m_sat_vapor-m_dot_pulse*1[sec])/m_sat_liquid
h_afterPulse = Enthalpy(R245fa,x=quality2,T=T_sat)
vspec_afterPulse = V_vapor/(m_sat_vapor - m_dot_pulse*1[sec])

P_beforePulse = Pressure(R245fa,T=T_sat,v=vspec_beforePulse)
P_afterPulse = Pressure(R245fa,T=T_sat,v=vspec_afterPulse)
P_loss = 10*(P_beforePulse - P_afterPulse)
```

7.2.2 Critical Heat Flux EES Code

```
// MFVAL Pulse Generator Required Heater Power                    October 2018

$UnitSystem K kPa J rad
$TabStops 0.25 2.5 4

// Set conditions //
//m_dot_pulse_gram = 16
m_dot_pulse = m_dot_pulse_gram*convert(g/s,kg/s)                  // Average mass flow from pulse generator, used to find initial required evaporization power

h = 9*convert(in,m)

r_50 = (0.5/2)*convert(in,m)
r_75 = (0.75/2)*convert(in,m)
r_125 = (1.25/2)*convert(in,m)

SA_50 = 2*pi*r_50*h + 2*pi*r_50^2
SA_75 = 2*pi*r_75*h + 2*pi*r_75^2
SA_125 = 2*pi*r_125*h + 2*pi*r_125^2

q_50 = Critical_Heat_Flux('R245fa','Cylinder', r_50, T_sat)*SA_50
q_75 = Critical_Heat_Flux('R245fa','Cylinder', r_75, T_sat)*SA_75
q_125 = Critical_Heat_Flux('R245fa','Cylinder', r_125, T_sat)*SA_125

q_50_in = (q_50/SA_50)*convert(W/m^2,W/in^2)
q_75_in = (q_75/SA_75)*convert(W/m^2,W/in^2)
q_125_in = (q_125/SA_125)*convert(W/m^2,W/in^2)

P_atm = 101.325
T_room = converttemp(C,K,22)

// Vapor at Outlet Properties //
T_vapor_outlet = 315
P_vapor_outlet = 220
rho_vapor_outlet = density(R245fa,T=T_vapor_outlet,P=P_vapor_outlet)
h_vapor_outlet = enthalpy(R245fa,T=T_vapor_outlet,P=P_vapor_outlet)

// Liquid at Inlet Properties //
T_liquid_inlet = 285
T_liquid_inlet = T_vapor_outlet - delta_T
P_liquid_inlet = 250
rho_liquid_inlet = density(R245fa,T=T_liquid_inlet,P=P_liquid_inlet)
h_liquid_inlet = enthalpy(R245fa,T=T_liquid_inlet,P=P_liquid_inlet)

// Saturation Conditions and Properties //
T_sat = t_sat(R245fa,P=P_vapor_outlet)
h_vap = enthalpy_vaporization(R245fa,T=T_sat-0.01[K])
h_sat_liquid = enthalpy(R245fa,T=T_sat-0.01[K],P=P_vapor_outlet)
h_sat_vapor = enthalpy(R245fa,T=T_sat+0.01[K],P=P_vapor_outlet)
rho_sat_liquid = density(R245fa,T=T_sat-0.01[K],P=P_vapor_outlet)
rho_sat_vapor = density(R245fa,T=T_sat+0.01[K],P=P_vapor_outlet)

Q_dot_in = ((h_sat_liquid - h_liquid_inlet) + h_vap )*m_dot_pulse

$Export 'F:\Box Sync\Annular Flow\Fehring\PG Thermal\Data\CriticalHeatFlux.csv' m_dot_pulse_gram Q_dot_in q_50 q_75 q_125
```

7.2.3 Cartridge Heater Geometry MATLAB Code

```
function [x,y]=CHModelGeometry2(bs,s)

%%%%%%%%%%%%%%%%%%%%%%%%%%%%%
% Input parameters
th = 0.00635;
Lch = 0.2032;
Lsl = 0.254;

L1 = 0.009525;              % Plate thickness
L2 = 0.143656;              % Plate length
L5 = 0.01143;               % Bottom of sleeve distance to plate
L3 = Lsl - L1 - L5;
L4 = 0.03175;
L6 = Lsl - Lch - th;
L7 = 0.0188595;
L8 = Lch - 2*L7;
L9 = L4 - 2*th;

L10 = 0.254;
L11 = 2*L2 + L4;
L12 = 0.009525;

%%%%%%%%%%%%%%%%%%%%%%%%%%%%%

%%%%%%%%%%%%%%%%%%%%%%%%%%%%%
nbs=26;  %number of boundary segments
%%%%%%%%%%%%%%%%%%%%%%%%%%%%%

if nargin==0,
  x=nbs; % number of boundary segments
  return
end

%%%%%%%%%%%%%%%%%%%%%%%%%%%%%%%%%%
% parameterized boundaries
d=[
  0 0 0 0 0 0 0 0 0 0 0 0 0 0 0 0 0 0 0 0 0 0 0 0 0 0 0 0 % start parameter value
  1 1 1 1 1 1 1 1 1 1 1 1 1 1 1 1 1 1 1 1 1 1 1 1 1 1 1 1 % end parameter value
  0 3 3 3 3 3 0 0 0 0 0 2 2 2 2 2 2 2 0 0 0 0 2 0 0 0 0 % left hand region
  1 1 1 1 1 1 1 1 1 1 1 1 1 1 1 1 1 1 1 1 1 1 1 0 3 3 3 % right hand region
];
%%%%%%%%%%%%%%%%%%%%%%%%%%%%%%%%%%

```

```
bs1=bs(:)';

if find(bs1<1 | bs1>nbs),
  error('PDE:rectangle:InvalidBs', 'Non existent boundary segment number.')
end

if nargin==1,
  x=d(:,bs1);
  return
end

x=zeros(size(s));
y=zeros(size(s));
[m,n]=size(bs);
if m==1 && n==1,
  bs=bs*ones(size(s)); % expand bs
elseif m~=size(s,1) || n~=size(s,2),
  error('PDE:rectangle:SizeBs', 'bs must be scalar or of same size as s.');
end

if ~isempty(s),
%%%%%%%%%%%%%%%%%%%%%%%%%%%%%%%%
%boundary segment coordinates
    % boundary segment 1
    ii=find(bs==1);
    if length(ii)
        x(ii)=0;
        y(ii)=s(ii)*L1;
    end

    % boundary segment 2
    ii=find(bs==2);
    if length(ii)
        x(ii)=s(ii)*L2;
        y(ii)=L1;
    end

    % boundary segment 3
    ii=find(bs==3);
    if length(ii)
        x(ii)=L2;
        y(ii)=s(ii)*L3 + L1;
    end
```

```
    end

    % boundary segment 4
    ii=find(bs==4);
    if length(ii)
        x(ii)=s(ii)*L4 + L2;
        y(ii)=L1 + L3;
    end

    % boundary segment 5
    ii=find(bs==5);
    if length(ii)
        x(ii)=L2 + L4;
        y(ii)=(1-s(ii))*L3 + L1;
    end

    % boundary segment 6
    ii=find(bs==6);
    if length(ii)
        x(ii)=s(ii)*L2 + L4 + L2;
        y(ii)=L1;
    end

    % boundary segment 7
    ii=find(bs==7);
    if length(ii)
        x(ii)=2*L2 + L4;
        y(ii)=(1-s(ii))*L1;
    end

    % boundary segment 8
    ii=find(bs==8);
    if length(ii)
        x(ii)=(1-s(ii))*L2 + L2 + L4;
        y(ii)=0;
    end

    % boundary segment 9
    ii=find(bs==9);
    if length(ii)
        x(ii)=L2 + L4;
        y(ii)=-s(ii)*L5;
    end
```

```
129
130         % boundary segment 10
131 -       ii=find(bs==10);
132 -       if length(ii)
133 -           x(ii)=(1-s(ii))*th + L2 + (L4 - th);
134 -           y(ii)=-L5;
135 -       end
136
137         % boundary segment 11
138 -       ii=find(bs==11);
139 -       if length(ii)
140 -           x(ii)=L2 + (L4 - th);
141 -           y(ii)=s(ii)*L6 - L5;
142 -       end
143
144         % boundary segment 12
145 -       ii=find(bs==12);
146 -       if length(ii)
147 -           x(ii)=L2 + (L4 - th);
148 -           y(ii)=s(ii)*L7 + L6 - L5;
149 -       end
150
151         % boundary segment 13
152 -       ii=find(bs==13);
153 -       if length(ii)
154 -           x(ii)=L2 + (L4 - th);
155 -           y(ii)=s(ii)*L8 + L7 + L6 - L5;
156 -       end
157
158         % boundary segment 14
159 -       ii=find(bs==14);
160 -       if length(ii)
161 -           x(ii)=L2 + (L4 - th);
162 -           y(ii)=s(ii)*L7 + L8 + L7 + L6 - L5;
163 -       end
164
165         % boundary segment 15
166 -       ii=find(bs==15);
167 -       if length(ii)
168 -           x(ii)=(1-s(ii))*L9 + L2 + th;
169 -           y(ii)=2*L7 + L8 + L6 - L5;
170 -       end
171
```

```
172         % boundary segment 16
173 -       ii=find(bs==16);
174 -       if length(ii)
175 -           x(ii)=L2 + th;
176 -           y(ii)=(1-s(ii))*L7 + L8 + L7 + L6 - L5;
177 -       end
178
179         % boundary segment 17
180 -       ii=find(bs==17);
181 -       if length(ii)
182 -           x(ii)=L2 + th;
183 -           y(ii)=(1-s(ii))*L8 + L7 + L6 - L5;
184 -       end
185
186         % boundary segment 18
187 -       ii=find(bs==18);
188 -       if length(ii)
189 -           x(ii)=L2 + th;
190 -           y(ii)=(1-s(ii))*L7 + L6 - L5;
191 -       end
192
193         % boundary segment 19
194 -       ii=find(bs==19);
195 -       if length(ii)
196 -           x(ii)=L2 + th;
197 -           y(ii)=(1-s(ii))*L6 - L5;
198 -       end
199
200         % boundary segment 20
201 -       ii=find(bs==20);
202 -       if length(ii)
203 -           x(ii)=(1-s(ii))*th + L2;
204 -           y(ii)=-L5;
205 -       end
206
207         % boundary segment 21
208 -       ii=find(bs==21);
209 -       if length(ii)
210 -           x(ii)=L2;
211 -           y(ii)=-(1-s(ii))*L5;
212 -       end
213
214         % boundary segment 22
```

```
215 -       ii=find(bs==22);
216 -       if length(ii)
217 -           x(ii)=(1-s(ii))*L2;
218 -           y(ii)=0;
219 -       end
220
221         % boundary segment 23
222 -       ii=find(bs==23);
223 -       if length(ii)
224 -           x(ii)=s(ii)*L9 + L2 + th;
225 -           y(ii)=L6 - L5;
226 -       end
227
228         % boundary segment 24
229 -       ii=find(bs==24);
230 -       if length(ii)
231 -           x(ii)=0;
232 -           y(ii)=s(ii)*L10 + L1;
233 -       end
234
235         % boundary segment 25
236 -       ii=find(bs==25);
237 -       if length(ii)
238 -           x(ii)=s(ii)*L11;
239 -           y(ii)=L10 + L1;
240 -       end
241
242         % boundary segment 26
243 -       ii=find(bs==26);
244 -       if length(ii)
245 -           x(ii)=L11;
246 -           y(ii)=(1-s(ii))*L10 + L1;
247 -       end
248
249     %%%%%%%%%%%%%%%%%%%%%%%%%%%%%%%
250 -   end
```

7.2.4 Cartridge Heater Finite Element Analysis MATLAB Code

```
%% Pulse Generator Model
% Brian Fehring
% 2017-5-26

close all
clear all
clc
tic;
set(0,'DefaultAxesPosition',[0.125 0.15 0.85 0.825])

% Geometry Parameters

th = 0.00635;
Lch = 0.2032;
Lsl = 0.254;

L1 = 0.009525;              % Plate thickness
L2 = 0.143656;              % Plate length
L5 = 0.01143;               % Bottom of sleeve distance to plate
L3 = Lsl - L1 - L5;
L4 = 0.03175;
L6 = Lsl - Lch - th;
L7 = 0.0188595;
L8 = Lch - 2*L7;
L9 = L4 - 2*th;

L10 = 0.3556; %0.254;
L11 = 2*L2 + L4;
L12 = 0.009525;

Ach = (pi*L9^2)/4 + pi*L9*(Lch-2*L7);

fig1 = figure(1);
pdegplot('CHModelGeometry2'),axis([-0.075 0.2 -0.025 0.3])
[p, e, t] = initmesh('CHModelGeometry2','hmax',0.1);
[p, e, t] = refinemesh('CHModelGeometry2', p, e, t);
[p, e, t] = refinemesh('CHModelGeometry2', p, e, t);
pdemesh(p, e, t), axis equal
xlabel('X-Distance [m]','Fontsize',12);
ylabel('Y-Distance [m]','Fontsize',12);
```

```
41 -    disp('PDE Plot and Mesh')
42 -    toc
43
44 -    [Data,label] = xlsread('FinData.xlsx');
45 -    Tvertcyl = Data(:,1);
46 -    hvertcyl = Data(:,2);
47 -    Tflatplt = Data(:,3);
48 -    hflatplt = Data(:,4);
49
50      % Boundary Conditions - Temperatures and Boundary Resistances
51 -    T_amb = 295;                % External (MFVAL room) temperature
52 -    Tedge = 315;                % Saturation temperature associated with 220 kPa
53 -    hch = 90594/400;            % Nucleate boiling R245fa on cartridge heater surfaces
54 -    hplate = 35;               % Free convection R245fa-aluminum plate (horiz)
55      %hplate = 41800/360;         % Nucleate boiling R245fa on aluminum plate
56 -    hc = 0.01;                  % Rc between cartridge heater and aluminum sleeve
57 -    hconv = 1.5;                % Free convection air-aluminum plate
58 -    hset = 99999;               % Set temperature of R245fa outside box boundaries
59
60 -    Powerch = 1000;             % Cartridge heater power (total)
61 -    gch = 0;                    % Cartridge heater power generation
62 -    qch = Powerch/Ach;          % Cartridge heater power surface heat flux
63      %qch = 0;
64
65 -    kal = 156.3;                % Conductivity of aluminum
66 -    kinc = 9.793;               % Conductivity of incoloy
67 -    kR245fa = 8.706;           % Conductivity of liquid R24fa
68
69 -    rhoal = 2699;               % Density of aluminum
70 -    rhoinc = 8191;              % Density of incoloy
71 -    rho245fa = 1334;            % Density of liquid R245fa
72
73 -    cpal = 953.9;               % Specific heat of aluminum
74 -    cpinc = 450;                % Specific heat of incoloy
75 -    cpR24fa = 1326;             % Specific heat of liquid R245fa
76
77 -    N = length(p);              % Number of nodes
78 -    NE = length(t);             % Number of edges
79 -    NB = length(e);             % Number of boundaries
80
```

```
pm = p;
tm = t;
em = zeros(3,NB);
em(1,:) = e(1,:);
em(2,:) = e(2,:);
em(3,:) = e(5,:);

C=spalloc(N,N,7*N);          % Capacitance matrix
K=spalloc(N,N,7*N);          % Conductance matrix
g=zeros(N,1);                % Cartridge heater heat generation

sdm = [kal, rhoal, cpal, 0; kinc, rhoinc, cpinc, gch; kR245fa, rho245fa, cpR24fa, 0]';
bcm = [hconv, T_amb, 0;      % Boundary 1
    hplate, T_amb, 0;        % Boundary 2
    hch, T_amb, 0;
    hch, T_amb, 0;
    hch, T_amb, 0;               % Boundary 5
    hplate, T_amb, 0;
    hconv, T_amb, 0;
    hconv, T_amb, 0;
    hconv, T_amb, 0;
    hconv, T_amb, 0;         % Boundary 10
    hconv, T_amb, 0;
    1/hc, 0, 0;
    1/hc, 0, qch;
    1/hc, 0, 0;
    1/hc, 0, qch;
    1/hc, 0, 0;
    1/hc, 0, qch;
    1/hc, 0, 0;
    hconv, T_amb, 0;         % Boundary 15
    hconv, T_amb, 0;
    hconv, T_amb, 0;
    hconv, T_amb, 0;
    hconv, T_amb, 0;
    hset, Tedge, 0;          % Boundary 20
    hset, Tedge, 0;
    hset, Tedge, 0;          % Boundary 22
];
```

```
120
121 -  for e=1:NE
122 -      i=tm(1,e);  % index of node i
123 -      j=tm(2,e);  % index of node j
124 -      k=tm(3,e);  % index of node k
125 -      d=tm(4,e);  % subdomain of element
126
127        %get coordinates of nodes
128 -      xi=pm(1,i); % x-coordinate of node i
129 -      yi=pm(2,i); % y-coordinate of node i
130 -      xj=pm(1,j); % x-coordinate of node j
131 -      yj=pm(2,j); % y-coordinate of node j
132 -      xk=pm(1,k); % x-coordinate of node k
133 -      yk=pm(2,k); % y-coordinate of node k
134
135        %geometric characteristics of element
136 -      xij=xj-xi;
137 -      yij=yj-yi;
138 -      xik=xk-xi;
139 -      yik=yk-yi;
140 -      xjk=xk-xj;
141 -      yjk=yk-yj;
142 -      bijk=xij*yjk-xjk*yij;
143 -      Ae=abs(bijk)/2;
144
145        %properties of element
146 -      kt=sdm(1,d);        %conductivity (W/m-K)
147 -      rho=sdm(2,d);       %density (kg/m^3)
148 -      c=sdm(3,d);         %specific heat capacity (J/kg-K)
149 -      gv=sdm(4,d);        %generation (W/m^3)
150
151        %capacitance matrix
152 -      C(i,i)=C(i,i)+rho*c*Ae/6;
153 -      C(i,j)=C(i,j)+rho*c*Ae/12;
154 -      C(i,k)=C(i,k)+rho*c*Ae/12;
155 -      C(j,i)=C(j,i)+rho*c*Ae/12;
156 -      C(j,j)=C(j,j)+rho*c*Ae/6;
157 -      C(j,k)=C(j,k)+rho*c*Ae/12;
158 -      C(k,i)=C(k,i)+rho*c*Ae/12;
159 -      C(k,j)=C(k,j)+rho*c*Ae/12;
```

```
160 -         C(k,k)=C(k,k)+rho*c*Ae/6;
161 -
162           %conductance matrix
163 -         K(i,i)=K(i,i)+Ae*kt*(xjk^2+yjk^2)/bijk^2;
164 -         K(i,j)=K(i,j)-Ae*kt*(xjk*xik+yjk*yik)/bijk^2;
165 -         K(i,k)=K(i,k)+Ae*kt*(xjk*xij+yjk*yij)/bijk^2;
166 -         K(j,i)=K(j,i)-Ae*kt*(xik*xjk+yik*yjk)/bijk^2;
167 -         K(j,j)=K(j,j)+Ae*kt*(xik^2+yik^2)/bijk^2;
168 -         K(j,k)=K(j,k)-Ae*kt*(xik*xij+yik*yij)/bijk^2;
169 -         K(k,i)=K(k,i)+Ae*kt*(xij*xjk+yij*yjk)/bijk^2;
170 -         K(k,j)=K(k,j)-Ae*kt*(xij*xik+yij*yik)/bijk^2;
171 -         K(k,k)=K(k,k)+Ae*kt*(xij^2+yij^2)/bijk^2;
172 -
173           %generation matrix
174 -         g(i)=g(i)+gv*Ae/3;
175 -         g(j)=g(j)+gv*Ae/3;
176 -         g(k)=g(k)+gv*Ae/3;
177 -     end
178 -
179 -     q_s=zeros(N,1);
180 -     H=spalloc(N,N,3*NB);
181 -     Ht_infinity=zeros(N,1);
182 -
183 -     for b=1:NB
184 -         i=em(1,b);
185 -         j=em(2,b);
186 -         bnd=em(3,b);
187 -
188           %get coordinates of nodes
189 -         xi=pm(1,i); % x-coordinate of node i
190 -         yi=pm(2,i); % y-coordinate of node i
191 -         xj=pm(1,j); % x-coordinate of node j
192 -         yj=pm(2,j); % y-coordinate of node j
193 -
194           %get geometric characteristics of boundary segment
195 -         xij=xj-xi;
196 -         yij=yj-yi;
197 -         sij=sqrt(xij^2+yij^2);
198 -
199           % properties of boundary segment
```

```
200 -       h=bcm(1,bnd);               %heat transfer coefficient (W/m^2-K)
201 -       t_infinity=bcm(2,bnd);      %ambient temperature (K)
202 -       qf_s=bcm(3,bnd);            %specified heat flux (W/m^2)
203
204         %specified heat transfer vector
205 -       q_s(i)=q_s(i)+qf_s*sij/2;
206 -       q_s(j)=q_s(j)+qf_s*sij/2;
207
208         %convection matrix
209 -       H(i,i)=H(i,i)+h*sij/3;
210 -       H(i,j)=H(i,j)+h*sij/6;
211 -       H(j,i)=H(j,i)+h*sij/6;
212 -       H(j,j)=H(j,j)+h*sij/3;
213
214         %Ht_infinity vector
215 -       Ht_infinity(i)=Ht_infinity(i)+h*t_infinity*sij/2;
216 -       Ht_infinity(j)=Ht_infinity(j)+h*t_infinity*sij/2;
217 -   end
218
219 -   disp('Matrices Finished')
220 -   toc
221
222     %% Steady State Solution
223 -   tic
224 -   S=H+K;
225 -   r=q_s+Ht_infinity;
226 -   t_ss=S\r;
227
228 -   disp('SS Solution Finished')
229 -   toc
230
231     %% Figure Creation
232
233 -   black = [0 0 0];
234 -   set(0,'DefaultAxesColorOrder',[black]);
235
236 -   set(0,'DefaultLineMarkerSize',3);
237 -   set(0,'DefaultLineLineWidth',1.5);
238 -   set(0,'defaultAxesFontSize',16)
239 -   set(0,'DefaultLegendFontSize',16);
```

```
240
241 -   set(0,'DefaultAxesPosition',[0.11 0.13 0.82 0.86])
242 -   fig2 = figure(2);
243 -   hold on
244 -   pdeplot(pm,em,tm,'xydata',t_ss,'contour','on','colormap','jet')
245     % pdegplot('CHModelGeometry2')
246 -   xlabel('X-Distance [m]');
247 -   ylabel('Y-Distance [m]');
248 -   ylabel(colorbar,'Temperature [K]','FontSize',16)
249 -   axis([-0.006 0.325 -0.0114 0.2635])
250 -   axis equal
251 -   fig2.Units = 'centimeters';
252 -       fig2.Position = [-20 3 20 15];
253
254 -   set(0,'DefaultAxesPosition',[0.11 0.13 0.88 0.86])
255 -   fig3 = figure(3);
256 -   hold on
257     % pdeplot(pm,em,tm,'xydata',t_ss,'contour','on','colormap','jet')
258 -   pdegplot('CHModelGeometry2')
259 -   xlabel('X-Distance [m]');
260 -   ylabel('Y-Distance [m]');
261 -   axis equal
262 -   fig3.Units = 'centimeters';
263 -       fig3.Position = [-25 3 20 15];
264
265     %% Labels for Boundaries
266
267 -   figure(3)
268 -   hold on
269 -   line('XData',[0.225 0.25],'YData',[0.018 0.03])
270 -   line('XData',[0.11 0.143],'YData',[0.17 0.14])
271 -   line('XData',[0.21 0.16],'YData',[0.17 0.14])
272 -   line('XData',[0.07 0.1],'YData',[0.025 0.01])
273
274 -   x = 0.21908125;
275 -   y = 0.016;
276 -   Radius = 0.006;
277 -   Angle = 0:0.1:2.5*pi;
278 -   xp = Radius*cos(Angle);
279 -   yp = Radius*sin(Angle);
```

7.3 Wall Temperature

7.3.1 Intensity Ratio Model

```
%%  Intensity Ratio Model
%   November 2018
%   Brian Fehring

close all
clear all
clc
tic

%% Input Section

InputAngle = 6.19;
Polarization = 1;
Win_FTOReflection = 1;
FTO_PolyoReflection = 1;
Polyo_LiquidReflection = 1;
Liquid_VaporReflection = 0.00;
CutoffIratio = 0.651;
Kappa = 1.08e-04;
BeamDivergence = 0.021;

Save = 0;

%% Refractive Indices

% Air - Prism - Oil - Window - FTO coating - R245fa Liquid - Polyolester - R245fa Vapor
n = [1.000277 1.515 1.515 1.515 1.85 1.33 1.45 1.1];

%% Property Calculations

TemperatureInterpolate = 0:0.005:50;

% Polyolester RI vs Temperature
p1 = -1.574e-7;
p2 = -0.000325;
p3 = 1.463;

nPolyolester = p1*TemperatureInterpolate.^2 + p2*TemperatureInterpolate + p3;

% R245fa Vapor vs Temperature
```

```
    % R245fa Vapor vs Temperature
    p1 = 6.143e-08;
    p2 = -9.666e-06;
    p3 = 0.0005513;
    p4 = 0.993;

    nvapor = p1*TemperatureInterpolate.^3 + p2*TemperatureInterpolate.^2 + p3*TemperatureInterpolate + p4;

    % R245fa RI vs Temperature
    p1 =   -1.32e-08;
    p2 =   6.131e-07;
    p3 =  -0.0005549;
    p4 =       1.269;

    nfluid = p1*TemperatureInterpolate.^3 + p2*TemperatureInterpolate.^2 + p3*TemperatureInterpolate + p4;
    nfluid = nfluid + sqrt(-1)*Kappa;

    %% Curve Fit Creation

    white = [1 1 1];
    gray = [0.6 0.6 0.6];
    black = [0 0 0];
    purple = [0.4 0 0.5];
    magenta = [1 0 1];
    blue = [0 0 1];
    cyan = [0.15 0.6 0.9];
    green = [0 0.4 0];
    lgreen = [0.25 0.85 0];
    orange = [1 0.5 0.1];
    dred = [0.75 0 0];
    red = [1 0 0];
    lred = [1 0.25 0.25];
    yellow = [1 0.8 0.2];
    set(0,'DefaultAxesColorOrder',[gray;black]);
    set(0,'DefaultLineMarkerSize',1.25);
    set(0,'DefaultLineLineWidth',1.4);
    set(0,'defaultAxesFontSize',16)
    set(0,'DefaultAxesPosition',[0.11 0.12 0.85 0.83])
    set(0,'DefaultLegendFontSize',16);

    %FigureLabel = strcat('fig',PlotIndexStr);
    Fig = figure(1);
    hold on
    grid on
    Counter = 1;

    % Plot Model for Given Angles
for alpha = [InputAngle-BeamDivergence,InputAngle,InputAngle+BeamDivergence]
    for i = 1:length(nfluid)

        theta(1) = alpha;
        theta(2) = asind(n(1)*sind(theta(1))/n(2));
        theta(3) = 60 - theta(2);
        theta(4) = asind(n(2)*sind(theta(3))/n(3));
        theta(5) = asind(n(3)*sind(theta(4))/n(4));
        theta(6) = asind(n(4)*sind(theta(5))/n(5));
        theta(7) = asind(n(5)*sind(theta(6))/nPolyolester(i));
        theta(8) = asind(nPolyolester(i)*sind(theta(7))/nfluid(i));
        theta(9) = asind(nfluid(i)*sind(theta(8))/nvapor(i));

        Rp(1) = ((n(1)*cosd(theta(2))-n(2)*cosd(theta(1)))/(n(1)*cosd(theta(2))+n(2)*cosd(theta(1))))^2;
        Rp(2) = ((n(2)*cosd(theta(4))-n(3)*cosd(theta(3)))/(n(2)*cosd(theta(4))+n(3)*cosd(theta(3))))^2;
        Rp(3) = ((n(3)*cosd(theta(5))-n(4)*cosd(theta(4)))/(n(3)*cosd(theta(5))+n(4)*cosd(theta(4))))^2;
        Rp(4) = ((n(4)*cosd(theta(6))-n(5)*cosd(theta(5)))/(n(4)*cosd(theta(6))+n(5)*cosd(theta(5))))^2;
        Rp(5) = ((n(5)*cosd(theta(7))-nPolyolester(i)*cosd(theta(6)))/(n(5)*cosd(theta(7))+nPolyolester(i)*cosd(theta(6))))^2;
        Rp(6) = ((nPolyolester(i)*cosd(theta(8))-nfluid(i)*cosd(theta(7)))/(nPolyolester(i)*cosd(theta(8))+nfluid(i)*cosd(theta(7))))^2;
        Rp(7) = ((nfluid(i)*cosd(theta(9))-nvapor(i)*cosd(theta(8)))/(nfluid(i)*cosd(theta(9))+nvapor(i)*cosd(theta(8))))^2;

        Rs(1) = ((n(1)*cosd(theta(1))-n(2)*cosd(theta(2)))/(n(1)*cosd(theta(1))+n(2)*cosd(theta(2))))^2;
        Rs(2) = ((n(2)*cosd(theta(3))-n(3)*cosd(theta(4)))/(n(2)*cosd(theta(3))+n(3)*cosd(theta(4))))^2;
        Rs(3) = ((n(3)*cosd(theta(4))-n(4)*cosd(theta(5)))/(n(3)*cosd(theta(4))+n(4)*cosd(theta(5))))^2;
        Rs(4) = ((n(4)*cosd(theta(5))-n(5)*cosd(theta(6)))/(n(4)*cosd(theta(5))+n(5)*cosd(theta(6))))^2;
        Rs(5) = ((n(5)*cosd(theta(6))-nPolyolester(i)*cosd(theta(7)))/(n(5)*cosd(theta(6))+nPolyolester(i)*cosd(theta(7))))^2;
        Rs(6) = ((nPolyolester(i)*cosd(theta(7))-nfluid(i)*cosd(theta(8)))/(nPolyolester(i)*cosd(theta(7))+nfluid(i)*cosd(theta(8))))^2;
        Rs(7) = ((nfluid(i)*cosd(theta(8))-nvapor(i)*cosd(theta(9)))/(nfluid(i)*cosd(theta(8))+nvapor(i)*cosd(theta(9))))^2;

        R(1) = abs(Rp(1)*Polarization + Rs(1)*(1-Polarization));
        R(2) = abs(Rp(2)*Polarization + Rs(2)*(1-Polarization));
        R(3) = abs(Rp(3)*Polarization + Rs(3)*(1-Polarization));
        R(4) = abs(Rp(4)*Polarization + Rs(4)*(1-Polarization));
```

```
        R(5) = abs(Rp(5)*Polarization + Rs(5)*(1-Polarization));
        R(6) = abs(Rp(6)*Polarization + Rs(6)*(1-Polarization));
        R(7) = abs(Rp(7)*Polarization + Rs(7)*(1-Polarization));

        %            Transmitted  Air-Prism-Oil-Window    Ref Win-FTO                  Ref FTO-Polyo
        Iratio(i,1) = (((1-R(1))^2)*((1-R(2))^2)*((1-R(3))^2))*(R(4)*Win_FTOReflection + ((1-R(4))^2)*(R(5))*FTO_PolyoReflection + ...
        ((1-R(4))^2)*((1-R(5))^2)*R(6)*Polyo_LiquidReflection + ((1-R(4))^2)*((1-R(5))^2)*((1-R(6))^2)*R(7)*Liquid_VaporReflection);

    end

    CutoffIndex = find(isnan(Iratio),1,'first');
    if ~isempty(CutoffIndex)
        Iratio(CutoffIndex:length(nfluid)) = Iratio(CutoffIndex - 1);
        IratioAdjustCutoff = Iratio(CutoffIndex - 1)/CutoffIratio;
        Iratio = Iratio/(IratioAdjustCutoff);
    else
        IratioAdjustCutoff = Iratio(length(Iratio))/CutoffIratio;
        Iratio = Iratio/(IratioAdjustCutoff);
    end

    IratioDiv(:,Counter) = Iratio(:,1);
    Counter = Counter + 1;
end

for i = 1:length(IratioDiv)
    IratioFinal(i,1) = mean(IratioDiv(i,:),2);
end

hold on
plot(TemperatureInterpolate,IratioFinal);

Fig.Units = 'centimeters';
Fig.Position = [-26 6 20 15];


%% Figure Axis Lables and Legend

TemperatureAxisLabel = strcat('Test Section Saturation Temperature',' [',char(176),'C',']');
xlabel(TemperatureAxisLabel);
ylabel('Intensity Ratio [-]');
```

```

%     legend('Calibration Data','Reflectance Model','Location','northwest');

set(0,'DefaultLineMarkerSize',15);
[Legend,LegendObject] = legend('Calibration Data','Reflectance Model','Location','northwest');
LegendLines = findobj(LegendObject,'type','line');
set(LegendLines,'MarkerSize',15);

TemperatureCalibration(:,1) = TemperatureInterpolate;
TemperatureCalibration(:,2) = IratioFinal;
save('TemperatureCalibration2018620.mat','TemperatureCalibration');

%% Save Figure

if Save == 1
    FigSaveName = strcat('IratioModel.png');
    saveas(Fig,FigSaveName);
    FigSaveName2 = strcat('IratioModel.fig');
    saveas(Fig,FigSaveName2);
end

Timer = toc; disp(['Model Curve Calculation Complete: ' num2str(Timer) ' seconds'])

```